Optimizing the delivery of pre-transplantation therapies during normothermic machine perfusion of human kidneys

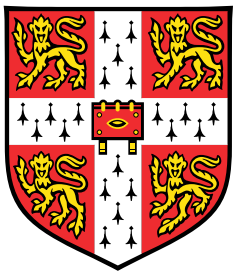

Jenna DiRito

Supervisor: Prof. M.L. Nicholson

Department of Surgery
University of Cambridge

This dissertation is submitted for the degree of
Doctor of Philosophy

Newnham College

April 2020

Declaration

I hereby declare that except where specific reference is made to the work of others, the contents of this dissertation are original and have not been submitted in whole or in part for consideration for any other degree or qualification in this, or any other university. This dissertation is my own work and contains nothing which is the outcome of work done in collaboration with others, except as specified in the text and Acknowledgements. This dissertation contains fewer than 60,000 words excluding figures, photographs, tables, appendices and bibliography.

Jenna DiRito
April 2020

Abstract

Optimizing the delivery of pre-transplantation therapies during normothermic machine perfusion of human kidneys

Jenna DiRito

Despite a severe organ shortage, thousands of kidneys from higher-risk donors go unused each year. These marginal kidneys have an increased susceptibility to ischemia reperfusion injury and the use of these organs may ultimately result in post-transplant complications like graft loss and recipient death. Normothermic machine perfusion has emerged as a platform for *ex vivo* assessment and repair to increase utilization of higher-risk donor organs without increasing risk to the recipient. This system also allows for the study the pathophysiology of human kidneys exclusively. After developing an understanding of how marginal kidneys behave during periods of controlled perfusion, one can then rationally design pre-transplant therapies to be delivered in isolation on the *ex vivo* circuit.

Through this body of work I have discovered (1) that it is possible to deliver vascular-targeted nanoparticle therapies during normothermic machine perfusion of human kidneys. I have shown that while nanoparticles may accumulate nonspecifically in red cell plugs, I have (2) identified the cause of and cleared the microvascular obstructions within a human kidney using a regimen of tPA and plasminogen. Having re-established microcirculation within a kidney not only improves drug delivery, but also allows for more homogenous oxygen and nutrient delivery, leading to a more viable organ. After having shown that nanoparticles can effectively delivered within this system following tPA and plasminogen treatment, I began to explore which therapeutics to deliver. I have (3) demonstrated that delivering an NLRP3 inhibitor during normothermic machine perfusion helps protect the organ from ischemia reperfusion injury. Finally, I have also (4) developed tools utilizing contrast-enhanced computed tomography to more holistically evaluate the vasculature of the entire kidney when assessing the efficacy of therapeutic approaches. This work almost exclusively utilized human kidneys that were deemed unsuitable for transplantation. Studying the exact specimen I am looking to repair has allowed me to develop highly translational therapeutic approaches that I believe can help improve marginal kidney utilization.

To my (not so) little brother, Nicky.
You are the reason I've smiled throughout this entire journey.

Acknowledgements

Above all else, I would like to thank the human donors and their families for providing the gift of human kidneys for research. Without them, this work would not be possible. I hope that my efforts with their precious gifts may one day translate to life saving treatments for transplant patients.

I would like to thank my supervisor Prof. M.L. Nicholson for his continuous time and guidance throughout my PhD. I could not have asked for a better mentor. Thank you for supporting all of my grandiose research ideas even if at times they were unrealistic. Your faith in me as a student and scientist has meant more than I could possibly express.

Thank you to Dr. Sarah Hosgood who quickly helped make Cambridge feel like a home. Thank you for always taking organ offer calls in the middle of the night, teaching me all of your perfusion tricks, and supporting my ambitious schedule of research.

I would like to thank my supervisor Dr. Gregory Tietjen. You have made me a better scientist and a better person. Without you, my PhD at Cambridge would not be possible. I will forever be grateful to you for helping me pursue dreams that I hadn't yet realized.

I would like to acknowledge Dr. Danielle Haakinson who has inspired me to continue on the long and fulfilling path to becoming a transplant surgeon and has assisted in accepting every one of the transplant declined kidneys used in the U.S.

I would like to extend my sincere gratitude to Drs. Mark Saltzman and Jordan Pober for mentoring me since I was an undergraduate at Yale. Their continued insight and guidance throughout my PhD has been invaluable.

I am grateful to my first year examiners, Prof. Menna Clatworthy and Mr. Vasilis Kosmoliaptsis for providing me with useful advice regarding the direction of my research.

Thank you to the generous funding for this PhD provided by the National Institute for Health Research Blood and Transplant Research Unit in Organ Donation and Transplantation at

Cambridge and Newcastle Universities and the Department of Surgery at Yale School of Medicine.

This work would not be possible without all of the technical and administrative support from Sylvia Rehokova, Jackie Higgins, Faye Hill, Lila Tran, Alison Warrington, Linda Butler, Adriana Clark, Korina Dacunto, and Ricarda Tomlin from the Cambridge and Yale Departments of Surgery.

I would like to thank the collaborators who contributed to this research:

- to Melanie Reschke who developed custom MATLAB code for quantification of microvascular obstructions;
- to Dr. Sathia Thiru who helped to assess microvascular obstructions
- to Alborz Feizi who helped to develop custom MATLAB code to quantify vascular area in dicom files generated from *ex vivo* CT imaging protocols
- to Drs. Claire Albert and Laura Bracaglia who helped to synthesize the targeted polymeric nanoparticles;
- to my summer student Anand Vaish for his help with immunofluorescent staining and developing custom MATLAB code to quantify immunofluorescence;
- to Dr. Kourosh Saeb-Parsy, Timothy Elliot Beech and Ms. Maggie Huang for their assistance and training in murine ischemia reperfusion injury models;
- to Addenbrooke's histopathology lab for their paraffin embedding and staining of human biopsies;
- to Core Biochemical Assay Laboratory for biochemistry measurements;
- to the staff of Central Biomedical Services for housing and maintaining the mice used for the renal ischemia reperfusion injury models;
- to Dr. Rafia Al-Lamki and Professor John Bradley for their assistance in setting up human organ culture models
- to Drs. Albert Sinusas, Stephanie Thorn, Nabil Boutagy, Attila Feher and the entirety of the staff at the Yale Translational Research Imaging Center for their assistance with *ex vivo* CT procedures on porcine and human kidneys;

- to Dr. Matthew Harris for his assistance in designing and executing *ex vivo* CT procedures on human kidneys;
- to Dr. Xinran Liu and the Bio and Cryo Electron Microscopy Core Facilities for their assistance with electron microscopy

I would like to thank my research family in Cambridge especially Dr. Krishnaa Mahbubani, Keziah Crick, Ashley Priddey, and Tegwen Elliott. Thank you for listening to me get too excited over research for the past three years. You have been the greatest support system I could ever ask for.

To my research family at Yale, Nensi Ruzgar, Melanie Reschke, Chris Edwards, Drs. Claire Albert, Laura Bracaglia, Taras Lysyy, Matt Harris, and John Langford thank you for always welcoming me back with open arms throughout the entirety of this very unusual dual-country PhD. You have been great colleagues and even better friends.

I am grateful to the Allocco Family for giving me a home away from home. You have helped make the transition into my PhD (and back) so full of love. Thank you for your continuous support.

Thank you to my parents for encouraging me to pursue my PhD even when I doubted my own abilities. Your hard work and perseverance through all of life's trials has motivated me more than words could possibly describe. Thank you for always being there.

To Nicky, my favorite brother, thank you for keeping me grounded. Thank you for the late night FaceTime conversations that kept me awake for my 24 hour experiments. Thank you for always making me laugh and inspiring me to be better.

Thank you to my best friend and the love of my life, August, for always standing by my side and telling me perfectly timed jokes. You have made me feel so secure and loved regardless of the miles that stood between us throughout this journey.

Related Works

Some passages have been quoted verbatim from the following sources. All figures from the following sources have been reprinted with permission from their respective journals.

J.R. DiRito, S.A. Hosgood, G.T. Tietjen, M.L. Nicholson. The future of marginal kidney repair in the context of normothermic machine perfusion. Am J Transplant. 2018; 18: 2400–2408. https://doi.org/10.1111/ajt.14963

G. T. Tietjen, S.A. Hosgood, **J.R. DiRito**, *et al*., Nanoparticle targeting to the endothelium during normothermic machine perfusion of human kidneys. Sci Transl Med. 2017 9: 418 https://doi.org/10.1126/scitranslmed.aam6764 (Reprinted with permission from AAAS.)

J.R. DiRito, Hosgood SA, Reschke M, *et al*., Lysis of cold-storage-induced microvascular obstructions for ex vivo revitalization of marginal human kidneys. Am J Transplant. 2020;00:1–13. https://doi.org/10.1111/ajt.16148

J.R. DiRito, *et al*., Inhibition of NLRP3 inflammasome during normothermic machine perfusion of human kidneys protects against ischemia reperfusion injury. *Manuscript in preparation, July 2020*

J.R. DiRito, *et al*., Contrast enhanced computed tomography for *ex vivo* assessment of human kidneys for transplant. *Manuscript in preparation, July 2020*

Abbreviations

Ab - antibody
AKI - acute kidney injury
ATN - acute tubular necrosis
ATP - adenosine triphosphate
a.u. - arbitrary units
BUN - blood urea nitrogen
CIT - cold ischemic time
CS - cold storage
CT - computed tomography
DAPI - 4',6-diamidino-2-phenylindole
DBD - donation after brain death
DCD - donation after cardiac death
DGF - delayed graft function
diH_2O - deionized water
DiI - 1'-dioctadecyl-3,3,3',3'-tetramethylindocarbocyanine perchlorate
DiO - 3,3'-dioctadecyloxacarbocyanine perchlorate
DLS - dynamic light scattering
DMSO - dimethyl sulfoxide
EC - endothelial cell
ECD - extended criteria donor
ECL - enhanced chemiluminescence
ELISA - enzyme linked immunosorbent assay
FACS - fluorescence-activated cell sorting
FDA - Food & Drug Administration
GFP - green fluorescent protein
GGT - gamma-glutamyltransferase
H&E - hematoxylin and eosin
HHS - Health & Human Services

HIPAA - Health Insurance Portability and Accountability Act
HRP - horseradish peroxidase
HUVEC - human umbilical vein endothelial cell
HTK - histidine-tryptophan-ketoglutarate
IACUC - institutional animal care and use committee
IC_{50} - half maximal inhibitory concentration
ICAM - intercellular adhesion molecule
IL - interleukin-6
IRI - ischemia-reperfusion injury
kDal - kiloDalton
KDPI - kidney donor profile index
LED - light-emitting diode
LR - lactated Ringers solution
pt - patient
MPS - mononuclear phagocyte system
MSB - Martius scarlet blue
MSC - mesenchymal stromal cell
NEDS - New England Donor Services
NF-κB - nuclear factor kappa B
NGAL - neutrophil gelatinase-associated lipocalin
NHS - National Health Services
NLRP3 - nucleotide-binding oligomerization domain-like receptor protein 3
NMP - normothermic machine perfusion
NPs - nanoparticles
PDI - polydispersity index
PECAM-1 - platelet EC adhesion molecule-1 (aka CD31)
PLA-PEG - poly(lactic acid)-poly(ethylene) glycol
RBC - red blood cell
RBF - renal blood flow
RCT - randomized control trial
RGB - red, green, blue
ROS - reactive oxygen species
SCS - standard cold storage
SD - standard deviation
SDS-PAGE - sodium dodecyl sulfate polyacrylamide-based discontinuous gel
SEM - standard error of the mean

Table of contents

List of figures

List of tables

Introduction

The state of renal transplantation

Transplantation is the best available treatment for end stage renal failure, but a worldwide shortage of donor kidneys has resulted in a significant gap between the number of transplants performed versus patients in need [1]. In the U.S., there are currently ~93,000 people waiting for a kidney, but only ~20,000 transplants are conducted annually [2]. This lack of access to transplantation leads to an average of 13 deaths on the kidney waitlist per day. In the same 24-hour period, ~10 donated kidneys are declined for transplant and ultimately discarded without clinical use typically due to concerns over post-transplant complications associated with organs from higher-risk donors [3, 4]. High-risk kidneys are believed to be more susceptible to ischemia reperfusion injury (IRI) as compared to standard criteria kidneys and are believed to have worse clinical outcomes, resulting in the limited utilization of these 'marginal' organs [5, 6]. The discard rates of kidneys from the donors believed to be highest risk—as determined by the Kidney Donor Profile Index or KDPI—can reach as high as 50-75% [7]. However, the continuing decline in the health of the organ donor population (e.g. increasing age, obesity) suggests that discarding all less than optimal organs is not a viable long-term strategy [4, 8–10]. There remains a need for new pre-transplant therapies to address the increased risk associated with transplanting marginal organs. Moving forward, comprehensive therapeutic strategies must be developed to protect high-risk kidneys from IRI in order to increase utilization of these organs.

Renal ischemia reperfusion injury

Clinically, IRI is defined as a sudden period of disrupted blood flow followed by the restoration of an oxygenated blood supply [11]. Histologically, IRI results in tubular necrosis, endothelial and epithelial damage, widespread inflammation, loss of structure, and cyst formation [12]. An ischemic organ will also typically have reduced metabolic function and microvascular damage. Post-transplant IRI can result in acute kidney injury manifested as

delayed graft function, which may ultimately impact long term graft survival [13, 3]. The severity of IRI can worsen depending on cytokine release at the time of death of the donor and through issues in general management of the organ resulting from the complex logistical nature of transplantation [6].

It is imperative to understand the components behind IRI to develop an appropriate treatment. IRI is a multifactorial process that is a result of the restoration of normoxic conditions following transplantation [6, 14]. This injury results in a dynamic process of neutrophil activation, increased production of cytokines, expression of adhesion molecules, and release of reactive oxygen species (ROS), resulting in inflammation and cellular necrosis [14, 15]. A critical mechanism in IRI that is explored in this thesis is the intracellular assembly and activation of the NLRP3 inflammasome, which triggers production of inflammatory caspases and the maturation of the prototypic inflammatory cytokine IL-1β and IL-18 [16–18]. Inhibition of the NLRP3 inflammasome has been proposed as a therapy to prevent IRI, but has yet been tested in relevant human models [18–20]. Although progress has been made in animal model systems, clinical translation remains a challenge.

To date, only a handful of clinical trials have started to investigate methods of ameliorating IRI (NCT00298168, NCT01442337, and NCT00802347). However, these clinical trials did not replicate the same successful outcomes previously demonstrated in rodent models. All the studies in question have faced similar challenges associated with systemic drug delivery and have been discontinued [21] . Traditionally, treatments for IRI (as well as for most other renal diseases) are delivered systemically following transplantation [22, 23]. The primary challenge of the systemic delivery stem is largely driven by the mononuclear phagocyte system (MPS). The MPS consists primarily of monocytes and macrophages present in the liver, spleen, and lymph nodes. This system works to remove foreign bodies, which can include therapeutics, from the circulation, and this often limits the effectiveness of systemically administered drugs [21]. Thus, there remains a significant need for highly specific renal therapies that can overcome the challenges of systemic delivery and adequately alleviate IRI.

Normothermic machine perfusion of human kidneys

Normothermic machine perfusion (NMP) has emerged as a modality for pre-transplant revitalization of marginal organs with the goal of improving utilization without increasing recipient risk [24, 25]. Leading centers in the UK, Canada, The Netherlands, and the United States have all begun to move NMP technology forward (Table 1)[26–28]. In the

current clinical practice of NMP, blood flow is re-established throughout the organ using serum-depleted red-blood-cells (RBCs) at or near body temperature for 1 hour prior to transplantation [26]. This approach has been established as a safe clinical procedure and has now been employed routinely in clinical practice in the U.K. [26]. Though the precise mechanism of potential benefit is still under investigation, this period of NMP facilitates functional assessment of the organ (e.g. hemodynamics, urine production) to allow surgeons to reconsider organs that had previously been deemed unsuitable for transplantation [24, 25]. This approach also allows aspects of the reperfusion phase of ischemia-reperfusion injury to happen in a controlled *ex vivo* setting rather than a sick patient, which may provide additional benefits. Preliminary results in a small series of kidneys from older deceased donors in the UK suggested that NMP may reduce DGF rates [24, 25]. A multicenter randomized control trial is currently underway (ISRCTN15821205) to directly assess if there are clinical benefits relative to standard cold preservation in kidneys donated after cardiac death (DCD) [26].

Delivering therapeutics on an *ex vivo* circuit

It is possible that NMP can improve some of the deleterious effects of IRI on its own, perhaps by a pre-conditioning mechanism in the setting of a protective, closely monitored environment [24]. In addition to these benefits, NMP serves as a platform to deliver potential treatments to further IRI treatments. NMP presents a unique opportunity to deliver therapies in isolation from the phagocytic system that rapidly eliminates systemically delivered drugs from circulation. Any treatments administered during NMP have direct contact with the organ vasculature and avoid most complications derived from systemic delivery [29]. NMP is being rapidly utilized as a device to deliver therapies within an opportunistic window in an attempt to reduce the injurious effects of ischemic injury [30, 31, 31, 32] . A handful of therapies, although not directly tested in human kidney NMP, have begun to emerge as promising treatments to protect renal grafts from complications of transplantation (Table 1).

Table 1 **State of experimental NMP studies.** A summary of experimental normothermic perfusion work was compiled following a comprehensive literature review using keyword searches in PubMed. Keywords used to identify relevant studies included normothermic machine perfusion, *ex vivo* normothermic perfusion, kidney perfusion, and renal perfusion. A methods review was then performed to identify all relevant studies. NMP with a focus on drug delivery is highlighted in bold. ATP, adenosine triphosphate; CS, cold storage; DBD, donation after brain death; DCD, Donation After Cardiac Death; GFP, green fluorescent protein; GGT, Gamma-Glutamyltransferase; HTK, Histidine-tryptophan-ketoglutarate; NGAL, Neutrophil gelatinase-associated lipocalin; UO, urine output; WIT, warm ischemia time.

Year	Author	Model	Methods	WIT (min)	Outcome
1980	Van der Wijk *et al.*; Groningen, Netherlands	canine heterotopic autotransplantation	DBD kidneys subjected to HMP for 72h, then NMP (*in situ*) for 1-4h and HMP for 72h more	N/A	kidneys can be preserved for up to 144h using intermediate NMP
1984	Rijkmans *et al.*; Groningen, Netherlands	canine heterotopic autotransplantation	DBD kidneys preserved for 6d HMP, interrupted at 3d for 3h of NMP	N/A	intermittent, brief NMP yielded superior results to HMP alone
1989	Maessen *et al.*; Groningen, Netherlands	canine heterotopic autotransplantation	DCD or DBD kidneys with 24 or 48h of CS w/ or w/o 30 min WIT with intermediate NMP	30	intermittent, brief NMP yielded superior results to CS alone
2000	Brasile*et al.*; Maastricht, Netherlands	canine heterotopic autotransplantation	DBD kidneys either reimplanted immediately, on HMP for 18h, or transitioned to 18h NMP before implantation	120	18h of NMP is feasible and results in immediate function following transplant
2002	Brasile *et al.*; Maastricht, Netherlands	canine kidneys	4h of NMP accompanied with GFP transfection	N/A	**transfections during NMP were successful and supported *de novo* synthesis of GFP**
2003	Brasile *et al.*; Maastricht, Netherlands	canine kidneys	DBD or DCD kidneys on HMP for 4-24h followed by 0 or 6h of NMP	30	HO-1 activity can be induced during NMP
2007	Kay *et al.*; Leicester, UK	porcine kidneys	kidneys flushed at with warm AQIXRS-I and given either CS or NMP	5-10	renal viability was maintained following 6h of NMP

Year	Author	Model	Methods	WIT (min)	Outcome
2008	Bagul *et al.*; Leicester, UK	porcine kidneys	2h CS, 18h CS, 18h HMP, or 16h CS + 2 h NMP followed by 3h reperfusion	10	NMP was able to restore depleted ATP levels and reverse some of the effects of CS
2008	Bagul *et al.*; Leicester, UK	porcine kidneys	18h CS followed by 3h NMP with carbon monoxide compared to control	10	**carbon monoxide, when delivered during NMP, may protect against IRI**
2009	Hosgood *et al.*; Leicester, UK	porcine kidneys	18h CS followed by 3h NMP with hydrogen sulfide compared to control	25	**hydrogen sulfide, when delivered during NMP, may protect against IRI**
2011	Hosgood *et al.*; Leicester, UK	human transplant	11h CS followed by 35m NMP immediately prior to transplant	30	NMP is a feasible method of preservation; first case conducted without compromising results of transplant kidney
2013	Nicholson *et al.*; Leicester, UK	human transplant	18 kidneys given 60 min of NMP compared to a control group of 47 recipients of ECD kidneys that underwent CS	patient dependent	significantly more predialysis patients and more receiving hemodialysis in NMP group compared to CS alone
2013	Hosgood *et al.*; Leicester, UK	porcine kidneys	DCD kidneys treated with CS for 24h or CS for 23h followed by 1h NMP	10	NMP kidneys had improved metabolic function and less tubular injury compared to CS kidneys
2014	Hosgood *et al.*; Leicester, UK	human transplant	10.5h of CS followed by 60 min NMP and then 5.3h CS	0	intermediate NMP is feasible and safe and may reduce effects of CI injury and extend length of preservation
2015	Kaths *et al.*; Toronto, Canada	porcine heterotopic autotransplantation	3h of CS followed by 10h NMP with leukocyte-depleted blood	0	prolonged NMP is feasible in DCD kidneys
2015	Hosgood *et al.*; Cambridge, UK	human discard kidneys	74 discard kidneys were given NMP for 60m and assigned a NMP score	patient dependent	a high percentage of viable kidneys are being discarded unnecessarily as assessed through NMP
2015	Hosgood *et al.*; Cambridge, UK	human discard kidneys	2 kidneys put on NMP for 60 min	patient dependent	NMP restores function and enables a platform for quality assessment of the kidney
2015	Hosgood *et al.*; Cambridge, UK	porcine kidneys	kidneys with variable WIT, CS for 2h followed by 3h NMP	15, 60, 90, or 120	NMP allows for assessment and potential recover from WI injury

Year	Author	Model	Methods	WIT (min)	Outcome
2016	Kaths *et al.*; Toronto, Canada	porcine heterotopic autotransplantation	DBD kidneys either stored for 8h in cold HTK or preserved with 8h of NMP	0	NMP is feasible and safe in good quality DBD kidney grafts
2016	Hosgood *et al.*; Cambridge, UK	human transplant	60 min of NMP following procurement from 35 y/o donor	13	NMP has the potential to rescue kidneys deemed "untransplantable", reducing their discard rate
2017	Kaths *et al.*; Toronto, Canada	porcine heterotopic autotransplantation	8h of CS followed by 0, 1, 8 or 16h of NMP with leukocyte-depleted blood	30	prolonged NMP is optimal for reconditioning; no CS produces better functioning kidneys
2017	Kaths *et al.*; Toronto, Canada	porcine heterotopic autotransplantation	kidneys with variable WIT underwent NMP for 8h	0, 30, or 60	perfusion characteristics (e.g. metabolism markers, functional parameters) correlate with injury
2017	Kaths *et al.*; Toronto, Canada	porcine heterotopic autotransplantation	DCD kidneys were either stored for 8h in cold HTK or preserved with 8 h of NMP	30	NMP improves renal graft function compared to CS
2017	Kaths *et al.*; Toronto, Canada	porcine heterotopic autotransplantation	DCD kidneys given 16h, 15h, 8h, or 0h of CS with 0h, 1h, 8h, or 16h of NMP followed by 60 min reperfusion	30	NMP provides superior outcome in DCD kidney transplant when compared to CS
2017	Blum *et al.*; Cleveland, Ohio	porcine kidneys	DCD kidneys with 5h of CS followed by 8h NMP	45	NMP provided comparable preservation of renal function as HMP and minimized AP and GGT release
2017	Adams *et al.*; Cambridge, UK	porcine kidneys	24h of CS or 23h of CS with by 1h of NMP using leukocyte-depleted blood prior to reperfusion	10	tubular and renal functions were better preserved after 1h NMP compared to warm perfusion or CS
2017	Hosgood *et al.*; Cambridge, UK	human discard kidneys	56 discard kidneys given 60 min NMP, scored based on the macroscopic appearance, RBF, and UO	13	urinary biomarkers (i.e. NGAL), functional perfusion parameters, and EVKP score provides informative measure of kidney quality for transplant decisions
2017	Tietjen *et al.*; New Haven, Connecticut	human discard kidneys	targeted nanoparticles administered and circulating for up to 8h of NMP	patient dependent	**endothelial cells can be successfully targeted with nanoparticles during NMP**

Year	Author	Model	Methods	WIT (min)	Outcome
2018	von Horn *et al.*; Duisburg-Essen, Germany	porcine kidneys	porcine kidneys stored on ice for 20h underwent NMP via standard protocols or with controlled oxygenated rewarming for 2 hours	20	controlled oxygenated rewarming of porcine kidneys improved renal function
2019	He *et al.*; Guangzhou, China	transplantable human kidney	human kidney was placed on NMP circuit immediately upon retrieval at donor hospital	0	ischemia free kidney transplantation is safe and possible
2019	Maassen *et al.*; Groningen, Netherlands	porcine kidneys	kidneys were perfused with hydrogen sulfide	30	hydrogen sulfide can induce a safe, **hypometabolic state in porcine kidneys**
2019	Adams *et al.*; Cambridge, UK	human discard kidneys	human kidneys with 18h preservation time treated with NMP at various oxygen concentrations or CS were reperfused with whole blood	10	Reducing oxygen concentrations during NMP does not have detrimental effects on renal function
2019	Urbanellis *et al.*; Toronto, Canada	porcine heterotopic autotransplantation	DCD porcine kidneys were reimplanted following 16h of CS, HMP, or NMP	30	NMP significantly improved early kidney function compared to other cold storage modalities
2019	Hameed *et al.*; NSW, Australia	human discard kidney pairs	discarded kidneys were either given 1h of NMP following CS or left on CS and then both were reperfused with whole blood	patient dependent	NMP demonstrated significant mechanistic benefits compared to CS alone
2019	Pool *et al.*; Groningen, Netherlands	porcine kidneys	kidneys underwent NMP for 7h, after 1h of perfusion MSCs were added to the perfusate	30	**MSCs were localized to the glomeruli**
2019	Brasile *et al.*; Nieuwegein, Netherlands	human discard kidney pairs	kidneys underwent 24h of NMP with or without MSCs	patient dependent	**MSC delivery aided in renal regeneration and reduced the inflammatory response**
2019	Aburawi *et al.*; Cambridge, Massachusetts	human discard kidneys	human kidneys were perfused for 6h with packed red blood cells or a synthetic hemoglobin based oxygen carrier	patient dependent	results between groups were comparable; using a synthetic hemoglobin based oxygen carrier is safe

Perfusate composition

Although major deviations from the original perfusate used by Hosgood et al have yet to be implemented, optimizing perfusate conditions may be a critical step in ensuring properly reconditioned organs. Vasodilators, anti-inflammatory and anti-hypertension drugs, insulin, glucose, and a nutrient solution are delivered during clinical cases of renal NMP to help establish strong renal blood flow and better prepare the kidney. Yet, there have been no studies examining the necessity or benefit of these additions to the perfusate. Other groups, have begun to investigate acellular perfusates such as Hemopure, a synthetic hemoglobin-based oxygen carrier, during NMP of human kidneys as a safe but more logistically feasible alternative to red blood cell based perfusates [33]. With the emerging literature on the benefits of NMP, it may be impactful for a study to be conducted that systematically examines and optimizes perfusate composition, to maximize all therapeutic results from NMP.

Gases

As a baseline, 95% oxygen is delivered during NMP and rates of oxygen consumption are used to measure the health of the organ [26, 34]. Oxygen consumption is maximized at normothermic temperatures, making NMP an ideal system for reconditioning. Nevertheless, there are other gases that, when delivered at low doses, have shown some evidence of having protective effects in the kidney. Carbon monoxide, nitric oxide, and hydrogen sulfide have all been investigated as therapeutic agents to protect against IRI, promote vasodilation, and inhibit apoptosis [30, 31, 35] . Both carbon monoxide and hydrogen sulfide have been shown to inhibit IRI throughout early functional outcome measures in porcine kidneys during NMP [35, 30]. Because gases can be easily absorbed into the blood, they work as ideal therapeutics in this closed, circulating system. Although little work has been done in clinically relevant systems for renal transplant, expanding and translating this work to a human model may offer kidneys additional benefit and protection prior to transplantation.

Stem cell therapies

Mesenchymal stromal cells (MSCs) can adapt to their microenvironment and differentiate into several different lineages, all while locally releasing a range of modulatory cytokines[36]. After encouraging results from animal studies, MSC administration has been adapted for pre-clinical studies, delivered via intravenous infusion after renal transplantation[36]. Although there were no adverse effects noted from these studies, MSCs were shown to be trapped in lung microcapillaries and could not reach the kidneys [36]. When delivered using isolated

perfusion circuits, MSCs have been showed to reduce inflammatory cytokine production and promote renal regeneration [37]. This approach has the potential to serve as a critical pre-transplantation therapy to repair ischemically damaged kidneys and is currently planned to undergo pre-clinical trials [37].

Gene therapies

The prospect of altering gene expression in isolated organs *ex vivo* opens the door for more effective, personalized therapies. In porcine models of *ex vivo* lung perfusion, adenoviral vector delivery has been demonstrated to be safe and effective [32]. This therapy resulted in a decreased inflammatory response with better graft functionality after transplantation [32]. In the area of renal research, Brasile *et al* previously demonstrated the ability to target an exogenous gene to the vascular endothelium of a kidney during NMP in a proof-of-concept experiment [38]. To protect the graft from complications of transplantation, gene therapies can be tailored for HLA silencing or to block transcriptional mechanisms of IRI. Introducing other methods of genetic manipulation, for example, siRNA, into the perfusate may require the utilization of stable vehicles for delivery.

Nanoparticles have properties that make them ideally suited to this role [39]. In contrast to other theorized treatments, nanoparticles have long-lasting effects and well-established slow-release profiles that extend beyond the period of normothermic perfusion [39]. Any drug that is typically delivered systemically can also be introduced during NMP for more concentrated, short-term treatments [29]. However, when treating IRI, a more prolonged, protective action is desired, as its effects persist long after the initial period of perfusion after transplantation. Each theorized therapy for this system has its own setbacks. What is needed is a modular system that can work across multiple mechanisms of IRI for an extended period [29].

Targeted nanoparticle therapies

Polymeric nanoparticles (NPs) have a long history of safe use in humans as drug delivery vehicles for the treatment of a wide variety of diseases [40, 41, 7] One of the primary benefits of NPs is their modularity. The polymer type can be varied to enable encapsulation of various classes of therapeutics from small molecules to nucleic acid–based drugs [7, 42]. In addition, NPs can be formulated to provide sustained therapeutic release with the rate of release controlled by polymer molecular weight. Finally, the polymer surface can also be modified in a variety of ways to suppress unwanted cellular interactions and/or enhance association

with a target cell type. Despite all the potential of NP drug carriers, clinical translation remains a challenge, largely due to issues with controlling NP localization following systemic administration.

Following systemic delivery, most varieties of NPs are rapidly eliminated via phagocytes in the liver and spleen (via the aforementioned MPS) [43]. This results in a relatively low accumulation of NPs at the desired site of therapeutic delivery and creates the potential for off-target toxicity [44]. To achieve higher accumulation at sites of disease, NPs have more recently been manufactured to have "stealth" properties in order to evade the immune system and thereby extend circulation times [45]. However, this method is not entirely effective and can still result in relatively short circulation half-lives and high levels of off-target accumulation.

Another popular strategy utilized in an attempt to introduce more reliable anatomic specificity is "molecular targeting." This approach employs conjugation of ligands to the NP surface, with the ligand selected on the basis of specificity for a receptor expressed on the target cell type of interest. Although this strategy seems logical, it is important to note that the forces that govern ligand- receptor interactions (e.g. hydrogen bonds, electrostatics) only operate over a distance of ~0.3-0.5 nm [46]. Thus targeting is not capable of equipping NPs with a capacity to "home" to sites of interest, but rather can only enhance the likelihood that an NP will be retained by a cell it happens to contact [47, 40, 41, 29] Consequently, molecular targeting has not been a reliable approach for controlling the anatomic localization of systemically administered NPs.

Although enhanced retention through the conjugation of ligands may not always be effective in systemic delivery, it is in many ways perfectly suited for an isolated NMP setting [41, 40, 29]. In the context of an isolated organ, NPs can largely avoid the challenges associated with systemic delivery [29]. An oxygenated plasma-free red cell solution is used to perfuse the organ, which obviates any complications that may arise from opsonization by serum proteins or tissue-resident phagocytes. Moreover, studies have shown that targeting will typically lead to internalization of NPs, which then provides an intracellular depot effect for effective drug delivery [48].

Whole organ assessment

To properly assess the efficacy of a therapeutic treatment, more comprehensive diagnostic tools must come to fruition. Although the number of marginal kidney transplants has

increased, there has been little progress in the development of a rigorous quality assessment for marginal kidneys. Currently, NMP also allows one to monitor the organ and assess its quality [27]. Outcome measures typically include renal blood flow, urine output, mean arterial pressure, oxygen consumption, creatinine clearance, ion concentrations, metabolic markers, and histologic analysis [49, 27]. A variety of biomarkers are assessed to determine the health of the organ, but a specific biomarker for IRI has yet to be identified. Most of these measures are providing clinicians with only superficial, regional information. It is likely that the quality of a perfusion is not uniform throughout the entire organ and that biopsies may only give insight into a certain section of the tissue. Additionally, biopsies are invasive measures that may impact the quality of organ perfusion. Measures like renal blood flow may not accurately describe the quality of microvascular perfusion. High urine output measurements may falsely signify a well-functioning kidney when the organ has lost its ability to properly concentrate urine. To more accurately gauge how well a kidney has reperfused, and how therapies are affecting the microenvironment, one must be able to look inside of the organ, non-invasively.

Throughout this thesis I have aimed to:

1. Effectively deliver targeted nanoparticles during *ex vivo* NMP 2. Re-establish microvascular circulation in poorly perfused organs 3. Understand mechanisms by which microvascular obstructions arise 4. Investigate potential pre-transplantation therapeutic strategies to prevent IRI 5. Develop non-invasive imaging methods to visualize perfusion quality of whole organs

I propose that this work, if adopted in clinical practice, will lead to the increased utilization of marginal kidneys for transplantation.

Chapter 1

Delivering targeted nanoparticles during normothermic machine perfusion

NMP creates a window of opportunity for the *ex vivo* delivery of therapeutic agents to further alter the graft microenvironment directly in the transplanted organ. In particular, the endothelial cell (EC) lining of the graft vasculature - the primary target of graft injury due to ischemia reperfusion or preformed anti-donor antibodies (Ab) [50–54] - is directly accessible to the perfusate during NMP. Reduction of preformed Ab by plasmapheresis or immunoadsorption, sometimes in combination with administration of intravenous immunoglobulin, may partially mitigate early Ab-mediated rejection [55]. However, these approaches are expensive, and neither strategy has been fully successful on its own. *Ex vivo* treatment of the vascular EC targets in the isolated graft (rather than the organ recipient) may represent a complementary strategy to enhance efficacy and minimize adverse systemic effects.

Because the nature of the host's adaptive immune response can evolve over the first few postoperative weeks, a prolonged therapeutic response over this time period will likely be needed. It has previously been shown that drugs encapsulated within polymeric nanoparticles (NPs) can be internalized by human ECs and that these NPs can serve as a slow release depot for drug delivery because the NPs slowly degrade by hydrolysis [56]. In the case of a small interfering RNA (siRNA), the therapeutic effect may persist 6 weeks or longer [7]. The challenge I address in this chapter is how to best ensure that NPs introduced during NMP are efficiently delivered to graft ECs.

Targeted NPs have thus far had only limited success in clinical medicine because of several challenges associated with systemic administration [39, 57]. First and foremost, NPs typically cannot efficiently escape from the vasculature to reach extravascular targets [58]. This results in marked accumulation within phagocytes of the liver and spleen that compete

nonspecifically with the intended target cell [59]. In addition, surface adsorption of serum proteins can create a so-called "protein corona" that can mask targeting ligands and abolish targeting benefits *in vivo* [60–62]. Targeting graft ECs during NMP, which uses a serum free perfusate, can potentially circumvent these challenges.

In this chapter, I show that conjugating anti-human CD31 Ab to poly(lactic acid)-poly(ethylene) glycol (PLA-PEG) NPs loaded with a fluorescent dye and administering them to isolated human kidneys during *ex vivo* NMP can lead to enhanced vascular retention compared to non-targeted NPs. Using two-color quantitative microscopy on cryosectioned biopsies, I observed the time-dependent accumulation of CD31-targeted and nontargeted NPs simultaneously in physiologically viable human kidneys during a period of NMP. This approach showed that Ab targeting to ECs can produce enrichment of accumulation in both renal glomerular and interstitial microvascular ECs in regions that were well perfused.

1.1 Identifying endothelial surface markers on human kidneys

To evaluate the potential use of molecularly targeted NPs for use during *ex vivo* perfusion of the human kidney, I first sought to identify a suitable surface protein on ECs to target. CD31, also known as platelet EC adhesion molecule–1 (PECAM-1), is a pan-EC marker typically expressed at relatively high quantities [63]. Although it is also expressed on platelets and new thymically released T cells, neither of these potentially competing cell types are present in isolated kidneys that are perfused with leucocyte-depleted and washed red blood cell (RBC) suspensions. CD31 has been shown to be a viable target to facilitate binding and subsequent internalization of Ab-conjugated NPs within ECs [64–66], provided that an appropriate epitope is recognized by the conjugated Ab [64]. These features suggest that CD31 may be well suited as a receptor for targeting of Ab-NPs uniformly to human renal ECs. However, the renal cortex contains a variety of vascular beds—including arteries, afferent and efferent arterioles, glomerular capillaries, peritubular capillaries, venules, and veins—that are molecularly distinct and may vary in the quantity of CD31 expressed (Figure 1.1A). To confirm the appropriateness of CD31 as the target, I probed for the expression of CD31 throughout the renal cortex of three separate human donor kidneys using fluorescence immunohistochemistry. CD31 staining was consistently present throughout the vascular beds of the renal cortex, suggesting that CD31 is an EC receptor with the potential to induce widespread accumulation of targeted NPs (Figure 1.1B and C).

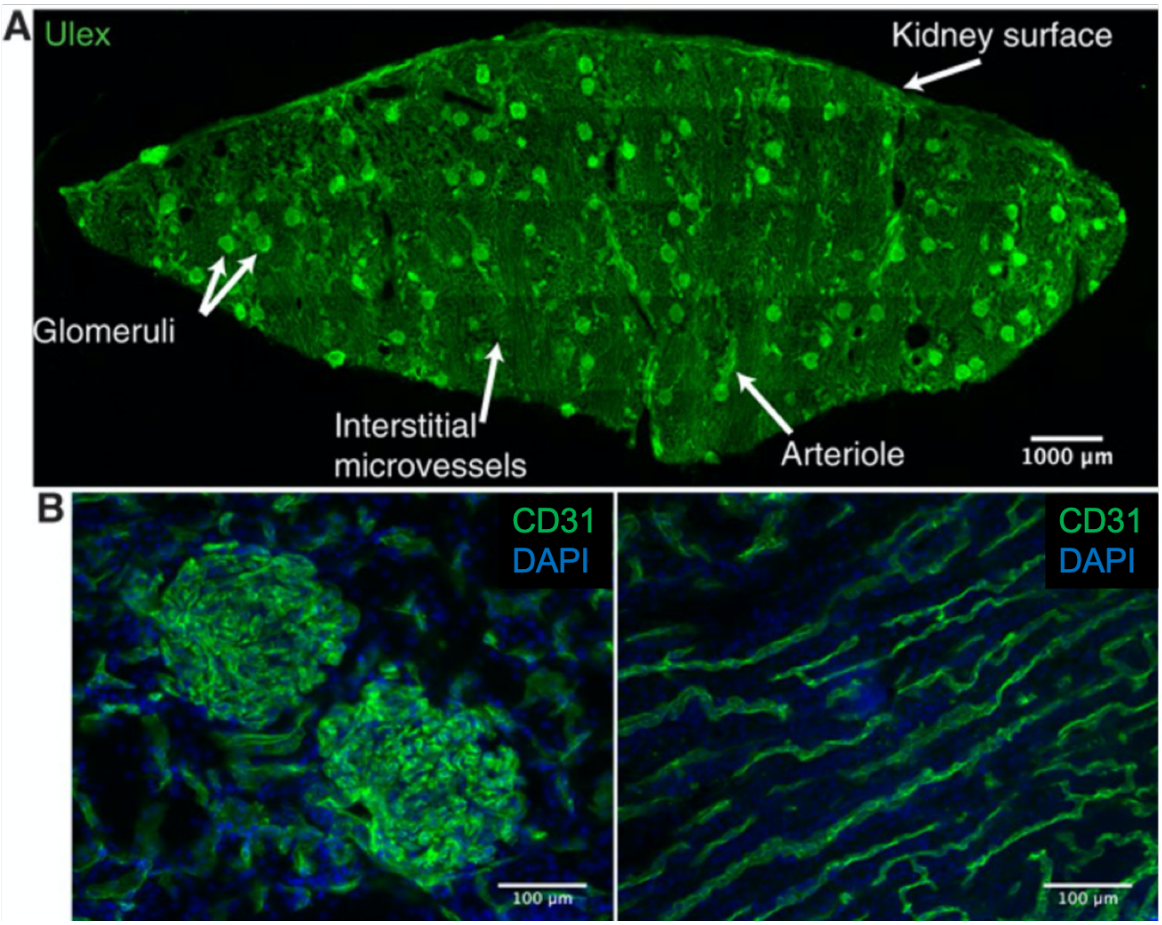

Fig. 1.1 **CD31 is present throughout the human renal vasculature.** (A) Representative fluorescent immunohistochemistry staining image of a cryosection taken from a wedge biopsy of a human kidney undergoing normothermic machine perfusion (NMP). Section was stained for Ulex to depict vascular endothelium (green). White arrows label different vascular beds and the kidney surface. Multiple 20× images were tiled to reconstruct the entire cryosection. (B) Representative images for CD31 (green) and nuclear 4',6-diamidino-2-phenylindole (DAPI; blue) staining of glomerular capillaries (left) and interstitial microvessels (right). Representative staining from three different donor kidneys

1.2 Targeted nanoparticle kinetics *in vitro*

I used nanoprecipitation to assemble NPs from a block copolymer of PLA-PEG (Figure 1.2A). This approach produces monodispersed NPs with an inert surface coating that reduces NP clumping [67] and thereby decreases the likelihood that aggregates of NPs might plug vessels and interfere with graft function. In addition, the PEGylated surface allows Ab to be conjugated using simple standard approaches [68]. NPs encapsulating either 1'-dioctadecyl-3,3,3',3'-tetramethylindocarbocyanine perchlorate (DiI) or 3,3'-dioctadecyloxacarbocyanine perchlorate (DiO) dye were about 165 to 170 nm in diameter with a polydispersity index (PDI) of $<$0.15 by dynamic light scattering (DLS; Figure 1.2B). Dyeloaded NPs were conjugated to either an anti-CD31 (CD31-NPs) or a nonbinding isotype-matched Ab (Control-NPs) via covalent coupling to terminal COOH end groups on the PEG. CD31-NPs strongly associated with HUVECs, whereas Control-NPs showed minimal association (Figure 1.2C). Quantification of this association via flow cytometry demonstrated that CD31-NPs enhanced accumulation by about 80× relative to Control-NPs under these static incubation conditions (Figure 1.2D and E).

Although targeted NP association in static culture is frequently used as a measure of potential for targeting in vivo [56], its relevance is unclear because association of NPs with ECs in the vasculature will occur under flow. The kinetics of targeted NP association with ECs are likely influenced by both the presence of flow and NP concentration. These features are particularly relevant for clinical NMP, given the relatively short perfusion period (typically about 1 hour). Thus, I quantified the targeting kinetics of CD31-NPs under physiologically relevant flow conditions and as a function of NP concentration. Previous studies have evaluated the kinetics of NP association with surface immobilized target receptors via surface plasmon resonance [69]; however, to my knowledge, quantitative studies evaluating the kinetics of NP association with live cells have not been reported.

Using microfluidic flow chambers (shear of 2 dyne/cm^2) and live cell imaging, I measured the association of CD31-NPs to HUVEC monolayers over an NP concentration range of 10 to 100 μg/mL. CD31-NPs accumulated on the EC monolayer, whereas Control-NP at 100 μg/mL did not (Figure 1.2F). CD31-NP binding did not fully saturate the surface of the cultured HUVECs over a 2-hour observation period even at the highest NP concentration tested (100 μg/mL; Figure 1.2F and G). As predicted for first-order kinetics, the rate of CD31-NP association scaled linearly with NP concentration (Figure 1.2H). Collectively, these cell culture data demonstrate both that the CD31-NPs bind ECs with robust specificity and that targeting is occurring under nonsaturating kinetics. This finding of nonsaturating kinetics is consistent with previous examples of CD31 targeting to cultured ECs under flow,

which showed apparent linear increases in NP accumulation with increasing NP dose, but a direct comparison of my results with previous studies is difficult because the previous studies did not directly examine the time dependence of NP accumulation [65, 66, 70]. The critical point raised by the observation that targeting to ECs is a kinetic (time-dependent) process, rather than equilibrium process, is that achieving robust accumulation within human kidneys during a short period of *ex vivo* NMP will require the optimization of both NP concentration and duration of exposure.

1.3 Delivering targeted nanoparticle kinetics *ex vivo*

To determine whether CD31-NPs can provide enhanced accumulation during *ex vivo* NMP, eight experimentally viable human kidneys that had been declined for transplantation were perfused with NPs. I first examined accumulation of CD31-NPs versus Control-NPs in two separate kidneys using the same low NP dose (4 μg/mL). Note that this is the initial NPconcentration in the perfusate reservoir; the actual concentration in the perfusate will change as fluid moves in and out of the intravascular space during normal kidney function and as NPs are depleted from the circulating perfusate. The goal of these experiments was to establish the necessary methodology, including detection within tissue samples by quantitative fluorescence microscopy. On the basis of the cell culture–targeting studies (Figure 1.2), I predicted that several hours of perfusion would be necessary for substantial NP accumulation at this dose. Therefore, using quantitative imaging of cryosections, I evaluated the accumulation of either CD31-NPs or Control-NPs in glomerular vessels and surrounding interstitial microvessels after 4 hours of NMP (Figure 1.3A and B). Although there was considerable variability, CD31-NPs accumulated about 2.5-fold more than Control-NPs (93.2 $\pm$ 23.2 mm^{-2} (CD31-NPs) versus 36.8 $\pm$ 15.4 mm^{-2} (Control-NP) normalized mean intensity; $\pm$ represents 95% confidence interval of the mean; Figure 1.3B).Notably, I did not find evidence for extravascular accumulation of NPs in either CD31-NP or Control-NP perfused kidneys, nor did I find NPs present in the urine during NMP. Accumulation within the vasculature was heterogeneous. For both CD31-NP and Control-NP, there were vessels that showed NP accumulation, whereas adjacent vessels appeared completely free of NP. Moreover, there was a statistically significant elevation of accumulation in glomeruli compared to surrounding interstitial microvasculature ($p < 0.0001$; Figure 1.3B).Accumulation within glomeruli was notably heterogeneous with strong accumulation in discreet regions, whereas other vessel segments appeared devoid of any accumulation (Figure 1.3A).

The cell culture results (Figure 1.2) suggested that accumulation of NP in renal vascular ECs could increase over several hours. Quantification of CD31-NP association with glomerular

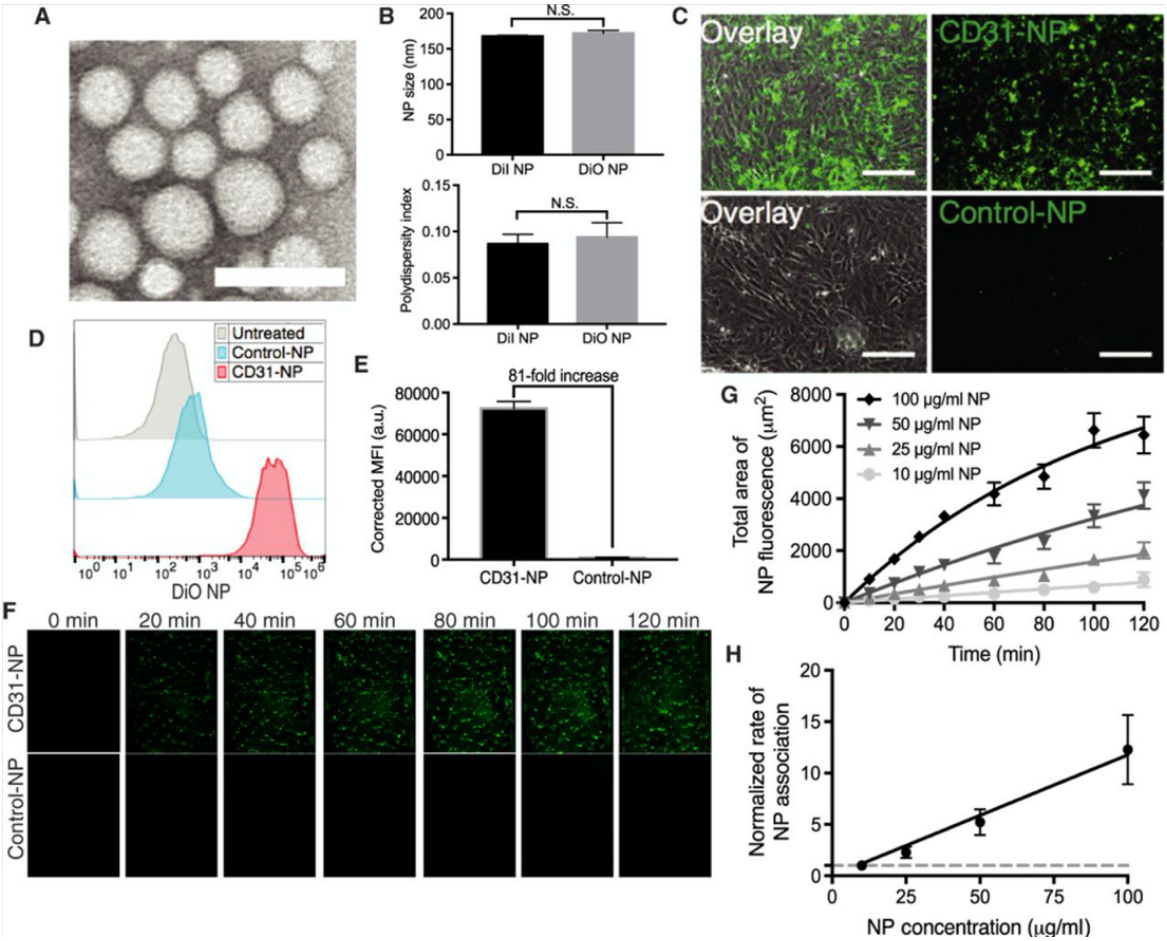

Fig. 1.2 **CD31 provides robust NP targeting *in vitro*.** (A) Representative transmission electron microscopy image of poly(lactic acid)–poly(ethylene) glycol NPs. Scale bar, 200 nm. (B) Quantification of NP size distribution and polydispersity index as measured by dynamic light scattering for both 1'-dioctadecyl-3,3,3',3'-tetramethylindocarbocyanine perchlorate (DiI)– and 3,3'-dioctadecyloxacarbocyanine perchlorate (DiO)–loaded nanoparticles (NPs; n = 3; a t test was used for statistical analysis). N.S., not statistically significant. (C) Representative 20× images of CD31-NPs versus Control-NPs after a 2-hour incubation with human umbilical vein endothelial cells (HUVECs) in static culture. DiO-loaded NPs are shown in green (right column) overlaid with brightfield images (left column). Scale bars, 150 μm. n = 3. (D) Representative fluorescence-activated cell sorting (FACS) histograms for HUVECs treated identically to (C). (E) Quantification of triplicate FACS experiments as shown in (D). n = 3. MFI, mean fluorescence intensity; a.u., arbitrary units. (F) Representative images of accumulation of DiI NPs as a function of time on HUVECs in a microfluidic cell culture during perfusion with CD31-NPs (100 μg/ml; top) or Control-NPs (100 μg/ml; bottom) at 2 dyne/cm^2. Each image is 300 μm wide, representing the full width of the microfluidic channel. NPs are pseudocolored green for better visualization. (G) Quantification of mean area of positive fluorescence for flow experiments as performed in (F) at a range of concentrations (n = 3 independent imaging regions for each dose and time point). Lines through data represent fit to a rate equation. (H) Plot of rates as a function of NP concentration as extracted from quantification in (G). Line through data represents linear fit. Rates are normalized to a concentration of 10 μg/ml (dashed line, 1). All error bars represent 1 SD.

ECs at early time points showed low NP signal that increased linearly with time (Figure 1.3C). In contrast, the NP signal observed in the kidney treated with Control-NPs appeared to show a rapid accumulation to a low, saturated value within the first 30 min. The rapidity of these nonspecific interactions, combined with their heterogeneous distribution throughout the vasculature, suggested that these NPs may be accumulating at specific sites due to discrete anatomical features of the tissue rather than binding to ECs. This raised the possibility that the difference observed between CD31-NPs and Control-NPs could have resulted from differences between the two kidneys rather than the nature of the NPs. Thus, although these results are consistent with an enhancement of accumulation of CD31-NP relative to Control-NP after 4 hours of perfusion, I next developed an approach to compare specific versus nonspecific accumulation simultaneously in the same kidney.

To determine the extent of specific versus nonspecific NP accumulation within an individual organ, I used a two-color NP approach where red-labeled (DiI dye) CD31-NPs and green-labeled (DiO dye) Control-NPs were simultaneously administered to each perfused organ; relative accumulation was then determined by quantifying the ratio of the two NP signals. The two-color NPs were matched for intensity under identical imaging and analysis conditions, as used for perfused kidney sections. The Control-NPs were specifically chosen for the green DiO channel to ensure that any tissue autofluorescence (which is predominately present in the green channel) did not artificially inflate the calculated degree of targeting specificity.

The analysis of Kidney 1 confirmed that CD31-NP targeting of renal ECs during NMP is time-dependent. Because the *in vitro* studies showed that increasing NP concentration increased the rate of delivery to ECs, I next focused on optimizing the concentration of NPs in the perfusate fluid above the initial concentration tested (4 μg/mL). A mixture of red CD31-NP (DiI) and green Control-NP (DiO) were administered to three donor kidneys, each at matched doses of 10, 50, and 100 μg/ml. Individual images of either glomeruli (masked to exclude any surrounding microvessels) or interstitial microvasculature (masked to exclude any glomerular vessels if present) taken within cryosections cut from wedge biopsies collected at various time points after perfusion were evaluated by quantitative microscopy. On the basis of the presence of apparent nonspecific accumulation in the single-color Control-NP kidney, I hypothesized that such areas would accumulate roughly equal amounts of red (CD31-NP) and green (Control-NP). A salient feature observed in all human kidneys treated with two color NPs were distinct regions of specific (red only) versus nonspecific (yellow, about equal amounts of red and green) accumulation (Figure 1.4A-C). Quantitative evaluation of yellow regions, either by line scan or total region evaluation, confirmed the nonspecific (about 1:1) nature of NP accumulation in these regions (Figure 1.4D and E). Within the same

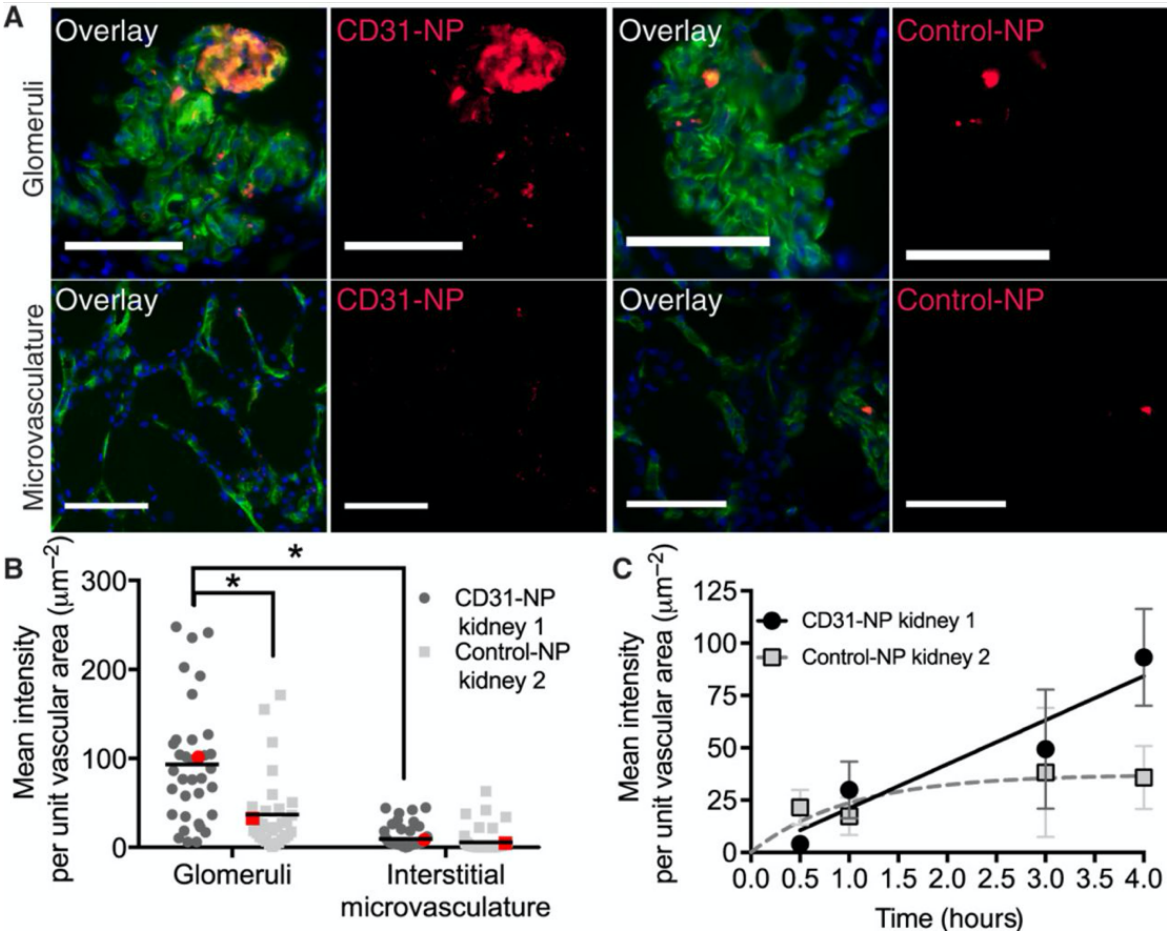

Fig. 1.3 **CD31 targeting enhances NP accumulation in perfused human kidney.** (A) Representative 20× fluorescent images of glomeruli (top) and interstitial microvessels (bottom) for kidneys perfused with either CD31-NPs (left) or Control-NPs (right). Overlay images show vascular stain (Ulex; green), DAPI nuclear stain (blue), and NP accumulation (red). Scale bars, 100 μm. Images are cropped to provide finer details. (B) Quantification of individual image MFI after background subtraction. Each image was normalized to the area of Ulex vascular stain, and every dot represents an individual normalized image mean intensity. The red dots correspond to the images shown in (A). *$p < 0.0001$ using a Mann-Whitney t test. For the single CD31-NP-treated kidney, n = 35 for images of glomeruli and n = 59 for images of microvasculature; for the single Control-NP–treated kidney, n = 31 for images of glomeruli and n = 56 for images of microvasculature. (C) Time-dependent normalized mean intensity values for CD31-NP versus Control-NP in glomeruli with corresponding fits to a linear equation (CD31-NP, black line) or saturating kinetic equation (Control-NP, dashed gray line). Error bars refer to 95% confidence window of the mean.

field of view as these nonspecific regions, there were other regions with distinctly higher CD31-NP-specific accumulation (about five-to-seven fold enhancement of CD31-NP relative to Control-NP in the highlighted regions shown in Figure 1.4). The presence of regions of about 1:1 CD31-NP/Control-NP accumulation in the same field of view and within the same cryosection as other vessels with five-to-seven fold higher values of CD31-NP-specific accumulation further validated the quantitative microscopy-based approach and supports the conclusion that CD31-NPs are capable of enhancing retention in regions of the kidney vasculature that do not otherwise accumulate NPs. In contrast, other regions of the same kidney accumulate NPs by a different mechanism that is not improved by targeting. In both cases, NP accumulation was exclusively intravascular.

The second round of experiments both validated the two-color NP targeting approach and identified optimal experimental conditions for quantitative microscopy. However, the variations in NP concentrations administered to the kidneys analyzed in the previous three organs limited the ability to directly assess how the benefits of CD31 targeting may vary from kidney to kidney. In particular, I was not able to assess how the quality of a given organ might affect specific versus nonspecific NP accumulation. Three additional donor kidneys (Kidneys 6 to 8) were perfused with 50 μg/ml each of CD31-NP (DiI-red) and Control-NP (DiO-green) under identical perfusion and sampling conditions. High-resolution (40×) image analysis was performed on cryosections taken from wedge biopsies collected before NP introduction and at 2, 4, and 6 hours after NP administration. The perfusion period was extended to a total of 8.5 hours for each kidney to provide a longer period for assessment of viability. The histological analysis of these kidneys did not identify major differences among the three organs, although the macroscopic appearances of Kidneys 6 and 7 were notably better than that of Kidney 8 (Table 1.1). Kidney 8 also demonstrated a decline in urine production after 4 hours, further suggesting that the quality of this kidney was not as high as Kidneys 6 and 7.

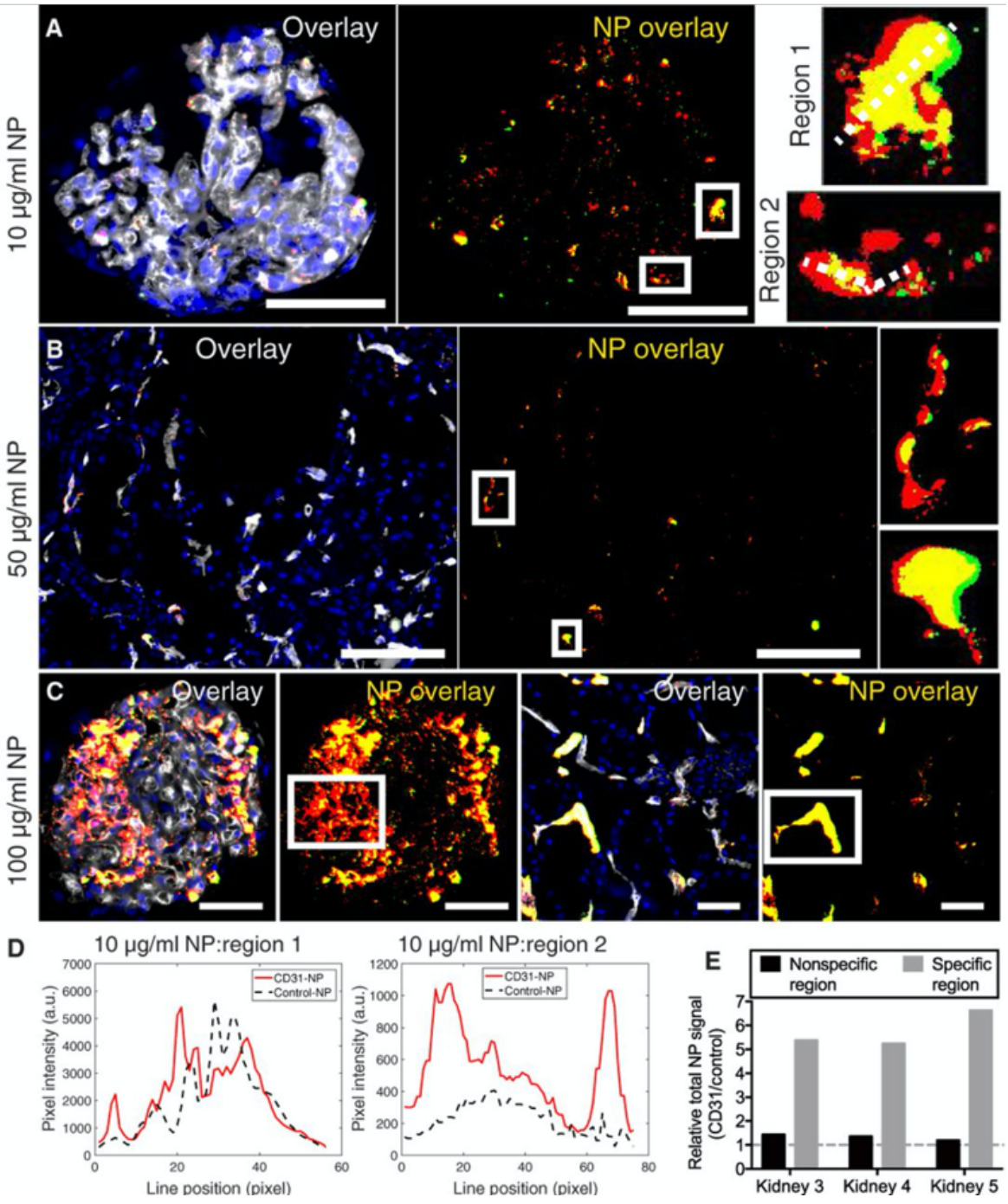

Fig. 1.4 **Specific versus nonspecific NP accumulation.** Representative thresholded 20× fluorescent images of (A) glomeruli from the NP kidney (10 μg/ml), (B) interstitial microvessels from the NP kidney (50 μg/ml), and (C) glomeruli and interstitial microvessels from the NP kidney (100 μg/ml) with white boxed regions highlighting areas of either specific or nonspecific accumulation within the same field of view or same section (DAPI, blue; CD31-NPs, red; Control-NPs, green; NP overlay, yellow; Ulex, white). The boxed regions are shown at a larger scale in the insets for both (A) and (B). The white dashed lines across the insets in (A) refer to the line scale analysis shown in (D) for nonspecific (region 1) and specific (region 2) accumulation. Scale bars, 50 μm. (D) Line scan plot of highlighted regions of NP glomerular accumulation in (A) showing similar amounts of accumulation in nonspecific regions with many more CD31-NPs relative to Control-NPs in more specific regions. (E) Region quantifications depicting the total relative NPs signal (CD31-NPs/Control-NPs) for the individual highlighted regions in (A) to (C); each bar represents the quantification of the single image shown for the respective panel.

Table 1.1 **Declined human kidney characteristics and experimental conditions** Declined human kidney characteristics and experimental conditions are presented for Chapter 1.

Kidney ID	Age	Donor type	Reason for decline	CIT (hh.mm)	NMP duration (hh.mm)	Mean RBF (mL/min/100g)	Total urine output (mL)	Macroscopic appearance	NP delivered	Final NP concentration
Kidney 1	57	DCD	Poor *in situ* perfusion	13.13	04.30	88.0 ± 19.6	177	Moderate	CD31-NP	4 μg/mL
Kidney 2	25	DBD	Malignancy	17.17	06.50	123.7 ± 35.2	730	Moderate	Control-NP	4 μg/mL
Kidney 3	44	DCD	Suspected malignancy	34.37	05.45	91.6 ± 23.9	107	Moderate	CD31-NP + Control-NP	10 μg/mL
Kidney 4	68	DBD	Suspected malignancy	16.03	05.00	67.9 ± 31.7	1045	Moderate	CD31-NP + Control-NP	50 μg/mL
Kidney 5	45	DBD	Poor *in situ* perfusion + prolonged agonal phase	22.38	05.00	83.5 ± 35.5	373	Moderate	CD31-NP + Control-NP	100 μg/mL
Kidney 6	64	DCD	Suspected malignancy	27.05	08.30	75.0 ± 22.1	598	Excellent	CD31-NP + Control-NP	50 μg/mL
Kidney 7	65	DCD	Histological changes consistent with diabetes	18.20	08.30	77.3 ± 25.4	451	Excellent	CD31-NP + Control-NP	50 μg/mL
Kidney 8	64	DCD	Damage to ureter and artery	25.58	08.30	80.7 ± 37.7	257	Moderate	CD31-NP + Control-NP	50 μg/mL

The two kidneys with the best macroscopic appearance (Kidneys 6 and 7) also had the highest average enhancement of CD31-NP accumulation relative to Control-NP in both glomeruli and interstitial microvessels at 2, 4, and 6 hours of NP perfusion (Figure 1.5A and B). Although there were individual glomeruli and regions of microvessels within these two kidneys, where the accumulation was largely nonspecific, there were multiple glomeruli and areas of interstitial microvessels where the CD31-NP accumulated at values about 5 to 10 times more that of the Control-NP (Figure 1.5A-C); one condition (Kidney 7 at 4 hours) had a few regions where targeting benefit exceeded 20 times. In contrast, Kidney 8 had generally reduced NP-targeting benefit that appeared to grow progressively worse over the course of 6 hours, concomitant with the decline in urine production (Figure 1.5A-C). These results further demonstrate that CD31-NPs are capable of accumulating via both specific and nonspecific means and that the degree of CD31-specific accumulation varies significantly among organs and in a manner that appears to correlate with the condition of the organ.

1.4 Nonspecific nanoparticle accumulation *ex vivo*

Confocal imaging revealed that nonspecific NP accumulation within the interstitial microvessels occurred primarily within the lumen of vessels, suggesting that this nonspecific accumulation was not occurring because of engulfment by extravascular, tissue-resident phagocytic cells (Figure 1.6A). Moreover, nonspecific NP accumulation localized to intravascular regions that contained RBC-shaped structures stained by Ulex Europaeus Agglutinin 1 (Ulex; which stains RBCs in addition to ECs; Figure 1.6B). This feature suggests that RBC-enriched vascular plugs may act as a sieve to accumulate high amounts of NPs in a nonspecific manner. Quantitative imaging of nonspecific regions that co-localized with high density RBC obstructions labeled by glycophorin A staining confirmed the nonspecific nature of this mode of accumulation (Figure 1.6, C and D).

To better understand the basis of nonspecific sites of NP accumulation, I evaluated formalin-fixed, paraffin-embedded sections of selective kidney biopsies. Hematoxylin and eosin staining of samples of Kidney 8, which had substantial nonspecific accumulation of NPs in interstitial microvessels (Figure 1.5A), revealed that there were extensive areas of vascular plugging by RBCs and RBC fragments that were present before NP introduction (Figure 1.6D). Widespread vessel plugging in the cortex and medulla persisted throughout the 4 hours of perfusion and was correlated with visual indicators of poor kidney perfusion (Figure 1.6D). These plugs did not appear to be classical thrombi because they showed minimal amounts of overt fibrin. The lack of fibrin is not unexpected, given that the perfusate consists of washed RBCs and lacks fibrinogen, but I cannot rule out the possibility that fibrin microthrombi

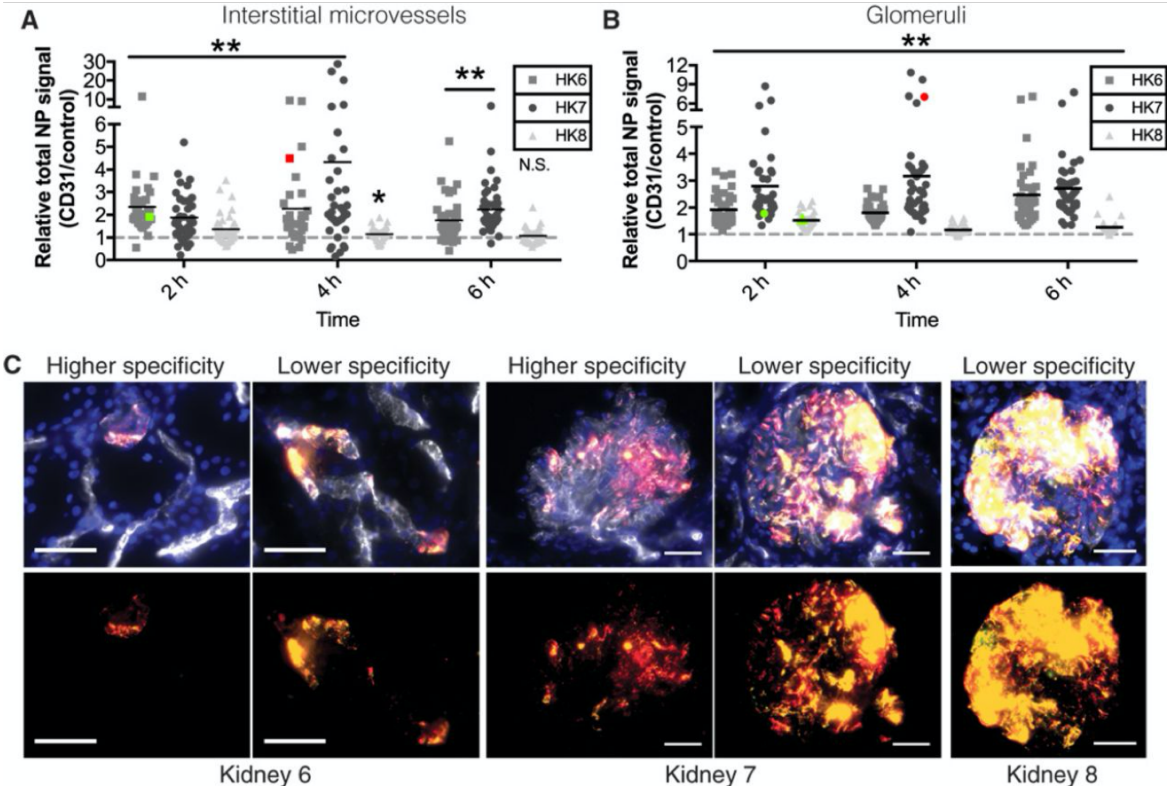

Fig. 1.5 **Effects of CD31-NP targeting in perfused human kidneys.** Quantification of relative NP signal (CD31-NPs/Control-NPs) at 4 hours (h) for kidneys 6 to 8. Each point represents an individual image of either interstitial microvessels (A) or glomeruli (B); non-specific (1:1) accumulation is represented by dashed gray line. **$p < 0.0001$ and *$p = 0.0024$ according to a Wilcoxon signed-rank test. Colored data points correspond to the quantification of the higher (red) or lower (green) specificity images shown in (C). (C) Representative images of either higher or lower specificity regions of NP accumulation in interstitial microvessels of kidney 6 (left) or glomeruli of kidney 7 (middle) and lower specificity regions in glomeruli of kidney 8 (right; DAPI, blue; CD31-NPs, red; Control-NPs, green; NP overlay, yellow; Ulex, white). Scale bars, 50 μm.

were present downstream and caused an RBC- and NP-rich plug to back up behind the obstruction. Alternatively, these plugs could represent vascular constrictions despite the presence of a vasodilator in the perfusion solution. Similar vascular plugs were observed to varying degrees in all kidneys in both glomeruli and interstitial microvessels; however, there was substantial variability in the degree of obstruction present between biopsies sampled at different time points and in different regional locations. This heterogeneity limits the ability to draw a quantitative correlation between vascular obstruction and nonspecific NP accumulation. Overall, gross evidence of poor perfusion provided a better correlation with nonspecific NP labeling.

Discussion

Although molecular targeting of drug carriers is often referred to as "active" targeting [71], molecular interaction forces (hydrogen bonds, electrostatic interactions) cannot provide a physical force that actively pulls the conjugate to a site of disease because these forces only operate over very small distances (< 0.5 nm) [46]. Thus, molecular targeting to a cell actually works by enhancing the likelihood that a targeted NP will be retained by a target cell with which it happens to come in contact. The maximal benefit from the addition of targeting ligands to NPs requires optimization of the route of administration to ensure that the NPs come in direct contact with the target cell of interest. For intravascular administration, ECs represent an ideal target cell type because NPs do not need to escape from the vasculature to reach them.

Many groups, including our own, have published on the advantages of therapeutic treatment during *ex vivo* perfusion [30, 31, 72, 73]. However, this study was the first of its kind to deliver cell-type specific targeted nanoparticles to human organs during NMP [74]. NMP provides an opportunity to isolate the targeted organ and thereby ensure that the delivered NPs only come in direct contact with the endothelium of interest. NMP also circumvents competition with phagocytic cells of the liver and spleen, which tend to substantially dilute any benefit associated with *in vivo* administration of molecularly targeted NPs. In addition, NMP is typically performed with a serum-free perfusate, which further alleviates issues associated with masking of targeting ligands by a protein corona [61, 62]. In this regard, NMP represents, in many ways, the ideal setting for realizing the maximal benefit of molecular targeting.

Despite this idealized nature of the NMP setting, a marked reduction between the degree of targeting benefit during *in vitro* cell culture (under either static or flow conditions) versus

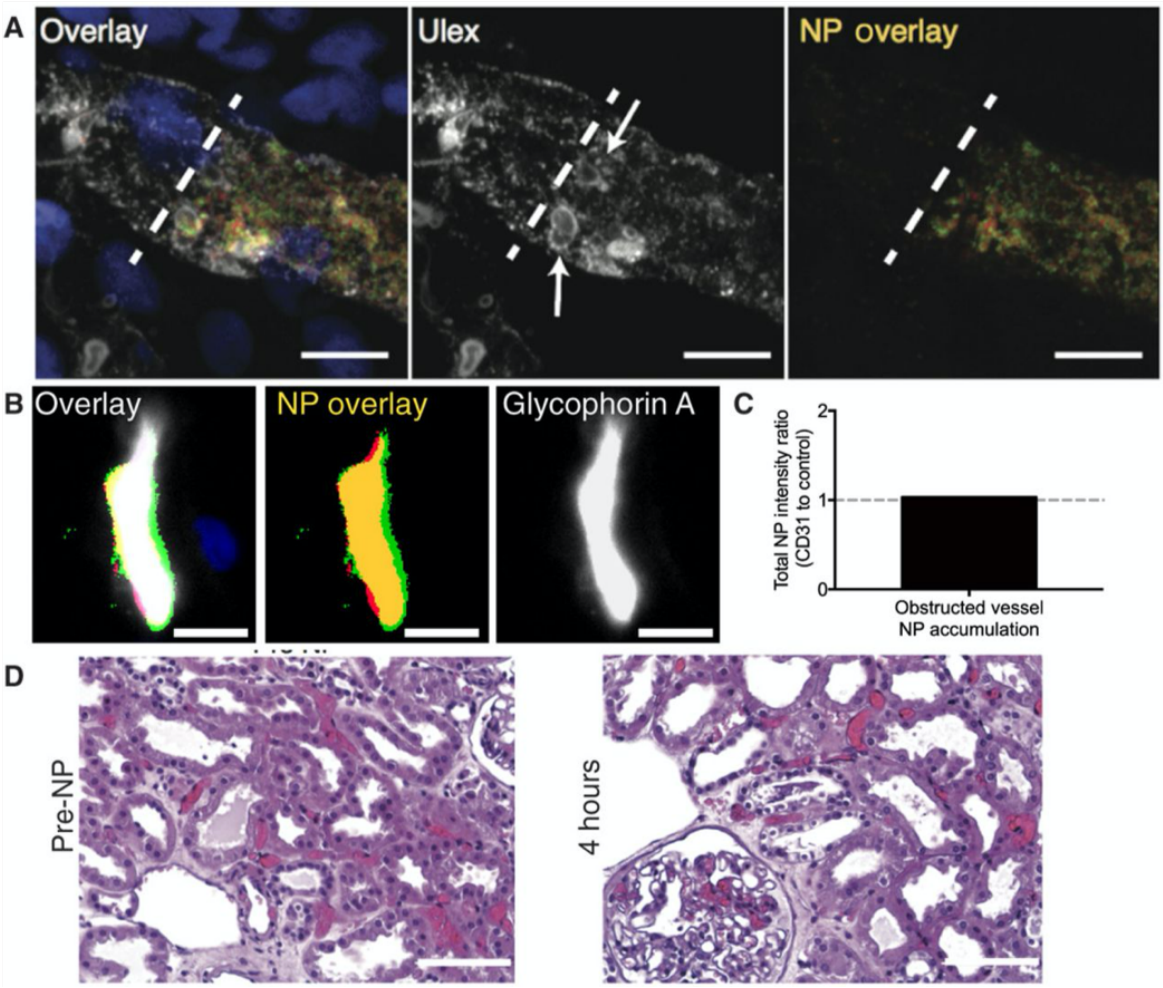

Fig. 1.6 **NPs accumulate at sites of vascular obstruction.** (A) Three-dimensional projection of a z-stack of confocal images of a vessel containing a high density of nonspecific NP accumulation in its lumen (DAPI, blue; CD31-NPs, red; Control-NPs, green; NP overlay, yellow; Ulex, white). Dashed white line represents the point of apparent obstruction, and arrows highlight apparent red blood cells (RBCs). Scale bar, 10 μm. (B) Representative image of nonspecific co-localization of NPs with sites of high-density RBC (glycophorin A, white; nonspecific NP, yellow) presumably representing vascular obstruction. Scale bar, 10 μm. (C) Quantification of relative NP signal (CD31-NP/Control-NP) for image in (B). (D) Representative hematoxylin and eosin–stained images of Kidney 8 (100 μg/ml) before NP introduction (pre-NP) or after 4 hours of NP perfusion. RBC occlusions are stained red. Scale bars, 100 μm.

an intact human organ was observed. Using static *in vitro* cell culture assays, CD31-NPs accumulated as much as 80-fold above that of Control-NPs. However, when delivered to human kidneys by NMP, targeted CD31-NPs accumulated only about two-to-four fold above the level of Control-NPs in the vasculature of the renal cortex when evaluated from a global average perspective. This two-to-four fold enhancement may seem relatively poor in comparison to previous results in *in vivo* animal models of CD31-NP targeting to vascular EC, where benefits have been observed as high as 10-to-20 fold [75, 41]. However, our detailed analysis suggests that this two-to-four fold enhancement results from taking an average across both nonspecific and CD31-specific modes of accumulation. These differences demonstrate the benefits of using a microscopy-based approach as an alternative or complement to whole-tissue quantification that necessarily loses information regarding the spatial heterogeneity of accumulation. Moreover, the presence of these discreet regions of about 1:1 NP signal in both glomeruli and interstitial microvessels served as an internal validation of the quantitative microscopy approach.

The relative abundance of the nonspecific accumulation appears to be coupled to the condition of the organ such that regional poor perfusion leads to more significant nonspecific accumulation. I postulate that in order to have effective targeted nanoparticle delivery, sufficient microvascular perfusion must be established throughout the entirety of the organ.

Chapter 2

Identifying and treating microvascular obstructions

In the previous chapter, I had shown that it is possible to deliver antibody-targeted polymeric nanoparticle drug carriers (NPs) to renal vasculature in the context of human kidney NMP [74]. I demonstrated that antibody-mediated targeting of CD31, a pan-endothelial surface protein, could enhance NP retention in well perfused organs. However, I also identified that NPs accumulate non-specifically at sites of microvascular plugging that arose to varying degrees in each of the 8 human organs evaluated [74]. This phenomenon exacerbated the heterogeneity of nanoparticle delivery throughout the organ and left many regions of the organ untreated. In addition, these obstructions impaired microvascular perfusion, likely leading to reduced oxygen and nutrient delivery in the plugged regions. The extent of microvascular plugging appeared to correlate with gross assessment of the quality of organ perfusion suggesting that removal of these plugs during NMP may improve organ viability.

In this chapter, I identify that these microvascular obstructions appear to arise as a result of local-renal production of fibrin(ogen) during cold-storage. As the staining reagents cannot distinguish between fibrinogen and soluble fibrin, I refer to this as fibrin(ogen). This fibrin(ogen) is rapidly released into the microvasculature upon restoration of normothermia/normoxia - both *ex vivo* or *in vivo* - leading to the formation of rouleaux-like RBC aggregates that plug in the renal microvasculature. Critically, the rate of fibrin(ogen) production during cold-storage varied substantially between donors with evidence suggesting that higher-risk donors (e.g. those >70 y/o) may be more susceptible to this pathology. I further demonstrated that *ex vivo* administration of plasminogen and tissue plasminogen activator (tPA) effectively clears these fibrin(ogen)-rich microvascular obstructions leading to more stable hemodynamics,

increased urine production, reduced markers of kidney injury, and significantly improved delivery of vascular-targeted nanoparticles.

These results highlight the utility of NMP as both an experimental tool to identify novel mechanisms of human organ injury and a clinical platform for therapeutic revitalization of marginal organs. Furthermore, they suggest that addressing fibrinogen-mediated, microvascular-plugging following reperfusion may enable better utilization of marginal organs from higher-risk donors and serve as critical first step to potentiate subsequent therapeutic delivery during NMP.

2.1 Microvascular obstructions arise during perfusion

In the previous chapter, I observed varying degrees of microvascular obstructions in each of 8 human kidneys subjected to NMP (Figure 2.1A) [74]. Upon histological examination, these obstructions appeared morphologically distinct from microthrombi. To better guide selection of therapeutic treatment for these obstructions, I first sought to identify their provenance. Transmission electron microscopy (TEM) on cortical biopsies from human kidneys subjected to NMP showed no evidence of either fibrin mesh or platelets as would be classically associated with either pre-existing donor microthrombi or newly formed microthrombi (Figure 2.1B). Instead, the obstructions appeared to be aggregates of red blood cells (RBCs) in a rouleaux-like formation (i.e. with the appearance of stacked coins) [74, 76, 77]. *In vitro*, RBC rouleaux formation is mediated by increased fibrinogen levels produced by the hepatic acute phase protein response to IL-6 [78]. Immunofluorescence microscopy confirmed high levels of fibrin(ogen) present within discrete regions of cortical microvasculature in human kidneys with confirmed microvascular obstructions (Figure 2.1C). Control isotype Ab staining verified the specificity of the immunofluorescence stain for fibrin(ogen) (Figure 2.2). I refer to this as 'fibrin(ogen)' in the context of immunofluorescence (or histochemical stain) of the microvascular obstructions because the reagents commercially available are not able to distinguish between fibrinogen protein and the thrombin-cleaved fibrinogen product known as fibrin.

To more clearly visualize the fibrin(ogen) and RBCs simultaneously, a Martius scarlet blue (MSB) trichrome stain was employed (Figure 2.1D). The MSB staining revealed dense aggregates of apparent fibrin(ogen) (red) and RBCs (yellow) in both peritubular capillaries and glomeruli. Collectively, these data suggest that fibrin(ogen) is integral to the observed RBC aggregates.

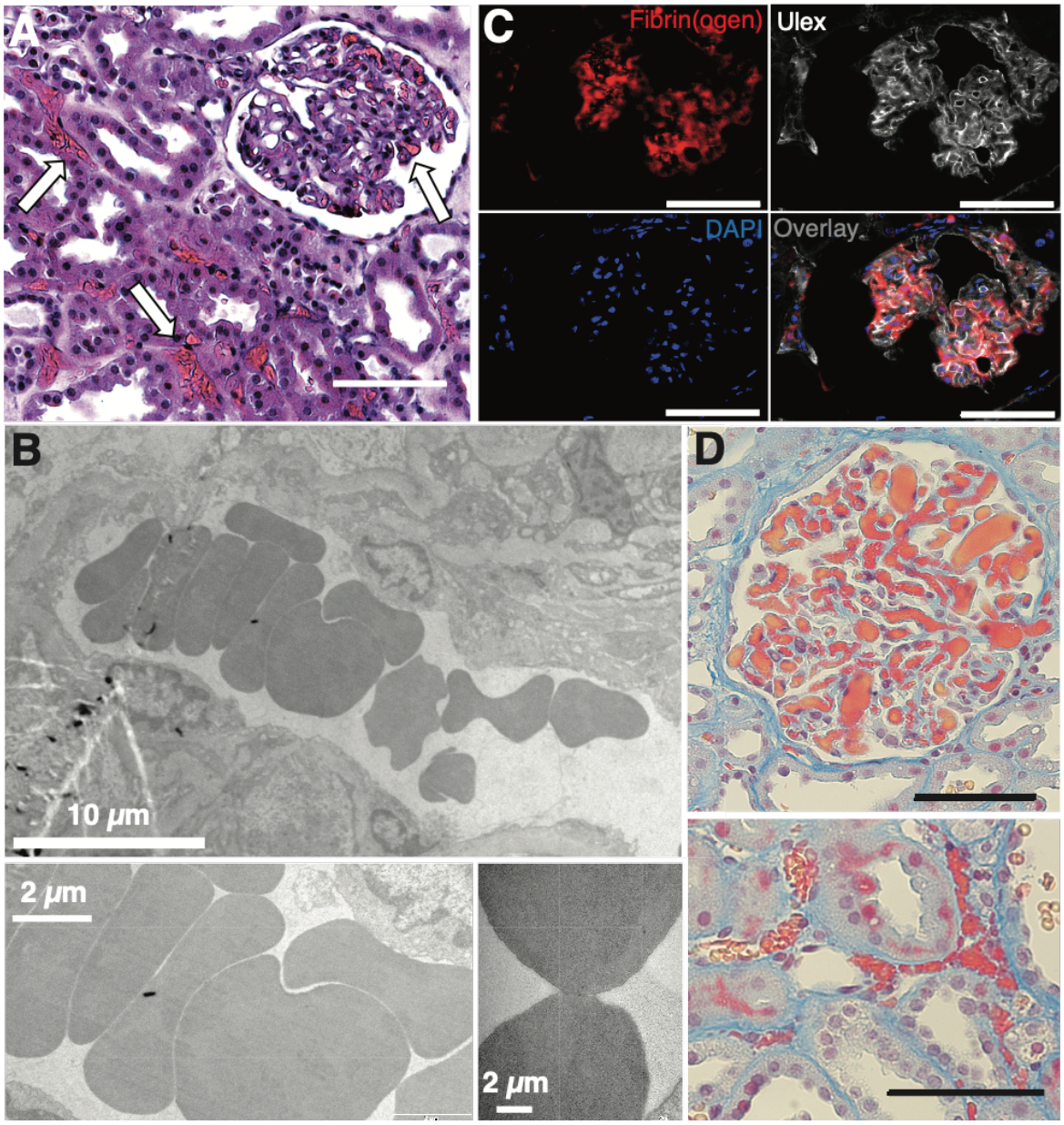

Fig. 2.1 **Fibrin(ogen)-rich microvascular plugs are present after NMP.** Representative images from perfused human kidneys 30 min after the start of NMP show microvascular obstructions in (A) H&E stained samples (white arrows) and (B) TEM images depicting microvascular obstructions with a rouleaux-aggregation of RBCs (scale bar is 10 μm). (C) Fluorescent staining depicts co-localization of fibrin(ogen) (red) with vasculature (white Ulex stain). Nuclei are stained blue. (D) Martius scarlet blue (MSB) stained samples (red - fibrin(ogen); yellow - RBC) in glomeruli (top) and microvessels (bottom). Scale bars represent 100 μm unless noted.

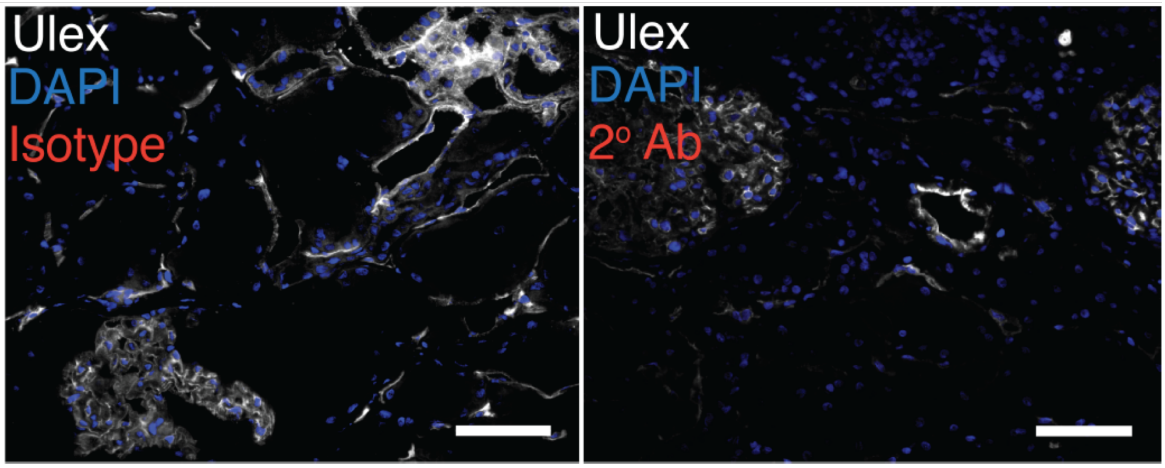

Fig. 2.2 **Staining controls for fibrinogen immunofluorescence staining.** Isotype and secondary controls for the immunofluorescent fibrin(ogen) staining demonstrate the staining specificity. Scale bars represent 100 μm.

Though it is classically associated with staining of fibrin, the MSB stain cannot definitively distinguish between fibrinogen, fibrin monomer or fully polymerized fibrin [79, 80]. However, extensive *in vitro* studies from literature suggest that fibrinogen alone is sufficient to form rouleaux RBC aggregates without the need for thrombin conversion of fibrinogen to fibrin [77, 76, 81]. Additionally, there was no evidence of thrombin activity in the perfusate following NMP (Figure 2.3). This lack of thrombin activity was expected given that the perfusate is derived from washed RBCs and therefore lacks clotting factors and platelets. Additionally, the perfusate is heavily heparinized to prevent any trace conversion of prothrombin to thrombin. Nevertheless, the possibility that some level of fibrinogen conversion to fibrin may be occurring in the formation of these microvascular obstructions can not be ruled out. Thus, for the remainder of this thesis, I will use 'fibrin(ogen)' to specifically refer to protein found in the intravascular compartment during NMP (either circulating in the perfusate or deposited within the obstructions) where the detection reagents cannot distinguish between fibrinogen, soluble fibrin monomer or insoluble fibrin polymer.

2.2 Fibrinogen is released from tubular epithelia into vasculature upon perfusion

The NMP procedure is performed in isolated kidneys with a heavily heparinized, washed RBC perfusate that lack serum proteins, including fibrinogen. *In vivo*, serum fibrinogen is primarily produced by hepatocytes. Thus, I anticipated that the obstructions must have

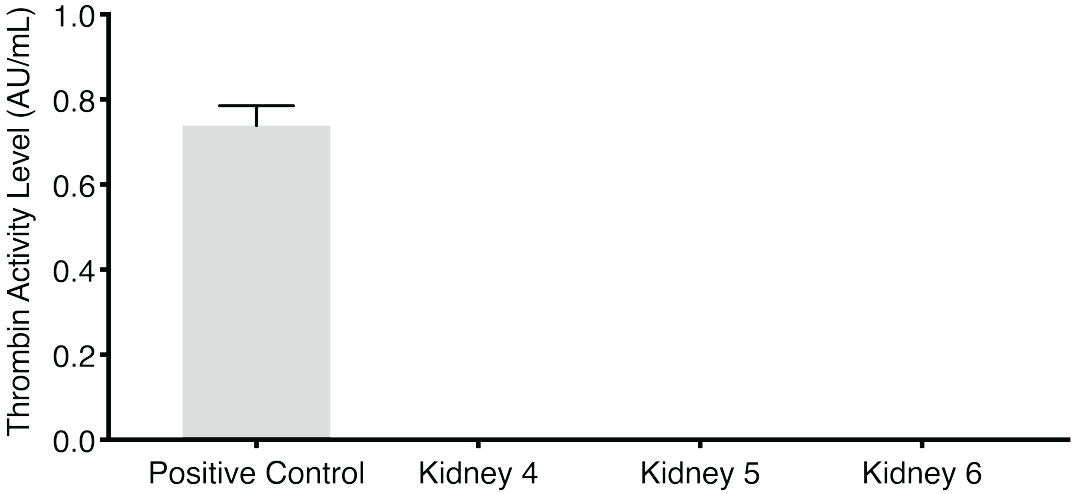

Fig. 2.3 **Absence of thrombin activity in kidney perfusates.** Thrombin activity levels were measured in perfusates collected after 90 min NMP in 3 separate kidneys. Each kidney was tested in technical triplicates. No thrombin activity was observed.

formed in the donor when hepatic fibrinogen was present and then been retained through the organ recovery and cold-storage process. To distinguish if the obstructions were present in the donor organ prior to NMP, I assessed repeat kidney biopsies taken from the same donor organ prior to NMP (i.e. at the end point of cold-storage) and then again after 30 min of NMP (Figure 2A). Surprisingly, I found that the fibrinogen stain was initially localized within tubular epithelia during cold-storage; here I presume that this intracellular protein is in its original uncleaved state. This epithelial stain was then lost after 30 min of NMP and coincided with the appearance of intravascular fibrin(ogen) concentrated at sites of microvascular obstruction (Figure 2.4A).

Consistent with this finding, there was no soluble fibrin(ogen) in the perfusate prior to NMP, but soluble fibrin(ogen) became detectable as early as 15 min following commencement of NMP (Figure 2.4A and B). Soluble fibrin(ogen) was also detected at high levels in the urine produced during NMP (Figure 2.4C). As urine is not recirculated in the NMP system and fibrinogen is not filtered by glomeruli, these results suggest that tubular epithelium may secrete fibrinogen in both the apical and basolateral directions. Alternatively, there is evidence that proteins present in urine can be scavenged and translocated back into the microvasculature [82]. The levels of soluble fibrin(ogen) appear much higher in urine than in the perfusate. However, levels detected in the perfusate do not include insoluble fibrin(ogen) bound within the obstructions, preventing a direct comparison of the amount of fibrin(ogen) secreted into the urine versus the microvasculature.

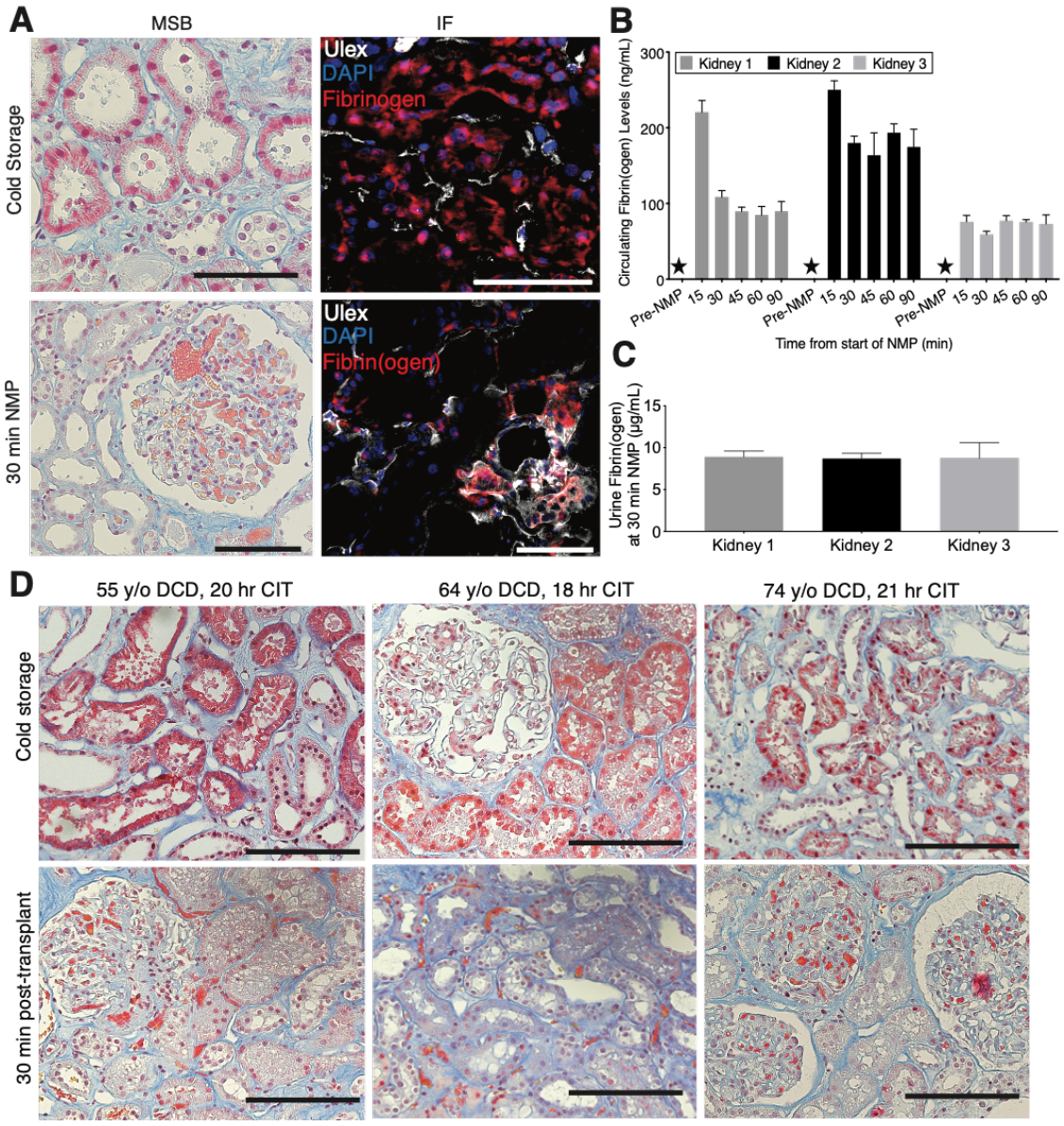

Fig. 2.4 **Normothermic reperfusion triggers intravascular accumulation of tubular cell-derived fibrinogen.** (A) Representative images during cold storage demonstrate positive stain in tubular epithelia in both MSB (left; pink stain) and immunofluorescence (right; fibrinogen/fibrin(ogen)–red; Ulex–white; DAPI–blue). A biopsy after 30 min of NMP depicts the migration of the positive stain to the vasculature. (B) Fibrin(ogen) levels in perfusate as measured by ELISA in technical triplicate for samples taken before and after NMP. Stars indicate samples below limit of detection. (C) Urine fibrin(ogen) levels in control kidneys measured in technical triplicate at 30 min of NMP. (D) Representative images from a clinical cohort of kidneys during cold storage that demonstrate positive MSB stain in tubular epithelia with MSB stain (top). A biopsy taken 30 min post-transplantation depicts the migration of the positive stain to the vasculature (bottom). Scale bars represent 100 μm.

To assess if this process of fibrinogen secretion would occur in a clinical setting, I evaluated a randomly-selected cohort of 15 human kidneys before and after clinical transplantation. These kidneys were part of the control arm of an ongoing, randomized controlled trial in the UK comparing the efficacy of NMP versus standard cold-storage (ISRCTN15821205) [26]. The only inclusion criteria for these organs was the presence of both a pre-transplant (at the end-point of cold-storage) and 30-min post-transplant biopsy. These 15 organs represent the first 15 organs that met this criterion from the clinical trial. Thus, the kidneys in this cohort varied in age and under-went variable periods of cold-storage time (Table 2.1). The paired biopsies from before and after transplant were again evaluated by MSB stain as an indicator of fibrinogen/fibrin(ogen) localization. Positive MSB stain was observed after cold storage (i.e. prior to transplant) specifically in the tubular epithelium of 6 of the 15 kidneys (Figure 2.5). Similar to the findings during NMP, this epithelial stain was lost 30 min post-transplant and coincided with the presence of positive intravascular stain co-localized with microvascular obstructions (Figure 2.4D).

Table 2.1 **Demographics of DCD kidneys transplanted from cold storage arm of NMP trial.** Demographics from transplanted DCD kidneys from the cold storage arm of the clinical trial assessing the benefits of normothermic machine perfusion.

Age	CIT (hh.mm)	High levels of tubular staining
55	19.44	Y
47	11	N
37	19.33	N
58	10.24	N
73	14.55	Y
67	13.36	N
59	11.53	N
74	21.24	Y
48	4.2	N
49	11.04	N
53	12.18	N
64	18	Y
28	19.36	Y
47	12	N
54	20	Y

Collectively, these data suggest that the fibrin(ogen) observed within the microvascular plugs during NMP is derived from the renal tubular epithelium. During cold-storage conditions, the newly synthesized fibrinogen is apparently sequestered within the tubular epithelium, perhaps

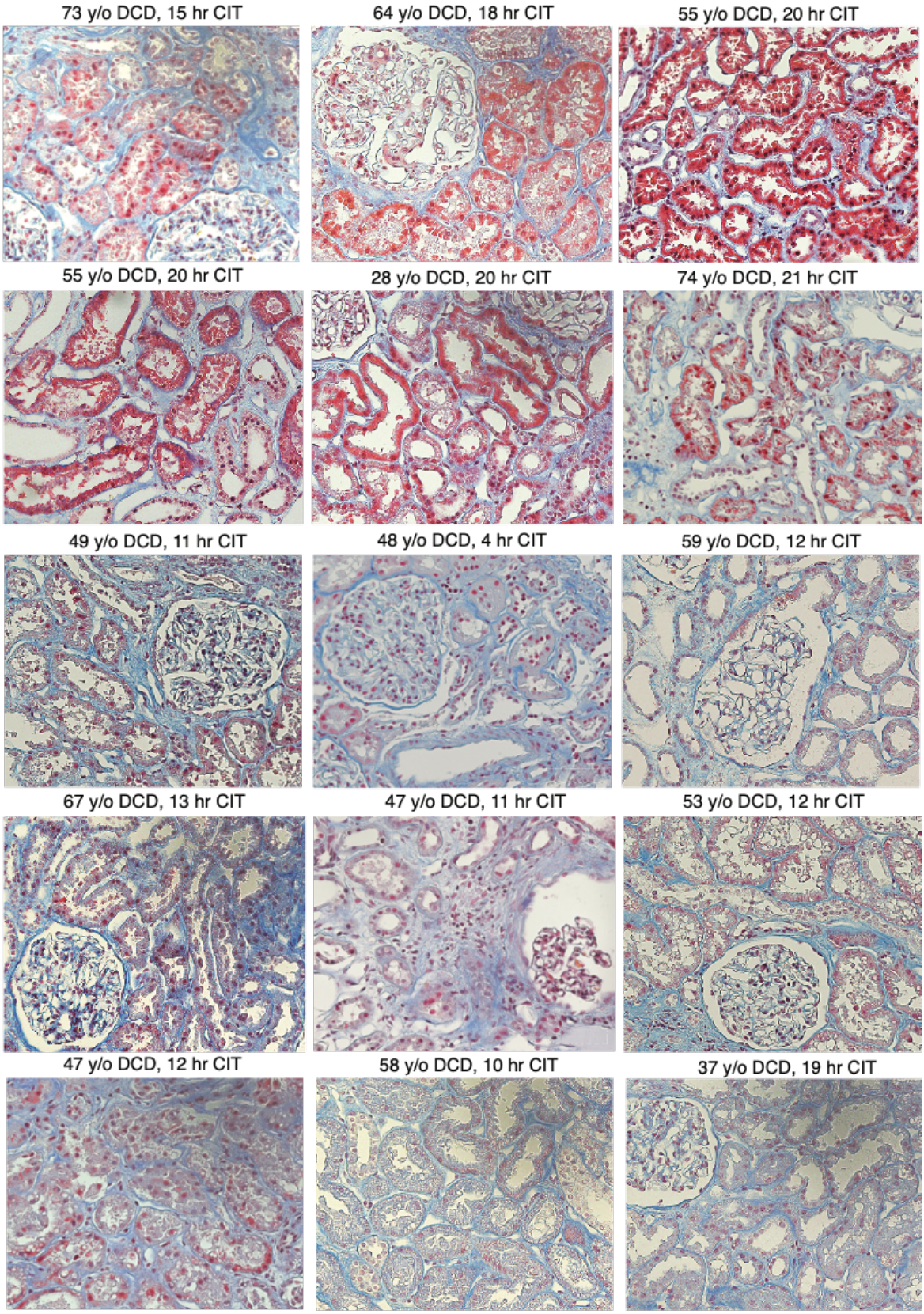

Fig. 2.5 **Tubular staining during cold storage of transplanted kidneys.** Images from a cohort of transplanted kidneys with various levels of tubular epithelial staining during cold storage.

due to the lack of active secretion at low temperatures [83]. Restoration of normothermia - either during NMP or after transplant - appears to initiate rapid secretion in a manner that can allow for transport into the microvasculature. Notably, extrahepatic synthesis of fibrinogen - including within mouse and human kidney - has been previously reported in response to ischemic injury and local inflammation [84–87].

2.3 Lysis of microvascular obstructions with tPA and plasminogen treatment

Having identified that NMP can initiate release of tubular fibrinogen into the vascular lumen, I next evaluated if an FDA-approved fibrinolytic therapy could clear the microvascular obstructions during NMP. Tissue plasminogen activator (tPA) is a commonly-used fibrinolytic that can degrade both fibrin thrombi and fibrinogen-rich RBC aggregates [88, 89]. tPA and similar thrombolytic agents have been previously evaluated in a pre-transplant setting with mixed results [90–92]. However, these studies typically applied tPA in the absence of its cofactor plasminogen; tPA catalyzes the conversion of plasminogen to the active enzyme plasmin [92, 90]. As the perfusate lacks serum proteins - and therefore contains no plasminogen - I hypothesized that exogenous plasminogen would be required for full effect.

To evaluate this hypothesis, a series of 6 human kidneys (i.e. each from different donors), declined for transplantation were evaluated in 2 treatment groups during NMP: combined tPA + plasminogen (Kidneys 1-3) or tPA only (Kidneys 4-6). The two groups were randomized for treatment versus control for 6 sequential donor organs received for research. Donor demographics (age, cold-storage time and reason for transplant-decline) are provided as a table in Table 2.2. Each organ underwent a standard clinical course of NMP with repeat biopsies collected at 3 time points: (1) at the end of cold-storage prior to NMP to confirm fibrinogen presence in tubular epithelia; (2) after 30 min of NMP to allow translocation in to the vasculature; and (3) after an additional 60 min of NMP either in the presence of tPA + plasminogen, tPA alone, or no treatment.

Five of the six organs displayed clearly positive MSB stain of the tubular epithelia in the cold-storage biopsy prior to NMP (Figure 2.6A; Figure 2.7). However, all 6 organs displayed measurable levels of microvascular obstructions following the initial 30 min of NMP (Figure 2.6A). A custom machine-learning algorithm was used to quantify the % area of microvascular obstruction identified by the MSB stain in a series of images from each biopsy (Figures 2.8, 2.9, and 2.10). While levels of microvascular obstructions were

Table 2.2 **Human discard kidney donor demographics.** Demographics from kidneys included in the study are presented below.

Kidney ID	Age (yrs)	CIT (hr)	Reason for decline	Donor type	Treatment
Kidney 1	65	28	high biopsy score	DCD	tPA-PLG
Kidney 2	75	24	infarcts	DBD	tPA-PLG
Kidney 3	65	22	anatomy	DBD	tPA-PLG
Kidney 4	51	36	damaged vein	DBD	tPA
Kidney 5	61	29	long CIT	DCD	tPA
Kidney 6	64	25	suspected malignancy	DBD	tPA
Kidney 7	49	12	poor function	DBD	CS
Kidney 8	39	12	high biopsy score	DCD	CS
Kidney 9	70	6	high KDPI	DBD	CS
Kidney 10	70	6	high KDPI	DBD	CS
Kidney 11	74	12	poor function	DCD	CS
Kidney 12	52	12	suspected malignancy	DBD	CS
Pair 1L	75	28	suspected malignancy	DCD	tPA-PLG
Pair 1R	75	28	suspected malignancy	DCD	PLG
Pair 2R	63	28	high biopsy score	DBD	tPA-PLG
Pair 2L	63	28	high biopsy score	DBD	PLG
Pair 3L	77	34	pt refusal	DCD	tPA-PLG
Pair 3R	77	34	pt refusal	DCD	PLG
Pair 4R	76	30	lesions found on lymph nodes	DBD	NMP
Pair 4L	76	30	lesions found on lymph nodes	DBD	tPA-PLG
Pair 5L	53	36	SSC found on lung	DBD	NMP
Pair 5R	53	36	SSC found on lung	DBD	tPA-PLG
Pair 6R	76	30	ATN	DBD	NMP
Pair 6L	76	30	ATN	DBD	tPA-PLG

variable prior to treatment, one hour of treatment with tPA + plasminogen completely cleared microvascular obstructions in all 3 kidneys regardless of the initial degree of microvascular obstructions present (* $p < 0.0001$; Figure 2.6A and B). Administration of tPA alone did not clear the microvascular obstructions (Figure 2.6A and B) and actually displayed increased levels of microvascular obstructions in 2 of the 3 organs evaluated.

An experienced renal pathologist blindly assessed a series of slides to validate the results of the digital analysis across a random sample of organs (Table 2.3). The pathologist I worked with defined any kidney with microvascular obstruction in glomeruli or peritubular capillaries >50% to be unsuitable for transplant. This analysis was consistent with the quantitative microscopy approach and confirmed the efficacy of the combined tPA + plasminogen treatment.

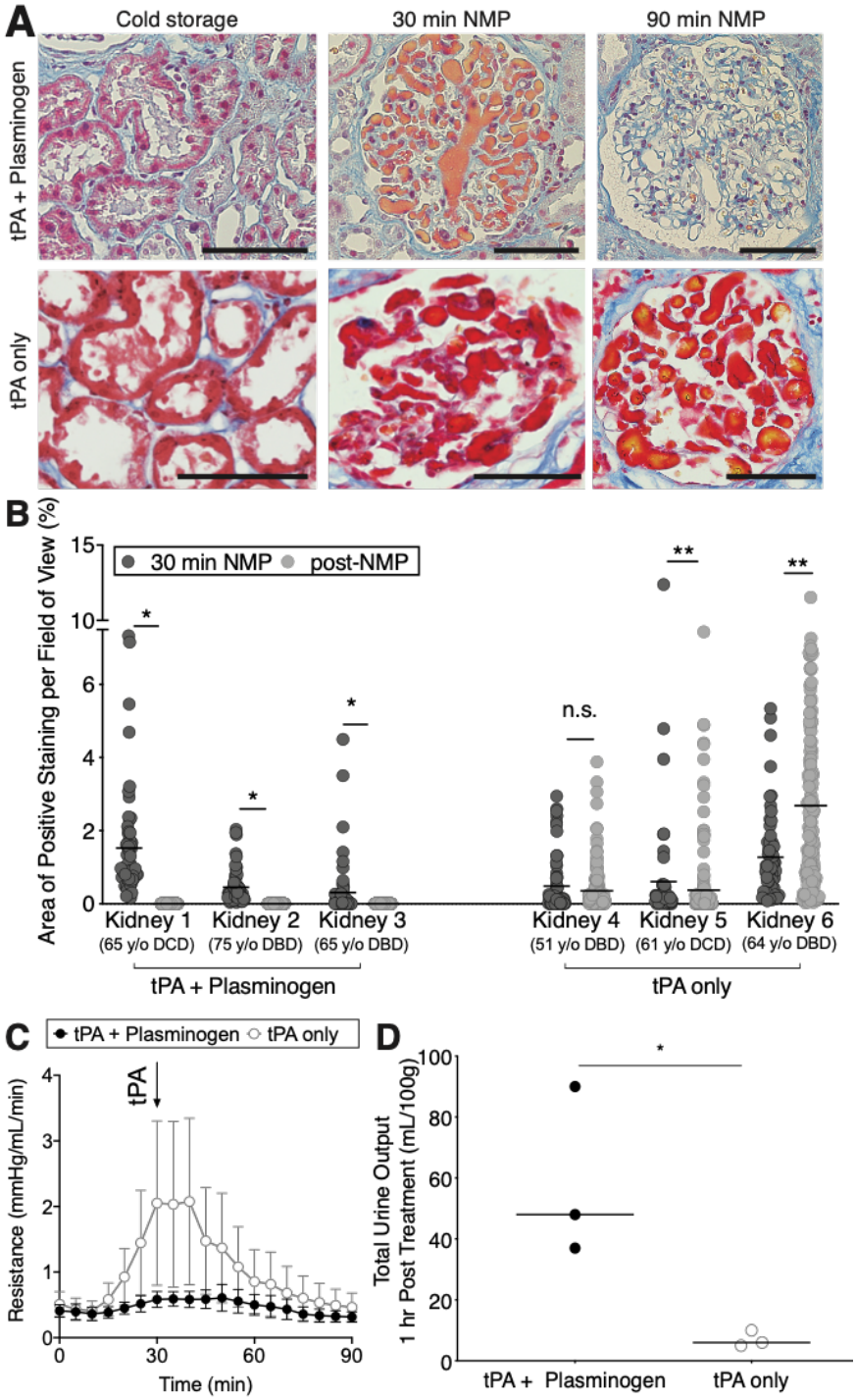

Fig. 2.6 **Combined tPA + plasminogen treatment lyses microvascular obstructions.** (A) Representative images and microvascular obstruction quantifications (B) are shown from single kidneys treated with tPA + Plasminogen or tPA only (* $p < 0.0001$, ** $p < 0.05$; Mann-Whitney t-test). Scale bars represent 100 μm. (C) Resistance time traces as measured during NMP for tPA + Plasminogen treated kidneys versus tPA only controls. Data points represent the mean of all 3 kidneys evaluated in each group. Error bars represent standard error of the mean. Arrow denotes point of tPA administration. (D) Total urine output was measured after 90 minutes of NMP (* $p = 0.0340$; unpaired t-tests). Data points represent individual kidneys.

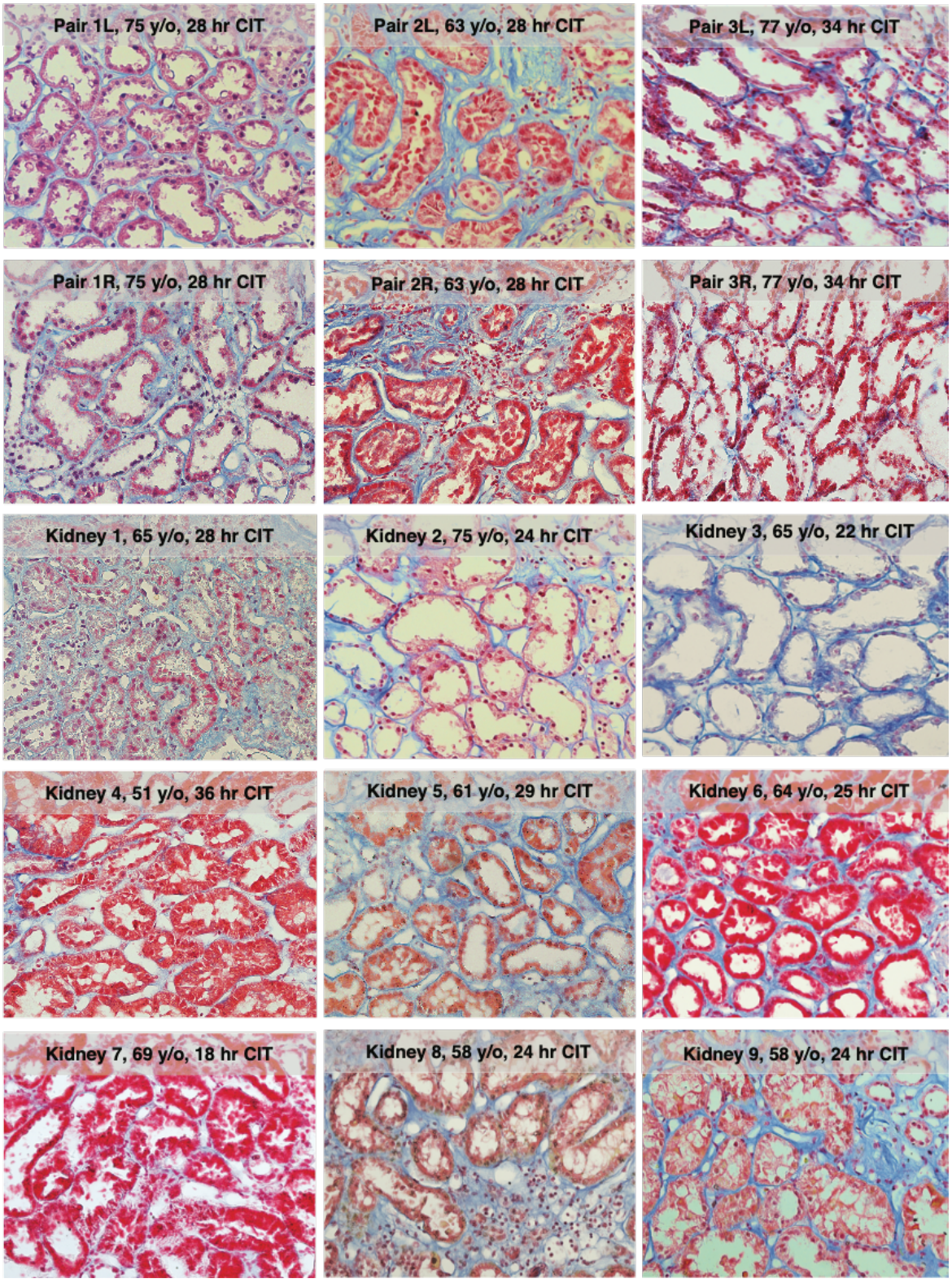

Fig. 2.7 **Tubular staining during cold storage of transplant discarded kidneys.** Images from a cohort of transplanted kidneys that display various levels of tubular epithelial staining during cold storage.

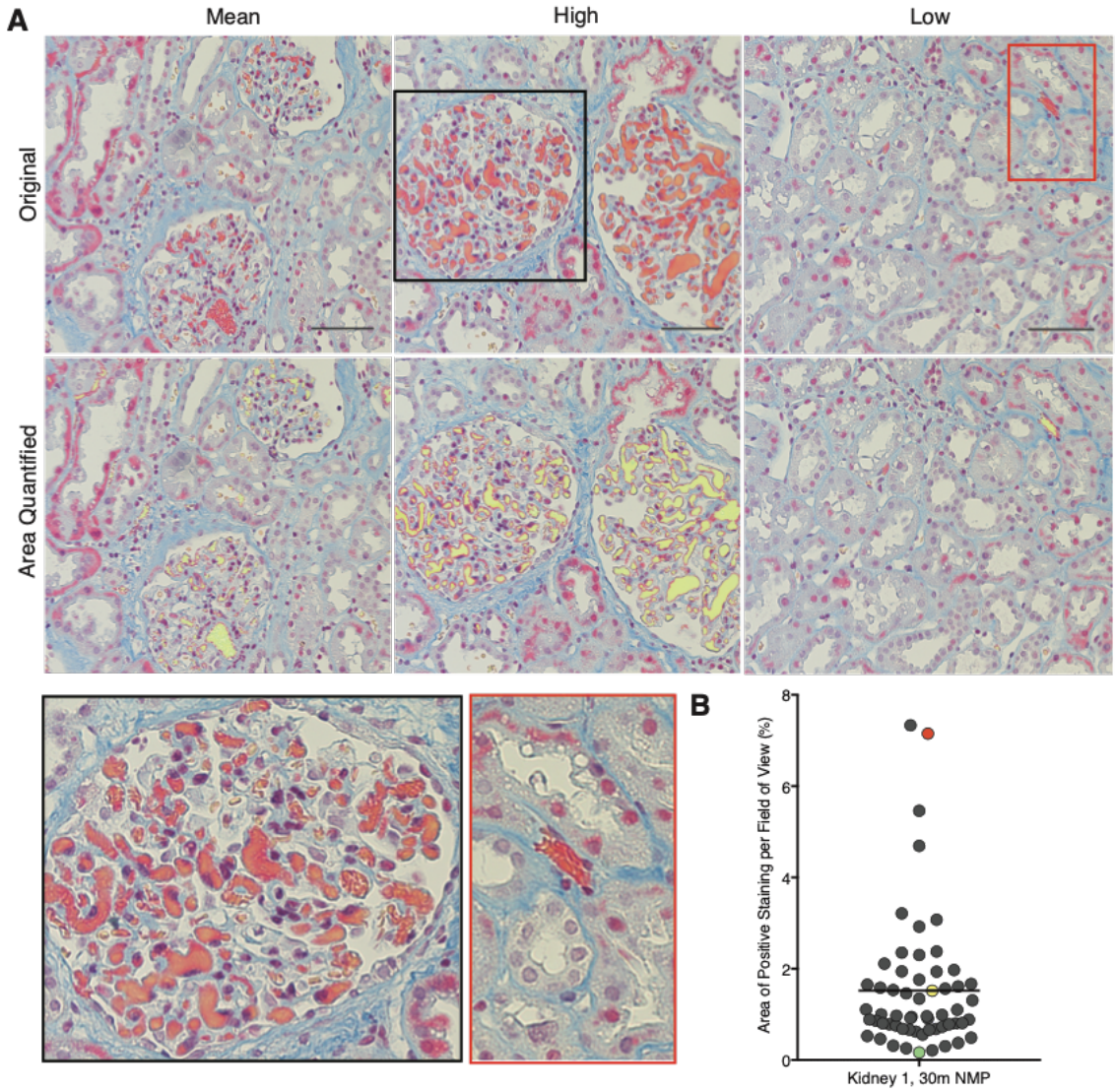

Fig. 2.8 **Demonstration of digital pathology approach to quantify color features following MSB histochemical stain.** (A) Representative images from different fields of view collected from the same individual section of a human kidney biopsy. Images show average, high, and low microvascular obstructions areas demonstrating the inherent variability of the samples (top and bottom enlarged panels). The machine-learning based digital pathology approach identifies the specific color associated with the feature of interest (middle panel yellow stain). Scale bars represent 100 μm. (B) Representative distribution for quantification of microvascular obstructions of 4x sections from a biopsy collected after 30 min of NMP. This demonstrates the broad distribution and need for a robust method of quantification as I have developed here. Red, yellow, and green data points refer to the corresponding images from panel (A) of high, average and low areas of microvascular obstruction respectively.

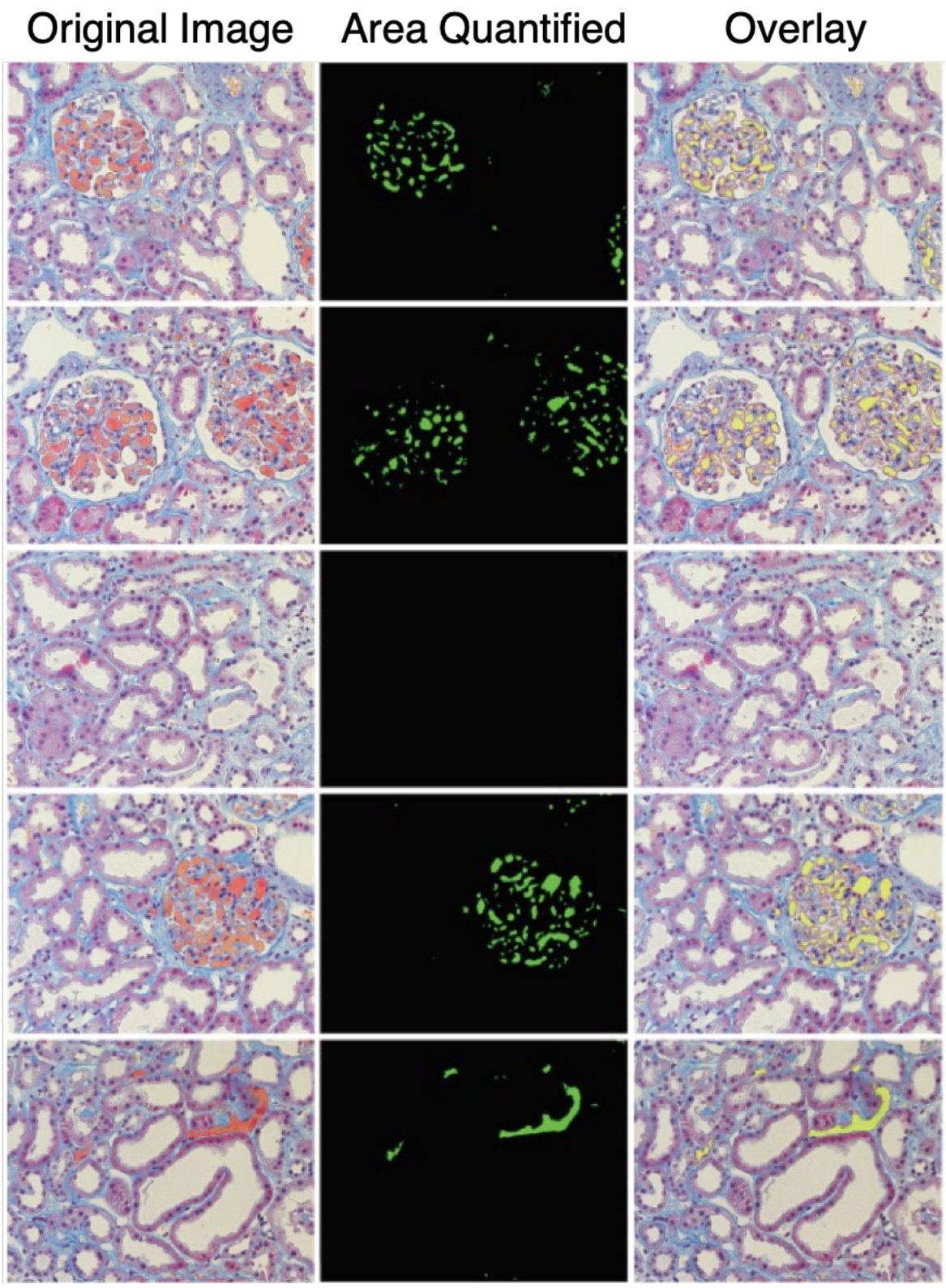

Fig. 2.9 **Demonstration that digital pathology approach provides robust quantification of microvascular obstructions (single donor organ).** Representative images depict robustness of the custom MATLAB code to isolate microvascular obstructions across a series of images from a single donor. Samples, all stained with Martius scarlet blue, are able to distinguish areas of collagen (blue), fibrin(ogen) (red), red blood cells (yellow), and microvascular obstructions where red blood cells and fibrin(ogen) overlap (left). The highlighted area of fibrin(ogen) is identified, exported as a mask (middle) and overlaid on the original image to ensure all positive areas are quantified (right).

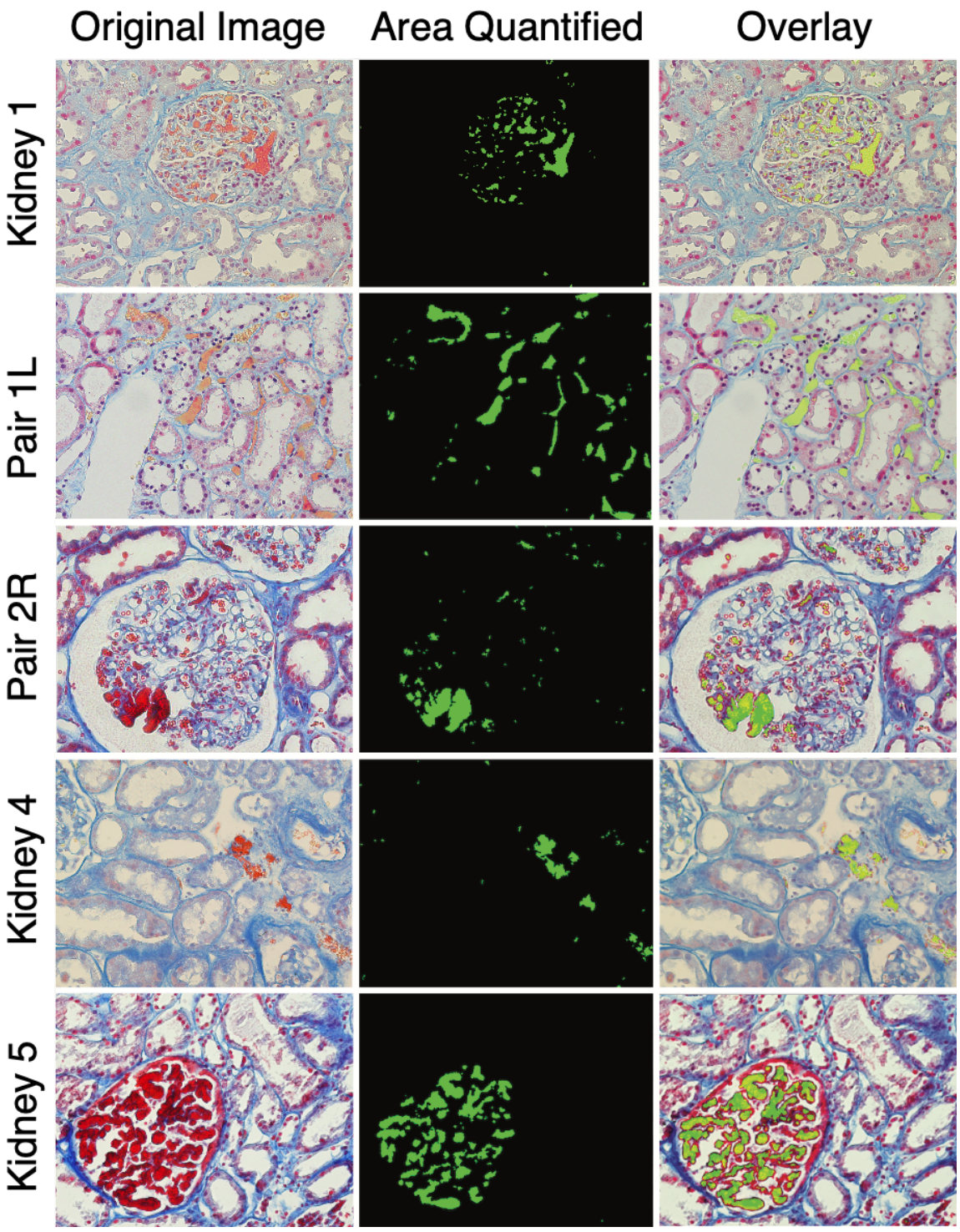

Fig. 2.10 **Demonstration that digital pathology approach provides robust quantification of microvascular obstructions (across multiple donors).** A key challenge of digital pathology is the variation of color schemes between different sample preparations. This variability is demonstrated here between different donor samples which have different hues of colors for the background (e.g. blue collagen) and features of interest (microvascular obstructions). This approach circumvents the issue by using a machine learning approach that is unique to each individual donor. Those allows for robust quantification across all donor samples (middle and right columns).

Table 2.3 **Pathologist's assessment of microvascular obstructions.** Pathologist's findings from blinded biopsies are presented above.

Pathologist's assessment	Time point	Treatment group
50–70% glomeruli have positive staining. Majority are global. Few are segmental. Focally positive areas of positive staining in peritubular capillaries.	30 min NMP	tPA + Plasminogen
Peritubular capillaries and glomeruli are completely negative.	90 min NMP	tPA + Plasminogen
Glomeruli are negative. Peritubular capillaries are negative. Noted different epithelial staining.	Cold storage	Plasminogen
More than 50% glomeruli are staining positively. Predominantly global. Focally positive areas of positive staining.	30 min NMP	Plasminogen
80% of glomeruli are staining positively. Predominantly global. Peritubular capillaries demonstrate more positive staining.	90 min NMP	Plasminogen

Though the organs in this sequential series were not matched for demographic characteristics, I nevertheless assessed indicators of physiologic function in the tPA + plasminogen group relative to controls. Vascular resistance spiked to higher levels in the tPA only group between 30-60 min of NMP (Figure 2.6C). In contrast, the tPA + plasminogen group displayed more stable resistance throughout NMP. While the tPA + plasminogen group appeared to diverge from the controls prior to addition of tPA, it should be noted that plasminogen was in circulation from time 0 and endogenous renal production of tPA has been previously reported [93]. In addition to the more stable hemodynamics, the tPA + plasminogen group produced significantly more urine than the tPA only group (Figure 2.6D). Collectively, these data suggest that plasminogen is essential for efficacy of tPA and that this approach can effectively clear microvascular obstructions during NMP.

2.4 Organ viability improves following treatment regimen

To more directly evaluate the effect of this treatment on organ viability, I evaluated 3 sequential pairs of transplant-declined organs recovered from 3 separate deceased donors (Figure 2.11B). The use of paired organs from the same donor is intended to better control for donor to donor variability for physiologic assessment. The three donors were aged 75 (Pair 1), 63 (Pair 2) and 77 (Pair 3) and were declined for suspected malignancy, biopsy

score and patient refusal respectively (Table 2.2). Cold storage times ranged from 28 to 34 hours and the cohort included both DCD and DBD donors. The paired organs were randomly assigned to receive either the combined tPA + plasminogen or plasminogen alone while undergoing NMP. Plasminogen was chosen as the negative control in this series to evaluate if the exogenous tPA was necessary or if endogenous tPA produced by the kidney was sufficient for full therapeutic effect.

The organ pairs were perfused simultaneously on identical perfusion systems and repeat biopsies were again collected at the same 3 time points: (1) at the end of cold-storage prior to NMP to confirm fibrinogen presence in tubular epithelia; (2) after 30 min of NMP to allow release in to the vasculature; and (3) after an additional 60 min of NMP either in the presence of tPA + plasminogen or plasminogen alone. Quantification of the microvascular obstructions revealed donor-to-donor variation in the initial levels of obstructions with Pairs 1 and 3 (75 y/o DCD and 77 y/o DCD) showing significantly higher initial values compared to Pair 2 (63 y/o DBD). Regardless of the initial level of obstruction, the combined tPA + plasminogen treatment completely eliminated all microvascular obstruction by the 90 min time point (from start of NMP) of the final biopsy (Figure 2.11A and B). By contrast, plasminogen alone led to only a minor reduction in Pairs 1 and 3 with high levels of microvascular obstruction remaining in all organs at the end of the NMP course.

To further confirm the results obtained via quantitative microscopy, levels of active plasmin (i.e. the activated enzyme) and fibrin(ogen) degradation products in the perfusates were evaluated. As expected, plasmin levels significantly increased in the kidneys treated with combined tPA + plasminogen (* $p < 0.01$; Figure 2.12A). Similarly, fibrin(ogen) degradation products (FDPs) also increased significantly after administration of combined tPA + plasminogen (* $p < 0.01$; Figure 2.12B). Modest effects were observed in the plasminogen only control likely reflecting endogenous production of tPA by renal endothelium as suggested in the prior series. Nevertheless, only the exogenous tPA + plasminogen treatment provided rapid and complete fibrin(ogen) cleavage (Figure 2.11B).

Next, parameters of physiologic function and organ injury in the treated organs relative to the paired controls were assessed. Treated organs demonstrated more stable vascular resistance as compared to non-treated organs which had a characteristic spike in resistance between 30-60 minutes (Figure 2.11C). The volume of urine production was also numerically higher in the treated organs by an average of 2.3 $\pm$0.6-fold, though this did not reach statistical significance with only 3 pairs of kidneys due to the relatively large variance between donors (Figure 2.11D). Urinary NGAL, a marker of acute kidney injury was significantly reduced in the treated kidneys compared to the paired controls (Figure 2.11E).

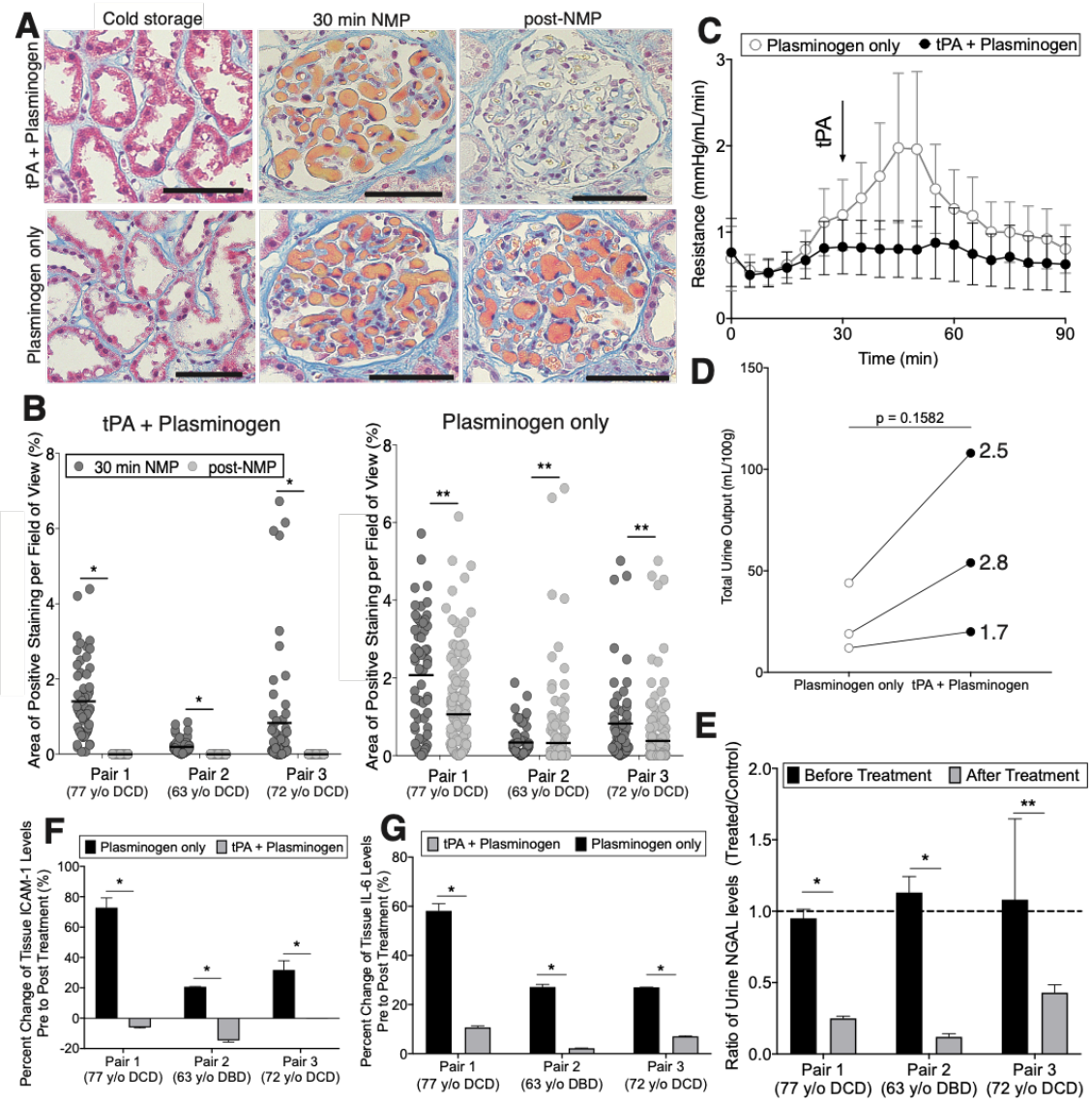

Fig. 2.11 **Assessment of paired donor organs suggests tPA + plasminogen improves organ viability.**(A) Representative images and microvascular obstruction quantifications (B) are shown from paired kidneys treated with tPA + Plasminogen or Plasminogen only (* $p < 0.0001$, ** $p < 0.05$; Mann-Whitney t-test). Scale bars represent 100 μm. (C) Resistance time traces as measured during NMP for Plasminogen only versus tPA + Plasminogen. Data points represent the mean of all kidneys evaluated. Error bars represent standard error of the mean. Arrow denotes point of tPA administration. (D) Total urine output was measured after 90 minutes of NMP (* $p = 0.1582$; paired t-test). (E) Urine NGAL ratios of tPA + Plasminogen to Plasminogen only controls for Pairs 1-3 before and after treatment (* $p < 0.00001$, ** $p = 0.018754$; multiple t-tests). (F) ICAM1 (* $p < 0.001$; multiple t-tests) and (G) IL-6 levels from tissue lysates (* $p < 0.00001$; multiple t-tests) in Pairs 1-3. Samples were processed in triplicate.

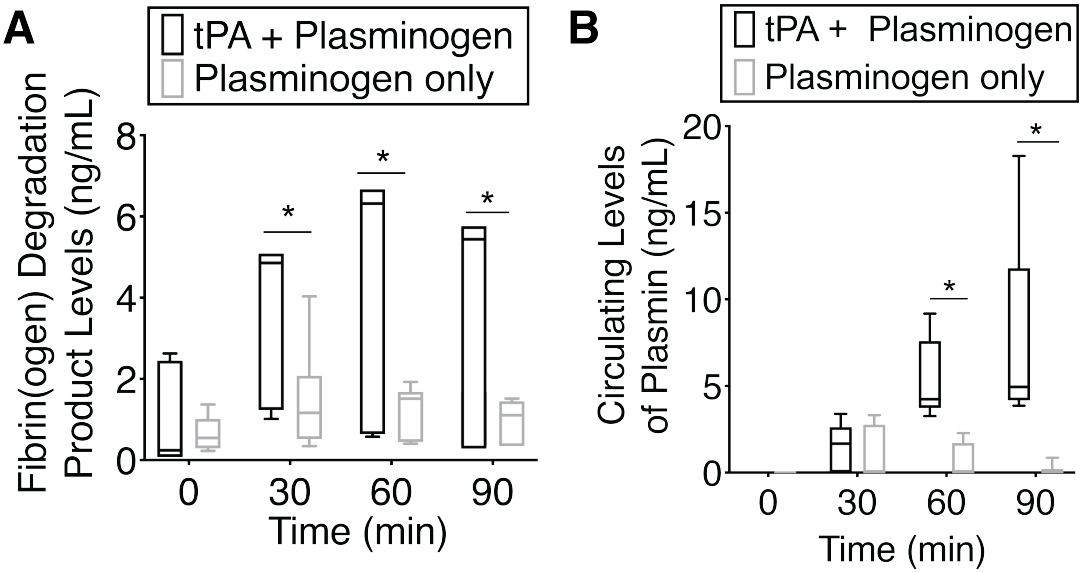

Fig. 2.12 **Biochemical assessment of paired kidneys after tPA and plasminogen treatment.** (A) Fibrin(ogen) degradation product levels (multiple t-tests; * $p < 0.05$ and (B) plasmin levels (multiple t-tests; * $p < 0.00001$) are presented throughout the course of 90 minutes of NMP from Pairs 1-3.

Finally, changes in protein levels of soluble ICAM1 and IL-6 were measured from pre (i.e. at end of cold-storage) to post NMP. Soluble ICAM1 - an enzymatically cleaved version of the cell-surface adhesion molecule, present in a wide variety of pathological states - was reduced by significant levels in the tPA + plasminogen group compared to plasminogen only controls (Figure 2.11F) [94–97]. Similarly, levels of IL-6 - a rapidly produced mediator of inflammation in renal IRI - rose in the perfusate to markedly higher levels in control organs compared to the combined tPA + plasminogen group (Figure 2.11G) [98, 99]. Collectively, these data confirm the effectiveness of using tPA + plasminogen to clear microvascular plugs and suggest that doing so leads to improvements in organ viability.

2.5 Tubular epithelia produce fibrinogen in response to cold time

The donor organs from the clinical series evaluated above displayed positive MSB stain in 6/15 kidneys (40%) prior to transplant. This ratio rose to 11/12 kidneys (92%) with positive MSB stain in cold storage for the series of non-transplanted research organs with 12/12 demonstrating microvascular plugging post NMP. Notably, the cold-storage times of the 6 MSB positive kidneys in the clinical cohort was significantly longer than that of the MSB

negative organs (Figure 2.13). The cold-storage times of the transplant-declined research organs were even longer suggesting that this may be a determining factor in renal fibrinogen levels. Hypothermic preservation of kidney allografts is thought to largely suppress protein translation [100, 101]. However, based on this evidence, I hypothesized that fibrinogen levels may be changing during cold storage.

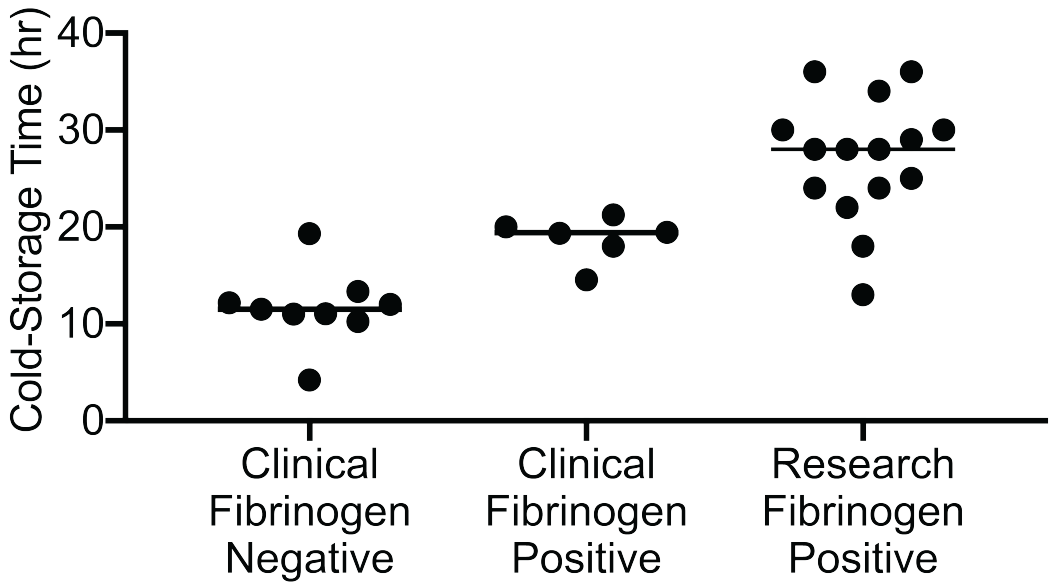

Fig. 2.13 **Cold storage times** Cold storage times are presented for clinical and research kidneys with fibrinogen negative or positive staining in tubular epithelium (* p = 0.0015; unpaired t-test).

To test this hypothesis, repeat tissue biopsies were collected from a 52 y/o DBD donor (Kidney 7) organ at 24 and 48 hrs of cold storage time and evaluated by western blot for the fibrinogen gamma subunit (52 kDal). An increase in fibrinogen levels was observed at 48 compared to 24 hours (Figure 2.14A). To investigate this in further detail, a series of five transplant-declined human organs were obtained early in cold storage (6-12 hours) and subsequently stored for prolonged cold periods with repeat sampling of biopsies collected out to 72 hours. Two organs from younger donors (Kidney 8 from a 49 y/o DBD and Kidney 9 from a 39 y/o DCD) were negative for MSB stain at the earliest time of 12 hrs. However, the MSB staining showed a clear time-dependent increase in tubular staining out to 72 hours (Figure 2.14B). A fibrinogen-specific ELISA performed on tissue lysates also demonstrated a linear increase of fibrinogen levels during this period consistent with the MSB staining (Figure 2.14C).

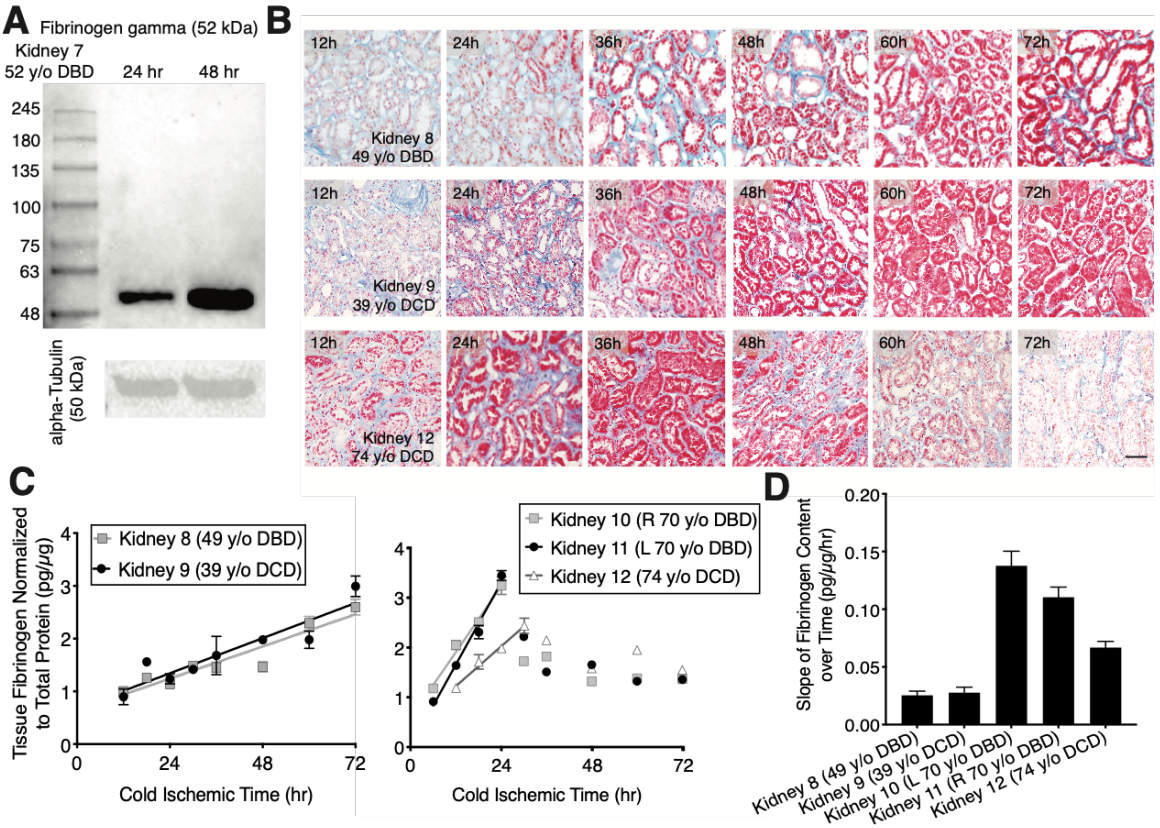

Fig. 2.14 **Tubular epithelia produce fibrinogen during cold storage at variable rates depending on the donor.**(A) Fibrinogen western blot and alpha-Tubulin loading controls from Kidney 7. (B) Representative images of sections taken from repeat biopsy of a 49 y/o DBD, 39 y/o DCD, and 74 y/o DCD kidney over the course of 72 hr. MSB stain shows increasing fibrinogen accumulation in tubular epithelia during cold-storage (red). Scale bar represents 100 μm. (C) Fibrinogen ELISAs performed on tissue lysates from repeat biopsies in 5 kidneys from 4 separate donors taken over the course of 72 hr (left - younger donors; right - older donors). Lines represent a fit to the linear phase of fibrinogen production. (D) Rate of fibrinogen production for each organ as derived from fits in (C). Error bars refer to SD. All measurements were taken in technical triplicate.

In the older donors (Kidney 10 and 11 from the same 70 y/o DBD; Kidney 12 from a 74 y/o DCD), an initial linear phase of fibrinogen increase was observed within the first 24-30 hours, followed by a subsequent period of decay perhaps due to some type of enzymatic degradation subsequent to cell death (Figure 2.14B and C). The organs from the older donors had significantly faster rates of fibrinogen increase compared to the younger donors (Figure 2.14D). Within 24-30 hours, the organs from older donors reached levels that took 72 hours to achieve in the organs from the younger donors. Notably, older donors are known to be more susceptible to damage from cold-storage preservation [102].

2.6 Improved specificity of targeted nanoparticles following treatment

The process of RBC plugging during NMP was initially discovered due to the non-specific accumulation of vascular-targeted nanoparticles (NPs) at the obstructed sites [74]. Therefore, I hypothesized that vascular-targeted NPs given after tPA + plasminogen treatment on NMP would show more selective targeting after restoration of microvascular perfusion. To evaluate this, another series of 3 sequential pairs of non-transplanted donors organs were evaluated (Pair 4 - 77 y/o DBD; Pair 5 - 53 y/o DBD; and Pair 6 - 76 y/o DBD). Based on the preceding data, each organ was held to a minimum of 30 hours cold-storage time to ensure high levels of fibrin(ogen) and subsequent microvascular plugging. Organs on NMP were either treated with tPA + plasminogen or untreated to replicate the conditions of the prior study [74]. Similar to the two-prior series, the treated organs demonstrated improvements in stability of hemodynamics (Figure 2.15A); urine production (Figure 2.15B) and reduced urinary NGAL as a marker of renal injury (Figure 2.15C).

To evaluate the efficacy of vascular targeted nanoparticle (NP) delivery, I repeated the previously published experimental design of co-administration of targeted and non-targeted NPs during NMP with and without the tPA + plasminogen treatment. Here, otherwise identical NPs were loaded with either red fluorescent dye and conjugated with an anti-ICAM2 antibody or loaded with a matched intensity of a green fluorescent dye and conjugated with a non-binding matched isotype control. (I was unable to use the anti-CD31 antibody employed in the prior study because the epitope recognized by this antibody appeared to be eliminated by the tPA + plasminogen treatment; Figure 2.16.) The NP were co-administered in both of the paired organs at 90 min after the initiation of NMP (to allow for the 60 min tPA + plasminogen treatment in the treated organ). Both paired organs were perfused for an additional 4 hours and end point biopsies were collected to assess the specificity of NP

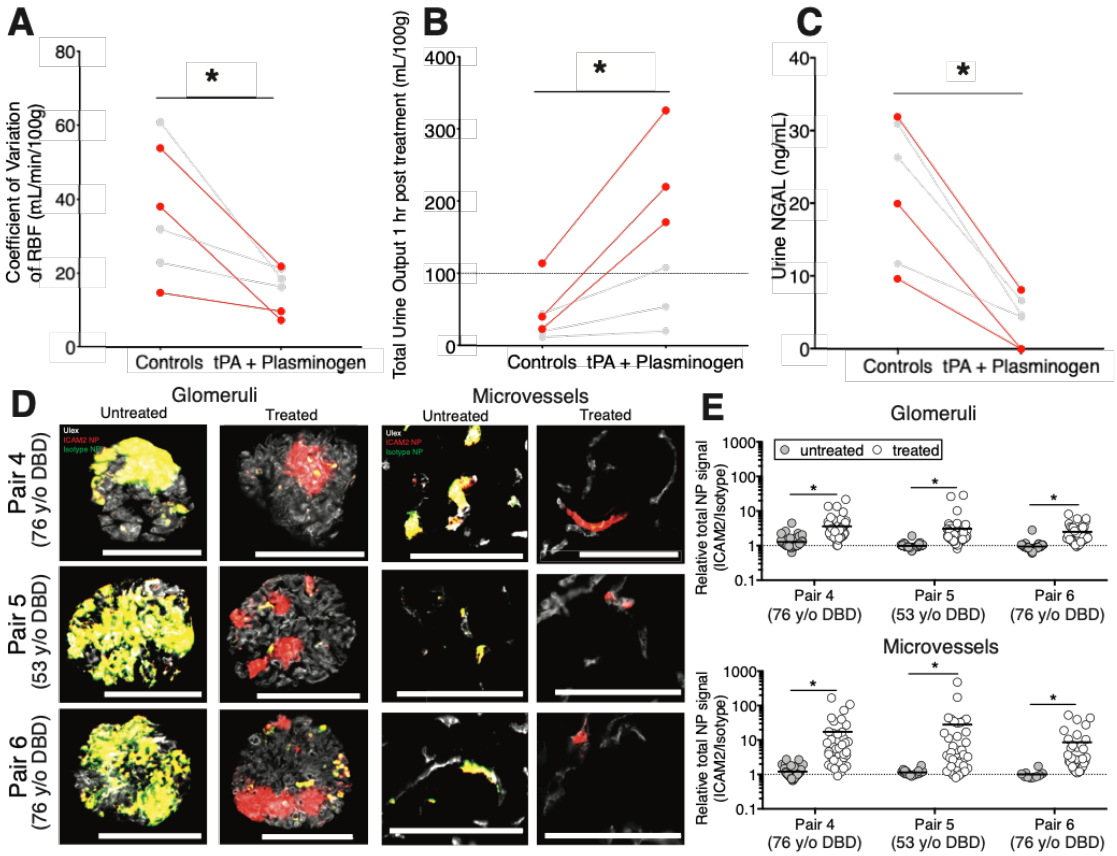

Fig. 2.15 **Lysing vascular obstructions improves specificity of vascular-targeted nanoparticles.** (A) Variation in renal blood flow (RBF) with or without treatment (* p = 0.0126; paired t-test). (B) Total urine production after one hour of NMP with or without treatment (* p = 0.0157; paired t-test). (C) NGAL levels in urine after one hour with or without treatment (* p = 0.0023; paired t-test). Red data points are from Pairs 4-6 that were stored for prolonged cold times of 30-36 hrs to build high fibrinogen levels. Each data point represents the outcome from a single kidney. (D) Representative images of glomeruli (left) and microvessels (right) from paired kidneys receiving either tPA + plasminogen treatment (treated) or NMP alone (untreated) prior to injection of combined ICAM2-NPs and Isotype-NPs labeled with two separate fluors (ICAM2-NPs, red; Isotype-NPs, green; NP-overlay, yellow; Ulex, white). Scale bars represent 100 μm. (E) Quantification of relative NP signal (ICAM2-NPs/Isotype-NPs) at 4 hours of NP circulation. Each point represents an individual image of either interstitial microvessels (top) or glomeruli (bottom); nonspecific (1:1) accumulation is represented by a dashed line (* $p < 0.0001$; Wilcoxon signed-rank test). Each data point represents an image taken from a section of a kidney.

targeting via quantitative microscopy to evaluate relative accumulation of the red ICAM2 NP and green Control-NP.

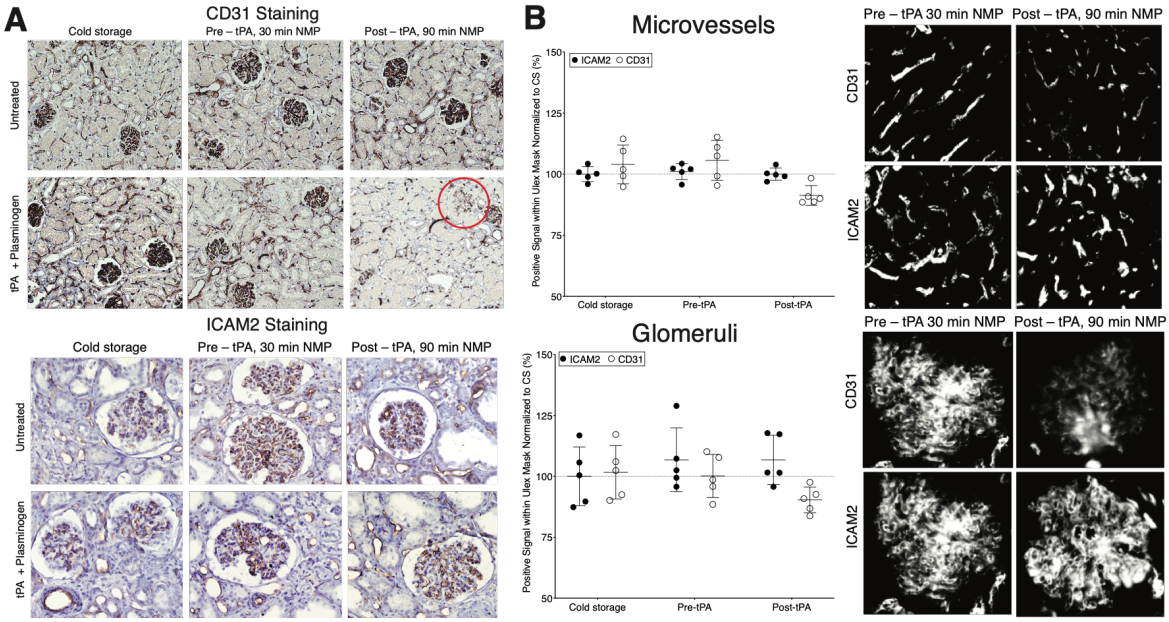

Fig. 2.16 **tPA and plasminogen treatment lyses CD31 epitope** (A) IHC staining of CD31 (10x) and ICAM2 (20x) images during cold storage, at 30 min of NMP and at 90 min of NMP with or without tPA + plasminogen treatment. (B) Quantitative microscopy calculations of fluorescent CD31 and ICAM2 staining during cold storage, at 30 min of NMP and at 90 min of NMP with or without tPA + plasminogen treatment in microvessels and glomeruli.

In the absence of tPA + plasminogen treatment, there was no observed benefit of NP targeting. ICAM2-NP and Control-NP accumulated at identical levels presumably via a sieving mechanism at the site of vascular obstructions, as previously observed (Figure 2.15D and E) [74]. However, in the paired kidney the retention of the non-targeted Control-NP were significantly diminished in the absence of the microvascular obstructions. The ICAM2-targeted NP were retained in areas of both glomerular and peritubular capillary microvasculature. The quantitative microscopy approach revealed ~3-fold retention benefit in the glomeruli ($p < 0.0001$) and ~20-fold benefit in the microvessels ($p < 0.0001$) (Figure 2.15E). The targeting benefit in glomeruli was similar to what was observed in well perfused kidneys in the previous pervious chapter, while targeting to the microvessels improved ~10 fold from the initial study [74]. These data suggest that clearance of microvascular obstructions is likely an essential precursor for effective delivery of targeted nanomedicines to renal endothelium during NMP.

Discussion

The basic principles for successful preservation of organs for transplant were established during pioneering studies in the late 1960s through late 1980s [103–105]. These efforts defined 5 key physiologic modes of failure to be addressed during preservation: 1) Hypothermia-induced cellular swelling due to impaired Na+ pump activity at cold temperatures; 2) Ischemia-induced intracellular acidosis; 3) Tissue edema from imbalance of osmotic pressures; 4) Reperfusion-induced production of reactive oxygen species; and 5) Depletion of substrates for ATP regeneration following reperfusion. Based on these 5 pillars, preservation fluids (e.g. University of Wisconsin solution) were designed to enable safe preservation of deceased-donor kidneys for ~24 hr [103]. However, these principles of safe preservation were established in an era with much less demand for organs and a donor population that was generally healthier. The poorer outcomes associated with more marginal donor organs prevalent today - even within the standard preservation cutoff times - suggests the possibility that there may be additional as yet unidentified modes of failure that need to be addressed to ensure these higher-risk organs can be safely preserved and transplanted.

The ability to perform preclinical research on the same non-transplanted organs that the community looks to revitalize provides a unique opportunity to identify these additional failure modes. This discovery process is further aided by the capacity of NMP to simulate *in vivo*-like conditions in a controlled *ex vivo* setting. The phenomenon uncovered in this study was identified as a direct result of the fact that *ex vivo* NMP can mimic how higher risk organs would behave *in vivo* post-transplant. The isolated setting of NMP further allowed me to identify renal tubular epithelium as the source of fibrinogen by eliminating the confounding source of hepatic fibrinogen. Thus, in the context of pre-clinical research, the approach employed here can enable discovery of new mechanisms of human pathophysiology that are intrinsic to a given organ type.

Regarding the specific mechanisms driving microvascular obstructions during NMP, the data suggest that factors produced within the kidney are sufficient to elicit these lesions. The fact that the obstructions are densely positive for fibrin(ogen) further suggests that the observed time-dependent increase in fibrinogen levels during cold-storage is central to this process. Nevertheless, the data do not conclusively demonstrate that renal fibrinogen is sufficient to drive the obstructions in the absence of other co-factors. Von Willebrand Factor has also been identified as a mediator of RBC-aggregation in the context of ischemia-reperfusion injury [106, 107]. Von Willebrand Factor, like fibrin(ogen), is also sensitive to plasmin degradation. Thus, there is a clear need for a future mechanistic investigation to complement the translational focus of this work. A comprehensive identification of the upstream regulators

of fibrinogen production and any other proteomic changes during cold storage may inform alternative therapeutic strategies with greater specificity than plasmin. This more detailed mechanistic study should also directly evaluate how hypothermic perfusion - a ubiquitous method of preservation in the U.S. and Europe - influences the rate of fibrinogen production and the formation of microvascular obstructions.

Though there may well be preferable alternatives to the therapeutic regimen developed here, the utility of this approach lies in its capacity for immediate translation. tPA is an FDA-approved therapeutic with a long history of use in the context of organ transplantation [91, 108]. Plasminogen is currently awaiting FDA-approval as a replacement therapy for patients with plasminogen-deficiency but has been shown in multiple clinical trials to be safe for use in humans [109–113]. In the U.K., the well-established clinical use of NMP will allow me to directly translate the regimen developed here within current clinical practice. While NMP is not currently in clinical use in the U.S., intra-arterial drip of low-dose tPA delivered ~10-15 min after transplant may be an effective strategy to achieve the same effect of clearing microvascular plugs in marginal organs with high levels of fibrinogen. In either case, the focus will be increasing utilization of the higher-risk organs that are currently being discarded in high numbers while patients die on the waitlist every day.

Given the high degree of variability present in marginal human organs, it seems unlikely that a one-size-fits-all approach will suffice for full pre-transplant revitalization. Indeed, I believe that the repair of marginal organs pre-transplant will likely require a personalized approach with therapies being adapted to the specific needs of a given organ. Within this paradigm, modular drug delivery systems (e.g. nanoparticles) hold significant promise due to their capacity to deliver a wide array of different therapeutic payloads including drugs, gases, proteins, nucleic acids, and gene-editing agents [7, 114, 115]. However, even the most well-suited therapies will not be effective if they can't reach the intended site of action. I propose that treating the microvascular obstructions identified here will be a critical first step in any pre-transplant treatment regimen. First and foremost, this will ensure adequate restoration of oxygen and nutrient delivery throughout the organ. However, these results suggest this approach will further potentiate use of the full toolkit of potential therapeutic options currently being explored for use during NMP. To begin building out a therapeutic toolkit, I next sought out to identify a drug that would be appropriate to load into nanoparticles and protect against renal ischemia-reperfusion injury.

Chapter 3

Delivering an NLRP3 inhibitor during normothermic machine perfusion

Having established better microcirculation for the improved delivery of targeted nanoparticles, I began to investigate different therapeutics that would be well suited to load into the targeted nanoparticles. As morbidity among the donor population continues to rise, more marginal kidneys, with high sensitivity to ischemia reperfusion injury (IRI), are being offered for renal transplantation [6, 5]. As there are currently no pre-transplantation therapies that work to minimize the effects ischemia reperfusion injury, thousands of these susceptible organs are discarded annually [116]. I hypothesize that targeting IRI with therapeutics prior to transplantation may be a viable strategy in increasing patient access to marginal organs.

Post-transplant IRI can result in acute kidney injury manifested as delayed graft function, which may ultimately impact long term graft survival [5]. IRI is multifactorial a process that is a result of the restoration of normoxic conditions following transplantation [6, 14]. A critical mechanism in IRI is the intracellular assembly and activation of the NLRP3 inflammasome, which triggers production of inflammatory caspases and the maturation of the prototypic inflammatory cytokines IL-1β and IL-18 [17, 16]. Inhibition of the NLRP3 inflammasome has been proposed as a therapy to prevent IRI, but to date, relevant therapies have been delivered entirely in *in vivo* animal models [17, 117, 18, 118]. Biodistribution challenges, off-target effects, and the need for increased dosing are commonly associated complications of *in vivo* drug delivery which ultimately hinder translation of a therapy to bedside care [119]. Additionally, in order for NLRP3 inhibition to be effective in protecting against IRI, the therapy must be delivered before transplant.

Emerging technologies, like renal *ex vivo* normothermic machine perfusion (NMP), have allowed us to deliver therapeutics pre-transplantation in a clinically relevant setting. As

previously discussed, NMP serves as a unique platform for the delivery of pre-transplant therapies *ex vivo* [120, 74]. On an isolated circuit, therapies can be delivered directly to the organ of interest without the usual challenges of systemic delivery (e.g. off-target drug effects, systemic toxicity) [119]. Delivering NLRP3 inhibitors in this setting will allow us to treat the organ, rather than the patient, prior to transplantation.

In this chapter I investigate MCC950, a selective NLRP3 hydrolysis inhibitor, to ameliorate renal ischemia reperfusion injury [121]. In murine and human organ culture models of renal IRI, I have shown that MCC950 has a protective effect. Additionally, I have demonstrated that NMP provides a highly effective platform for the isolated delivery of pre-transplant therapies. I propose that blockade of the NLRP3 inflammasome with MCC950 may be a viable therapeutic strategy in the search for interventions that may improve early allograft function. MCC950 may be an optimal drug to load into targeted nanoparticles for prolonged delivery and protection against IRI and increase marginal organ utilization.

3.1 NLRP3 inhibition with MCC950 is protective against renal ischemia reperfusion injury in mice

Activation and assembly of the NLRP3 inflammasome has been shown to be a key mechanism in the regulation of renal IRI [17, 16]. To assess if inhibition of the inflammasome was protective against IRI I applied a bilateral clamp model of renal IRI wild type (WT) and NLRP3 knockout mice [122]. Using serum creatinine and blood urea nitrogen (BUN) as clinically accepted markers for renal injury, NLRP3 knockout mice had lower levels of serum creatinine and BUN than WT mice (Figure 3.1, A and B) [123]. Additionally, there were also significantly reduced levels of tubular necrosis in the outer strip of the medulla, the portion of the kidney most sensitive to ischemia reperfusion injury (Figure 3.1, C and D). Both WT and NLRP3 knockout mice had similar basal levels of serum creatinine, BUN, and tubular necrosis in sham conditions (Figure 3.1, A-D). Previous, similarly executed experiments support these findings [122, 124].

Confirming that an NLRP3 knockout is protective against IRI, I next sought to test if a small molecule inhibitor of NLRP3, delivered just prior to clamping, could produce the same phenotype. I chose to investigate MCC950, a small hydrophobic drug, that has been shown to act as a potent NLRP3 inhibitor by directly targeting the NLRP3 ATP-hydrolysis motif [121]. When MCC950 (7.5 mg/kg) was delivered systemically intravenously to mice subjected o renal IRI, there was a significant reduction in both serum creatinine and BUN levels (Figure

3.1, A and B). Historically, MCC950 has been delivered intravenously in mice at doses between 3 and 10 mg/kg, suggesting that I am administering a dose within the correct range to observe an effect [125, 126]. There was a significant reduction in levels of tubular necrosis following MCC950 treatment (Figure 3.1, C and D). However, the same reduction in injury markers that was seen in the full NLRP3 knockout model was not observed. I hypothesize that the obstacles of effective systemic drug delivery (i.e. phagocyte-mediated elimination, off-target effects) may have contributed to the incomplete attenuation of these injury markers [29]. Having shown that NLRP3 inhibition with MCC950 has promise in reducing the effects of IRI *in vivo*, but does not have a full protective effect, I next moved to deliver MCC950 to human kidneys on an isolated *ex vivo* NMP circuit in an attempt to obviate the challenges of *in vivo* drug delivery.

3.2 Organ culture models serve as a platform for dose titration studies

To identify the optimal dose of MCC950 for human organs *ex vivo*, models of organ culture were utilized. Organ culture allows us to preserve tissue architecture and cellular interactions that may not be possible in standard cell culture assays [127]. Additionally, this method enables us to turn one whole organ into potentially thousands of replicates. In this study, dissected tissue from 4 separate human kidneys was incubated in various concentrations of MCC950 previously used in the literature (Table 1). Following the period of treatment, the tissue was challenged with a period of hypoxia and then subjected to a model of reperfusion (Figure 3.2A). Measuring levels of IL-1β and IL-18 in the reperfusate, IC_{50} curves were constructed to determine the most appropriate concentration of MCC950 to deliver during NMP. In human organ culture models of IRI, a full reduction of both IL-1β and 1L-18 was noted at 100 μM of MCC950 and I chose to proceed with that concentration for NMP.

3.3 Normothermic machine perfusion of a kidney improves with NLRP3 inhibition

Here, when MCC950 was delivered to a series of 4 single kidneys on the *ex vivo* circuit (Table 3.1) there was improved total urine output and significantly higher renal blood flow measurements when compared to controls (Figure 3.3, A and B). As it takes a certain amount of time for the NLRP3 inflammasome to assemble, the organ was allowed to stabilize or 90 minutes prior to delivering MCC950. It is important to note that while these kidneys were

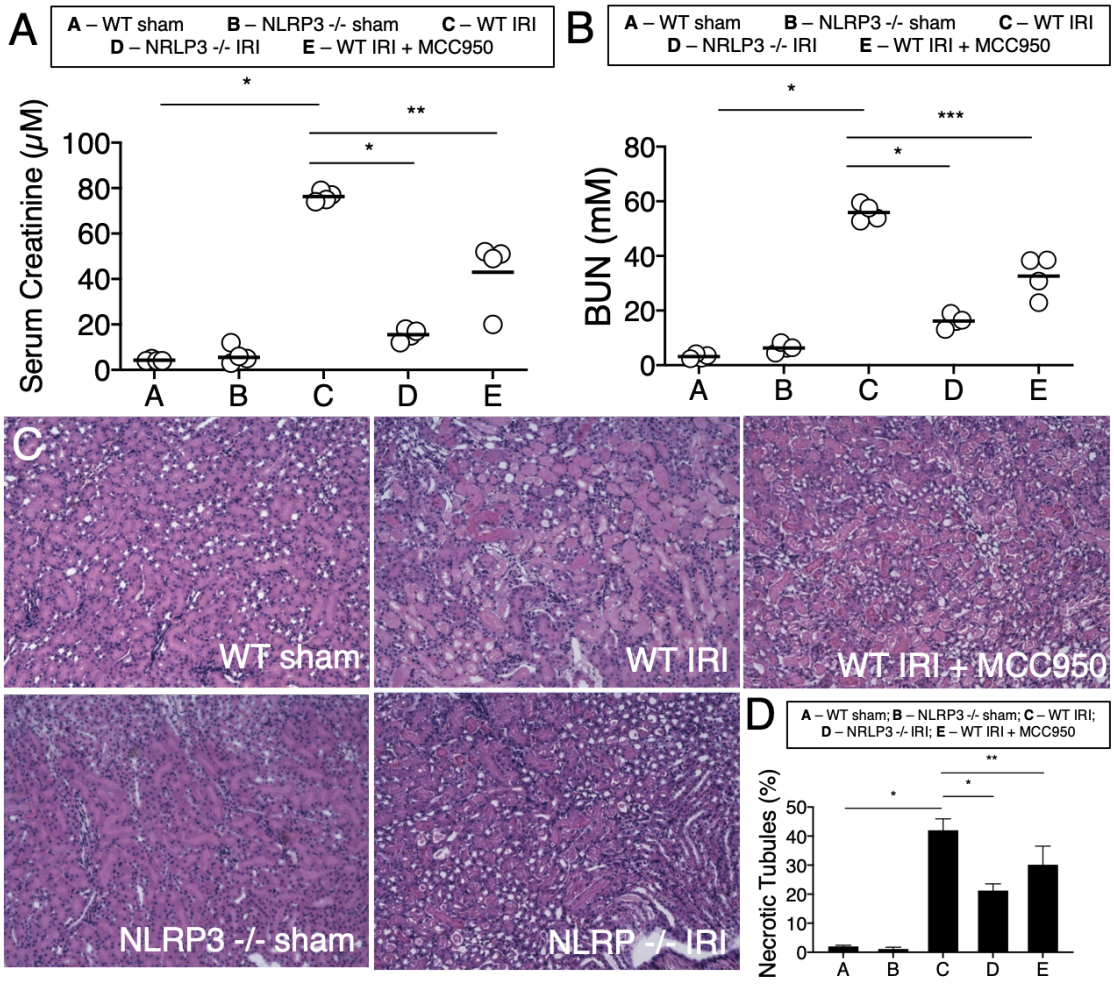

Fig. 3.1 **NLRP3 inflammasome inhibition protects murine kidneys from ischemia reperfusion injury.** (A) Serum creatinine and (B) blood urea nitrogen (BUN) levels (*$p < 0.0001$, **$p = 0.0052$, ***$p = 0.0012$; unpaired t-tests) are presented across all experimental groups of mice. Single data points represent individual mice in a group ($n = 4$). (C) Representative 20x images of the outer strip of the medulla are presented across all groups. (D) Percent of necrotic tubules were quantified in the outer strip of the medulla levels (*$p < 0.0001$, **$p = 0.0197$; unpaired t-tests).

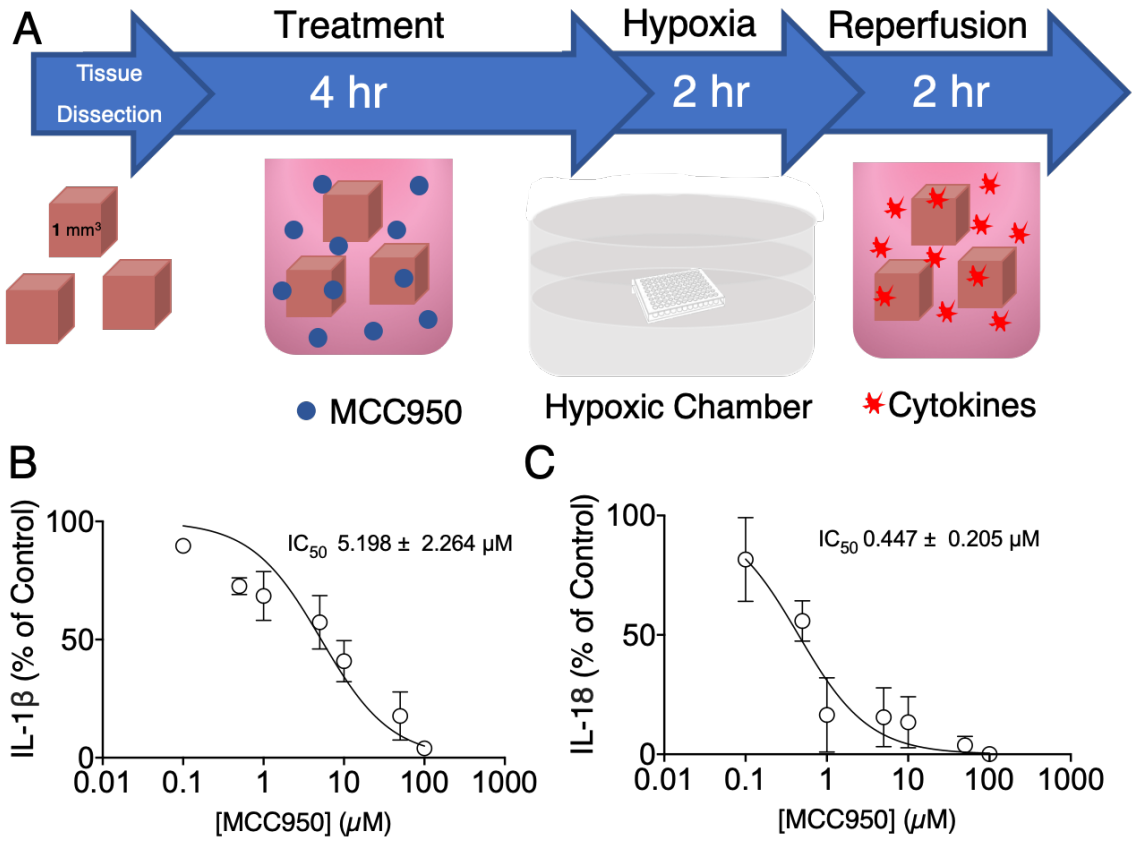

Fig. 3.2 **NLRP3 inflammasome inhibition is possible during human kidney organ culture.** (A) A schematic from the human organ culture experiments following static cold storage is presented. MCC950 dose response curves during human organ culture are presented for (B) IL-1β and (C) IL-18. Error bars represent SEM.

matched to be DBDs with long cold times, they did not come from the same donors, making paired analysis inappropriate for these measures. While perfusion parameters have been suggested to correlate with improved organ function, they have yet to be fully understood, suggesting other markers of organ health and function should be considered [128, 49, 27].

Table 3.1 **Donor demographics.** Donor demographics are presented for all transplant discarded human kidneys used in the presented experimental series.

Kidney ID	Age	CIT	Reason for decline	Treatment group
Kidney 1	73	14	high biopsy score	CS
Kidney 2	46	27	retrieval damage	CS
Kidney 3	63	17	no suitable recipient available	CS
Kidney 4	71	30	poor artery anatomy	CS
Kidney 5	76	33	age & long CIT	NMP + MCC950
Kidney 6	35	33	long CIT	NMP + MCC950
Kidney 7	68	27	suspected cancer	NMP + MCC950
Kidney 8	68	27	suspected cancer	NMP + MCC950
Kidney 9	63	26	suspected cancer	NMP + saline
Kidney 10	76	30	suspected cancer	NMP + saline
Kidney 11	53	36	suspected cancer	NMP + saline
Kidney 12	76	30	ATN	NMP + saline

Additionally, decreased levels of cytokine in the perfusate were observed after 4 hours of MCC950 circulation when compared to controls (Figure 3.3C). Higher cytokine levels during perfusion have been associated with higher levels of DGF post transplantation. Lower levels of cytokine production associated with MCC950 administration suggest that the treatment not only inhibits the NLRP3 inflammasome but in doing so better prepares the organ for transplantation. To confirm this, one must look beyond this period of treatment to see how the organ behaves longer term.

3.4 Human organ culture following normothermic machine perfusion serves as a model for IRI post-transplant

To evaluate how the organ responds post-NMP, methods of human organ culture can be utilized. Following treatment during NMP tissue can be dissected, challenged in a hypoxic chamber, and allowed to reperfuse to simulate what the organ may experience following an additional period of cold storage and transplantation (Figure 3.4A). Our preliminary evidence suggests that even 8 hours after the initial dose of MCC950, tissue produced

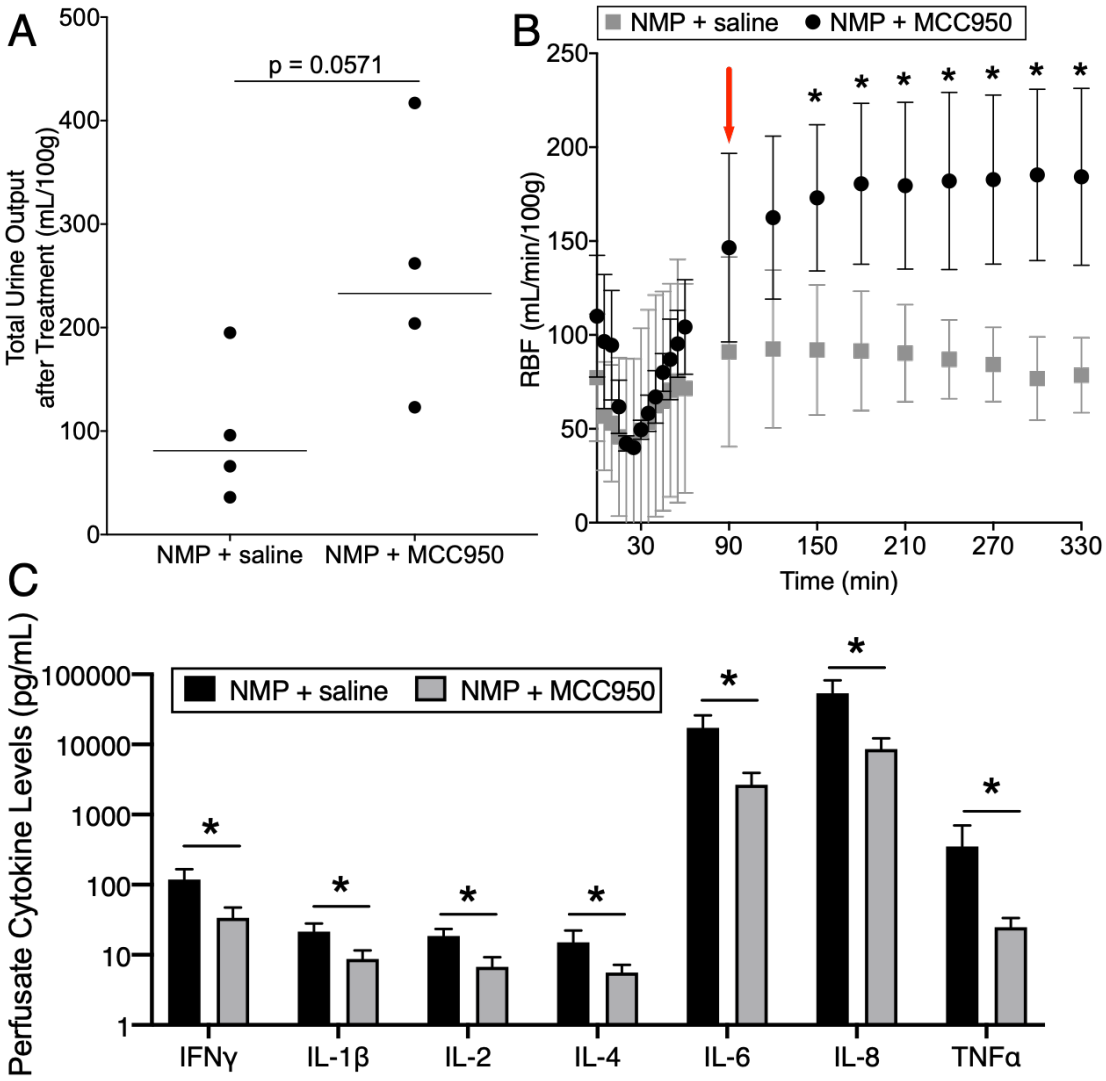

Fig. 3.3 **MCC950 delivery during renal NMP improves perfusion parameters.** (A) Urine output are presented from control (NMP + saline) and treatment (NMP + MCC950) groups. Each data point represents the output from an individual kidney. (B) Renal blood flow parameters are presented from control and treatment groups (*$p < 0.05$, multiple t-tests). (C) Perfusate cytokine levels are presented from control and treatment groups (*$p < 0.05$, multiple t-tests).

mostly undetectable levels of IL-1β (Figure 3.4B) and significantly less IL-18 (Figure 3.4C). These results support that delivering MCC950 during NMP may be a viable pre-transplant therapeutic strategy to protect marginal organs from IRI.

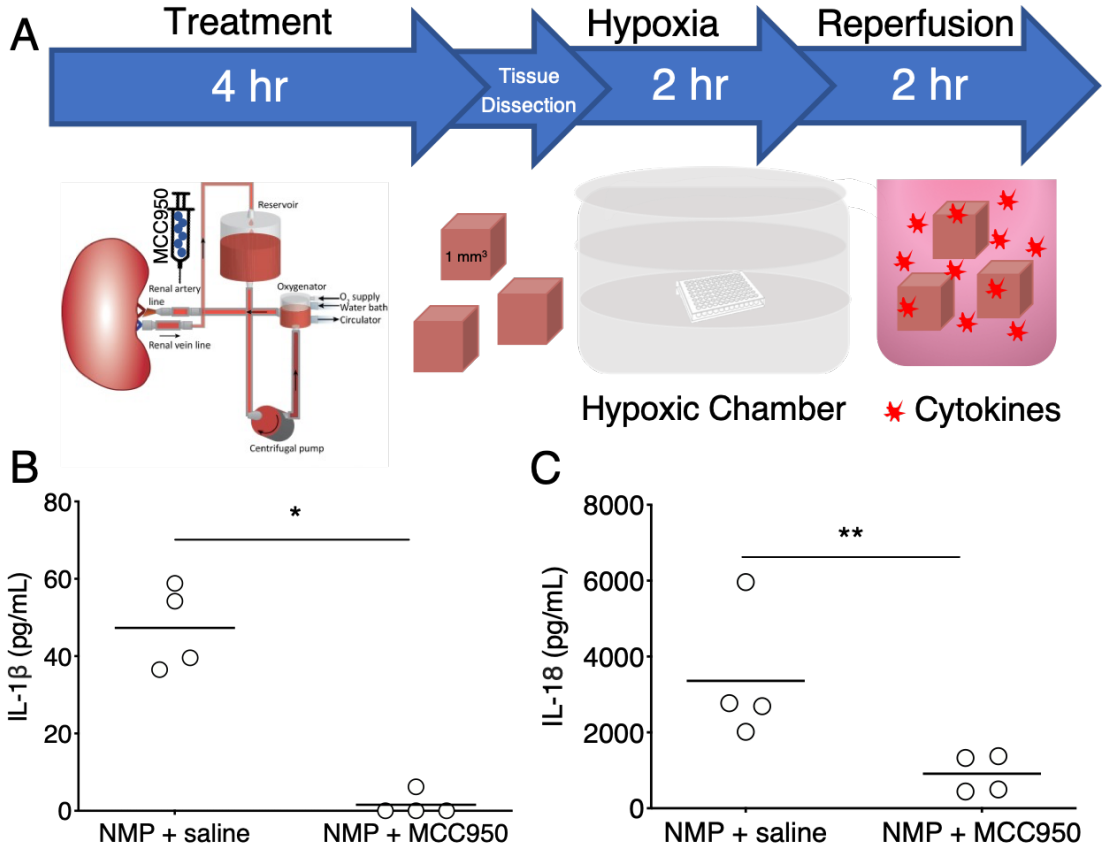

Fig. 3.4 **Human organ culture supports MCC950 delivery during renal NMP is protective against IRI.** (A) A schematic from the human organ culture experiments following normothermic machine perfusion is presented. (B) IL-1β (*p = 0.0002, unpaired t-test) and (C) IL-18 (*p = 0.0373, unpaired t-test) levels are presented from the reperfusion media following a period of normothermic machine perfusion.

Discussion

Although ischemia reperfusion injury is largely regulated by the NLRP3 inflammasome, this injurious process is known to be multifactorial and has yet to be completely understood [6, 14, 17, 16, 129]. Due to the nature of IRI, it is unlikely that the inhibition of a single pathway will fully ameliorate the long term effects of this process. To protect marginal organs from IRI following transplant, a dynamic therapeutic toolkit must be built to address multiple

mechanisms of injury and be adaptable to specific organ profiles. I chose to investigate MCC950, a small hydrophobic drug, that has been shown to act as a potent canonical and non-canonical NLRP3 inhibitor by directly targeting the NLRP3 ATP-hydrolysis motif [121, 126]. MCC950 has been studied in a variety of experimental models of inflammation and has been shown to alleviate colitis, stroke, asthma, and even Parkinson's disease [130–133]. Most pertinently however, in models of porcine liver transplantation, MCC950 administration has been shown to reduce IRI [134]. In this study, I demonstrated that delivering an NLRP3 inflammasome inhibitor *ex vivo* can protect marginal organs against IRI as one facet of a potential therapeutic strategy.

Methods of human organ culture help us to better understand the therapeutic efficacy of a treatment in question by allowing us to preserve tissue architecture and cellular responses that may be lost in cell culture models [127]. Additionally, this approach enables high throughput screenings of therapeutic agents and dosing by turning one human organ into theoretically thousands of replicates. As transplant-discard human organs are an extremely rare and valuable resource, it is important that transplant scientists continue to devise and implement strategies that maximize the potential of these gifts. Once initial screenings have been conducted and proper dosages have been determined in a human organ culture setting, scientists can move to more clinically relevant models and treat whole organs using *ex vivo* normothermic machine perfusion [26, 74].

As treatments are delivered to single organs on *ex vivo* perfusion circuits more frequently, it will become imperative that there is an understanding of (1) the intra-organ biodistribution of the drug administered and (2) whether or not there is a need to target these drugs to specific cell types in order to make them more effective therapeutics in the short window pre-transplantation [74, 30, 31, 24]. Targeting therapies has been shown to enhance the retention of drugs, allowing for more rapid cellular internalization [48, 39]. MCC950 is a small hydrophobic drug that, when delivered without a targeting ligand, will passively diffuse through the cellular membranes of all accessible cells types within a kidney through random drug-cell interactions [135]. As the NLRP3 inflammasome has only been shown to be active in the cytosol of innate immune cells (e.g. macrophages, monocytes, and dendritic cells) and some resident kidney cells (e.g. tubular epithelium and podocytes) it is likely that I delivered MCC950 at a higher than necessary dose to see a protective effect against IRI [136]. In the case that targeting MCC950 to multiple cell types is necessary for more effective treatment, one possible strategy is to encapsulate the drug into a polymeric nanoparticle carrier.

Using nanoparticle technologies also enables us to deliver encapsulated drugs over a prolonged period of time [137]. Polymeric nanoparticles can be formulated to slowly release

their contents over a period of hours, days, or even weeks as they degrade by hydrolysis [56, 7]. Although there is no current consensus on how long IRI persists post-transplantation, it has been shown that IRI in susceptible organs may result in acute kidney injury or graft loss [5]. Delivering therapeutic agents over a sustained period of time post-transplantation may help mitigate the deleterious effects of IRI. From this work, I propose that inhibition of the NLRP3 inflammasome may be one approach to protecting marginal organs from IRI. These pre-transplantation therapies may ultimately increase the rate at which these marginal organs are utilized for transplantation.

Chapter 4

Whole organ viability assessments

As previously discussed, *ex vivo* organ perfusion has emerged as both a clinical and research platform with the potential to improve safe utilization of marginal organs [138, 119, 139–141]. In the clinical context, *ex vivo* organ perfusion provides an opportunity for more detailed assessment of organ function to better stratify safe versus compromised donor organs. Indeed, recent clinical experiences in kidney and other organs suggest that *ex vivo* organ perfusion can improve utilization of organs that had been previously declined without sacrificing outcome [120, 138, 142, 143]. Parallel efforts in pre-clinical research have been exploring therapeutic strategies to potentially revitalize compromised organs to make them safe for transplantation [119, 144, 30, 31, 37]. In either setting, sophisticated diagnostic tools are essential to provide an objective and quantitative assessment of organs.

In the prior chapters, I have developed diagnostic imaging tools for quantitative assessment of biopsy specimens to evaluate delivery of targeted nanomedicines and to quantify the extent of microvascular obstruction during normothermic machine perfusion (NMP) of transplant-declined human kidneys [74]. Though this approach is useful for this type of higher-resolution detailed analysis, biopsy-based diagnostics have two key limitations: (1) Invasive-nature of the assessments limits the ability to perform longitudinal measurements of dynamic behavior; and (2) assessment is limited to the tissue within the biopsy and cannot provide a global assessment of the organ.

In this chapter, I sought to develop a complementary diagnostic tool that could overcome the limitations of biopsy-based assessments. I hypothesized that *ex vivo* tomography imaging could enable non-invasive and whole-organ diagnostic assessments. I specifically focused on evaluation of contrast-enhanced computed tomography (CT) as an assessment of organ perfusion characteristics; my prior work suggests that establishing good microvascular perfusion is a prerequisite for any subsequent therapeutic efforts at organ revitalization. In

a series of pig and non-transplanted human kidneys, I first developed quantitative tools for analysis of CT-image-stacks. I then utilized these tools for assessment of non-transplanted human organs either before, during or after normothermic machine perfusion. These data demonstrate the potential for *ex vivo* tomographic imaging as a preclinical research tool and suggests contrast-enhanced CT could also have potential utility for organ assessment in a clinical setting.

4.1 CT imaging to assess renal vasculature *ex vivo*

In the previous chapters, I have developed advanced quantitative microscopy tools to analyze biopsies collected before, during and after normothermic perfusion. However, the destructive nature of repeat biopsies limits the ability to perform dynamic assessments and restricts analysis to the collected tissue, precluding whole-organ assessment. To overcome these limitations, I sought to develop a complementary whole-organ tomography imaging method. For this study, I specifically focused on contrast-enhanced computed tomography (CT) to enable *ex vivo* quantification of organ perfusion (Figure 4.1A).

I first sought to develop a simple quantitative metric that could be used to parameterize the quality of perfusion for robust statistical analysis. Porcine kidneys procured from a local slaughterhouse were infused with cold crystalloid and a bolus of iohexol contrast reagent. Three repeat axial scans were collected in quick succession to capture the initial dynamics of contrast filling in the organ (Figure 4.1B). From these 3D image stacks, the volume of contrast positive vasculature was calculated relative to the full volume of the organ measured during that scan. The fraction of contrast positive volume scaled roughly linearly in time, allowing a simple parameterization by fitting this trend to a line (Figure 4.1C).

The quantification of the initial dynamics of whole organ contrast filling provides a simple metric for comparison. However, this global metric does not provide regional information regarding the quality of microvascular perfusion in a given organ. To complement the volume fraction measurement, I added a fourth scan collected at 5 min after the initial bolus of iohexol was administered. This time point allows contrast to fully access microvascular regions and enter the parenchyma providing a clear qualitative discrimination of contrast accessible versus inaccessible microvascular regions. Representative axial and coronal scans from a pair of pig organs with or without one hour of autologous whole blood perfusion *ex vivo* to simulate reperfusion injury demonstrate the utility of this mode of visualization to assess regional variation in perfusion quality. For the delayed scan, Hounsfield units were measured pixel by pixel in the first 8 mm of the renal cortex as a metric to evaluate cortical

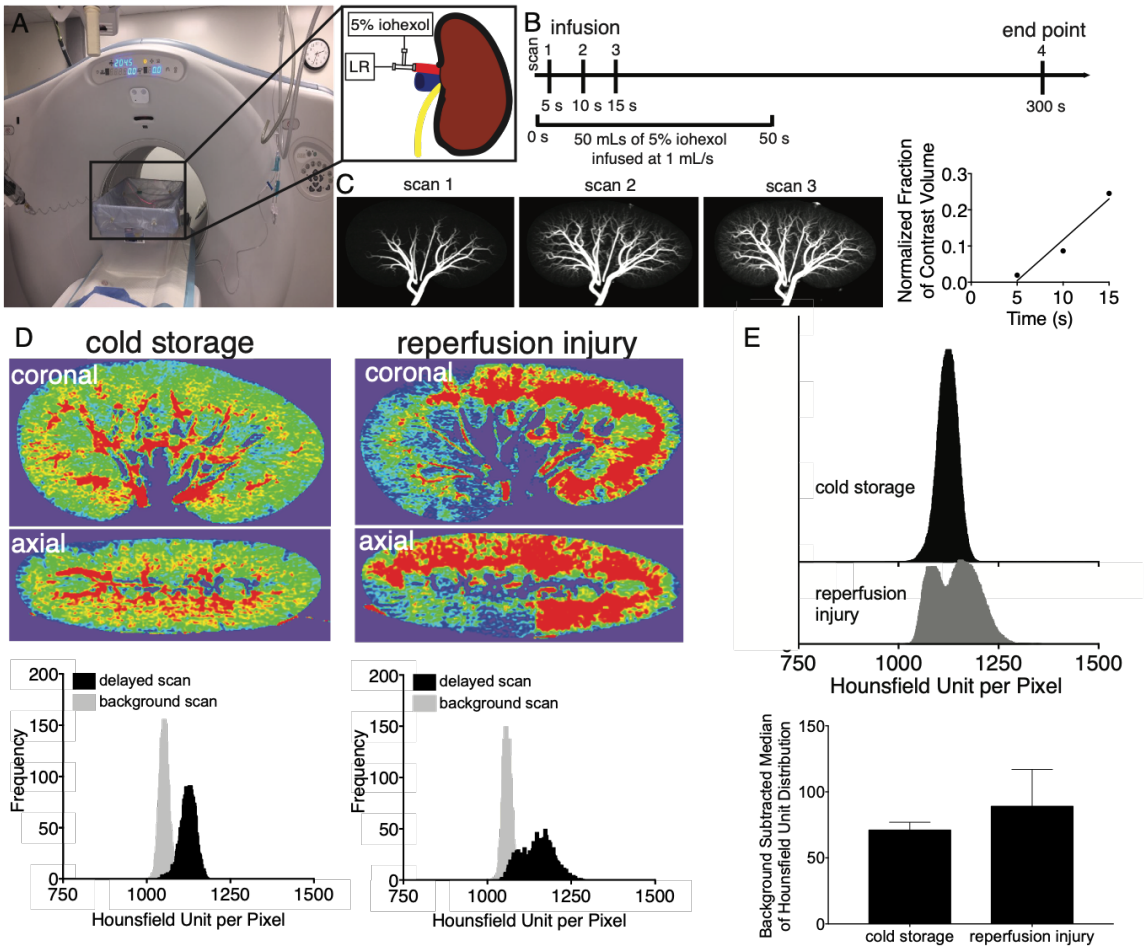

Fig. 4.1 **Schematic and methodology of CT imaging to assess renal vasculature *ex vivo*.** (A) *Ex vivo* porcine kidney is placed inside of a CT scanner for imaging. (B) Imaging sequence for kidneys during cold storage. (C) Maximum intensity projections are presented the first three sequential scan in the cold storage imaging series. (D) Heat maps are presented in axial and coronal views for a pair of porcine kidneys, with or without one hour of *ex vivo* whole blood perfusion to simulate a period of reperfusion. Distributions from single slices (left) and the full scans (right). (E) Background subtracted distributions and median values are presented for the scans in (D).

microvascular perfusion (Figure 4.1D). A histogram of the Hounsfield units was generated and a background subtracted median was used as a measure of the quality of microvascular perfusion (Figure 4.1E).

4.2 Angiography of transplant-declined human kidneys

Having optimized the imaging and assessment methods in porcine kidneys, I next imaged a series of 6 transplant-declined human kidneys under an identical protocol. The 6 human organs used for the study were recovered in coordination with the local organ procurement organization (New England Donor Services) under an existing research protocol. The organs were accepted in succession with no exclusion criteria on the basis of donor factors to provide an unbiased evaluation of the utility of these methods to distinguish differences in viability of transplant-declined human organs. Donor demographic details are provided in Table 4.1.

Table 4.1 **Donor demographics and organ characterization for transplant declined human kidneys.** Donor data and kidney characteristics obtained from national database of donors and information from organ offer. Acute Kidney Injury Network (AKIN) criteria – 0, 1, creatinine increases > 0.3 mg/dL (27 μM) or 150-200% above baseline; 2, creatinine increase 200-300% baseline, non-oliguric; 3, creatinine increase > 300% baseline or oliguria < 0.3 mL/hr.

Kidney ID	Donor type	Age	Sex	KDPI	Terminal creatinine	AKIN	Reason for decline
Cold storage imaging							
Kidney 1	DCD	22	M	32	0.8	1	air in cold perfusion pump
Kidney 2	DCD	39	M	71	0.9	0	biopsy
Kidney 3	DCD	39	M	71	0.9	0	biopsy
Kidney 4	DBD	57	F	94	4.7	3	high KDPI / AKI / biopsy
Kidney 5	DCD	57	M	88	1.4	3	high KDPI / long cold ischemic time
Kidney 6	DBD	60	M	91	4.9	3	high KDPI / AKI
NMP imaging							
Kidney 7	DBD	67	F	98	2.4	2	high KDPI / AKI
Kidney 8	DBD	41	M	39	0.8	2	papillary renal cell carcinoma
Kidney 9	DCD	59	M	94	0.8	0	surgical damage / high KDPI
Pre and post NMP imaging							
Kidney 10	DBD	58	F	75	2.3	2	AKI / long cold ischemic time
Kidney 11	DCD	46	M	44	0.74	1	biopsy / retroperitoneal fibrosis

Figure 4.2A depicts maximum intensity projections for the three consecutive scans of each human organ. There was substantial variation in the dynamics of contrast accessibility amongst the 6 organs (Figures 4.2A and B). The first organ in the series (Kidney 1) had the highest rate of contrast filling. Notably, this organ was from a 22-year-old DCD donor with a KDPI of 32 and had been accepted for transplantation. Unfortunately, an air pocket was noted in the cold-perfusion circuit prior to transplant and the organ was declined for fear of an air embolism in the kidney. The organ was otherwise healthy and viable for transplant. Air emboli within the kidney were not observed upon imaging and the maximum intensity projections appear to show good vascular access throughout the organ. Thus, this volumetric assessment likely represents a standard for organs with high quality global perfusion.

In contrast, Kidney 5 and Kidney 6 displayed poor rates of initial contrast filling suggesting substantial defects in the quality of global perfusion. Where the slope of contrast filling in Kidney 1 was $2.1\% \pm 0.1\%$ of the kidney volume filled per second, this slope dropped to $0.4\% \pm 0.04\%$ and $0.3\% \pm 0.2\%$ in Kidney 5 and Kidney 6 respectively. Thus, Kidney 5 and Kidney 6 likely represent the poorer end of the spectrum with respect to the quality of initial perfusion. These specific organs may not have been recoverable to a viable state for safe transplantation. However, the ability to quantify the state of global perfusion in a robust way can subsequently enable assessment of therapeutic strategies that would seek to restore the perfusion of kidneys like Kidney 5 and Kidney 6 to a state similar to Kidney 1 using repeat longitudinal measurements.

4.3 Regional microvascular accessibility assessment

Having evaluated the global metric of perfusion quality in the human organ series, the quality of microvascular perfusion as determined by the end point scan was then assessed. These images were segmented to remove all surrounding image artifact and pseudo-colored to depict regions of hypoperfusion (blue) relative to well perfused regions (red). Representative coronal and axial midpoint scans are displayed for qualitative visualization (Figure 4.3A).

In single slices throughout the scan, I was able to observe major differences in microvascular perfusion (Figure 4.3A). These images demonstrate that the kidneys with faster filling rates of the total vasculature have qualitatively more microvascular filling as evidenced by the clearly visible increased area of red in the renal cortex in Kidney 1 and Kidney 4. Alternatively, the kidneys with lower rates of initial filling, Kidney 5 and Kidney 6, have less or no contrast enhancement in the cortex as evidenced by the predominantly blue images. Importantly, Kidney 2, which had a higher initial filling rate, has relatively poor microvascular perfusion.

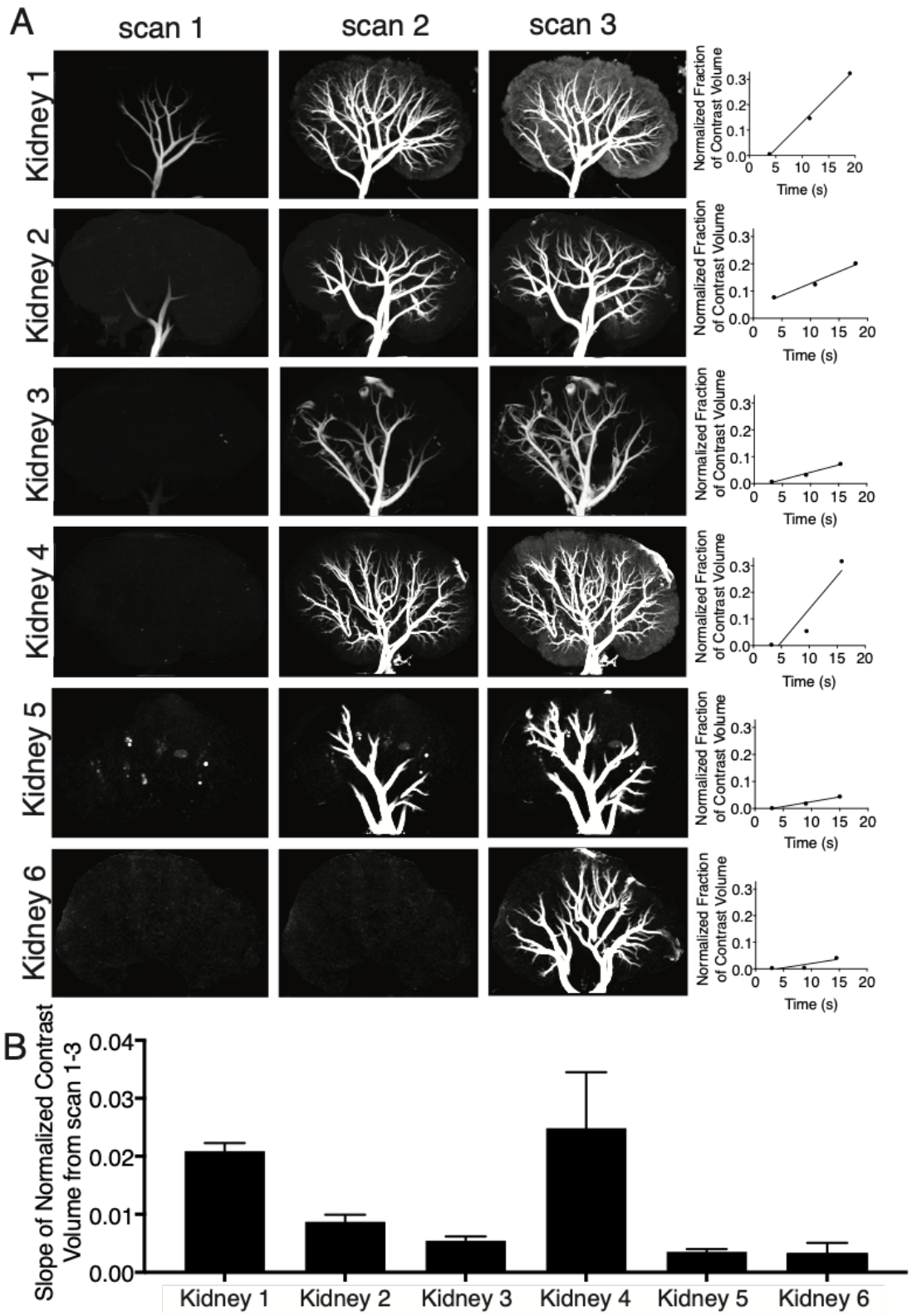

Fig. 4.2 **Angiography assessment of transplant-declined human kidneys.** (A) 6 human kidneys are presented as maximum intensity projections from each of the first 3 sequential scans. Vascular volumes are calculated and plotted for all four scans in the series. (B) Slopes from each vascular volume calculation are presented.

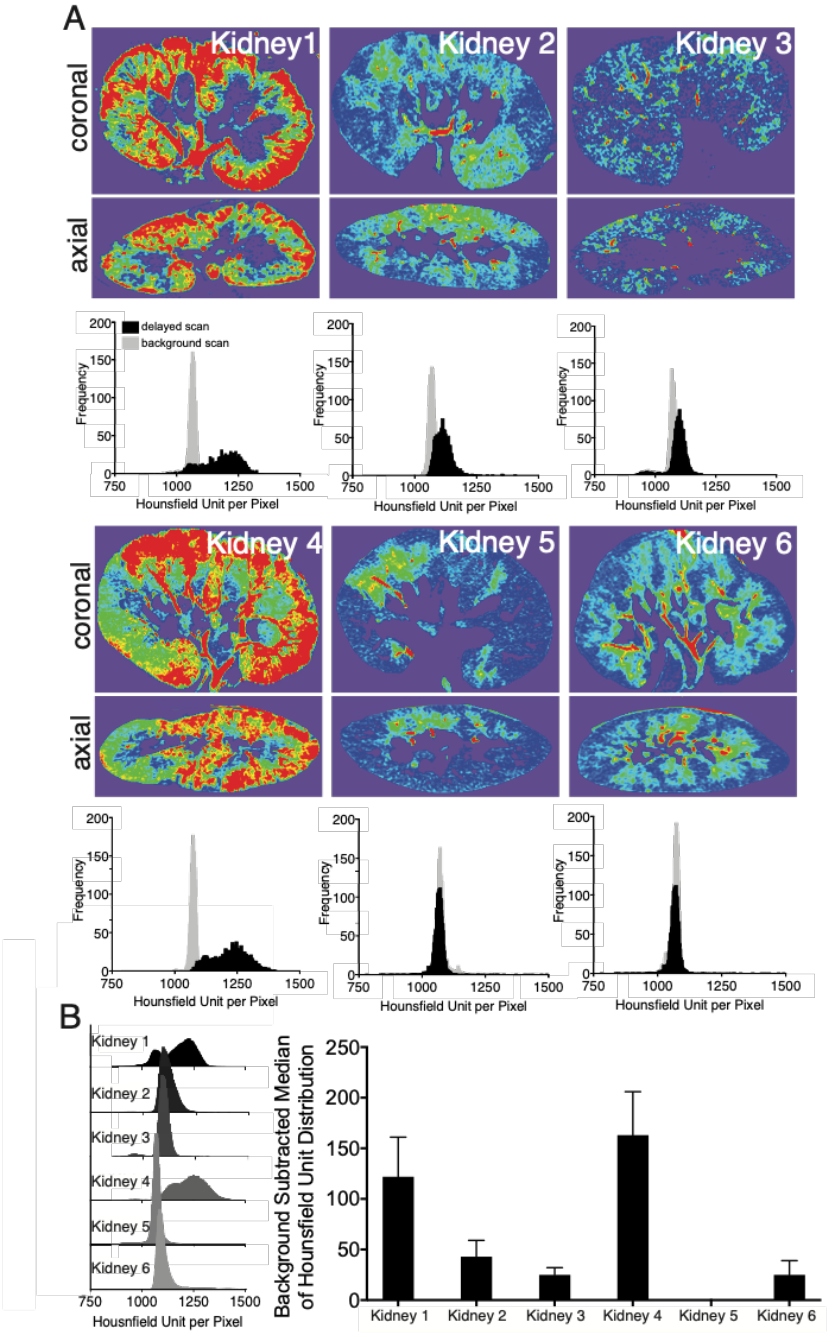

Fig. 4.3 **Assessment of regional microvascular accessibility in transplant-declined human organs.** (A) Heat map representations (top) and histograms of Hounsfield units in outer cortex (bottom) of single, midpoint axial and coronal slices from the end point scan of 6 human kidneys imaged with the cold storage imaging protocol are presented. Heat map ranges from blue representing the lower limit of enhancement to red, the upper limit of enhancement. (B) Histograms of Hounsfield units from pooled slices throughout the scan are presented for each kidney (left). Background subtracted medians are displayed (right).

This highlights that these assessments reflect different components of organ perfusion (i.e. global and regional perfusion quality).

Quantitative assessment of these images also supports what was qualitatively observed in the pseudocolored scans from the center of the organ (Figure 4.3A and B). Hounsfield units quantified per pixel in the first 8 mm of the cortex were measured in each slice of the full scan before and 5 minutes after contrast was administered. The shifts (or lack thereof) in the medians of the histograms from background reflect the quality of the cortical microvascular perfusion (Figure 4.3A and B). Again, it is observed that Kidney 1 and Kidney 4 have the highest levels of microvascular perfusion while Kidney 2, Kidney 3, Kidney 5, and Kidney 6 have little to no shift in Hounsfield units from the background measurement (Figure 4.3A and B).

4.4 Imaging during normothermic machine perfusion

The preceding data demonstrates the capacity of contrast-enhanced CT to provide a quantitative whole-organ assessment. I next sought to determine the utility of this approach for non-invasive, longitudinal evaluation of human kidneys during normothermic machine perfusion (NMP). A pilot series of three human kidneys (Kidney 7, Kidney 8, Kidney 9) was run to evaluate feasibility and determine the utility of contrast-enhanced CT in this setting. The standard NMP circuit was adapted for use with a clinical CT scanner to enable imaging during NMP [138]. With this approach, I was able to repeatedly obtain qualitative images of organ vasculature during NMP (Figure 4.4A).

This pilot series also identified a key limitation with respect to using iohexol as the CT contrast reagent for repeat longitudinal imaging during NMP. Specifically, a prolonged persistence of the iohexol contrast reagent was identified within the organ following each injection at different NMP time points. Evaluation of the four sequential scans performed at each NMP time point showed a relatively slow clearance of the contrast from the tissue after completion of iohexol injection. The 4th sequential organ scan, performed ~20 sec after iohexol has cleared from the renal vein, routinely showed significant retention of iohexol within the tissue parenchyma and all time points (Figure 4.4B and C). Moreover, a steady build in the parenchymal levels of iohexol was observed in the initial scan performed at each NMP time point (Figure 4.4D and E). This potential for continual buildup of iohexol contrast reagent during NMP suggests that this approach does not meet the second criteria for a non-invasive imaging modality to enable longitudinal measurements.

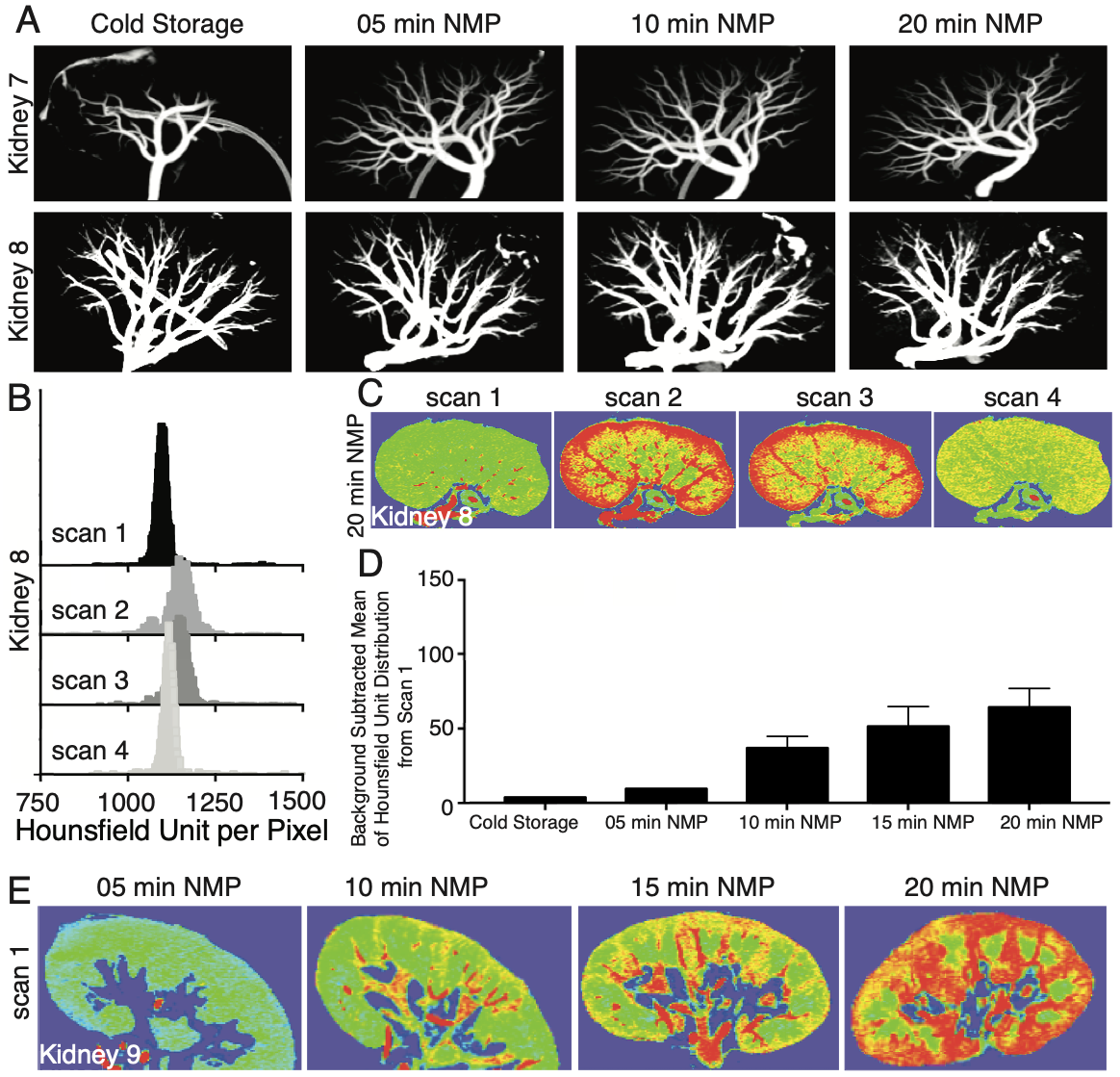

Fig. 4.4 **Contrast-enhanced CT imaging during NMP** (A) Representative maximum intensity projections of the large vessels from scan 2 are presented throughout 20 minutes of NMP from Kidney 7 and Kidney 8. (B) Histograms of microvascular intensities from the midpoint slice of Kidney 8 are presented from scans 1-4 at 20 minutes of NMP. (C) Heat maps for Kidney 8 are displayed for scans 1-4 corresponding to the histograms presented in (B). (D) Microvascular intensities from scan 1 are displayed throughout the 20 min of NMP for Kidney 9. (E) Heat maps for the midpoint slices of Kidney 9 are presented for the intensities presented in (D).

4.5 Imaging before and after normothermic machine perfusion

To circumvent the challenge of iohexol retention, I returned to the cold-storage imaging protocol to assess if iohexol could be effectively cleared with a flush of cold-lactated Ringers solution (LR) following imaging. Indeed, it was observed that a 1L flush of cold LR reliably removed iohexol to below the limits of detection (Figure 4.5). Thus, I next evaluated repeat cold-storage imaging before and after NMP as a means to assess changes in quantitative imaging parameters.

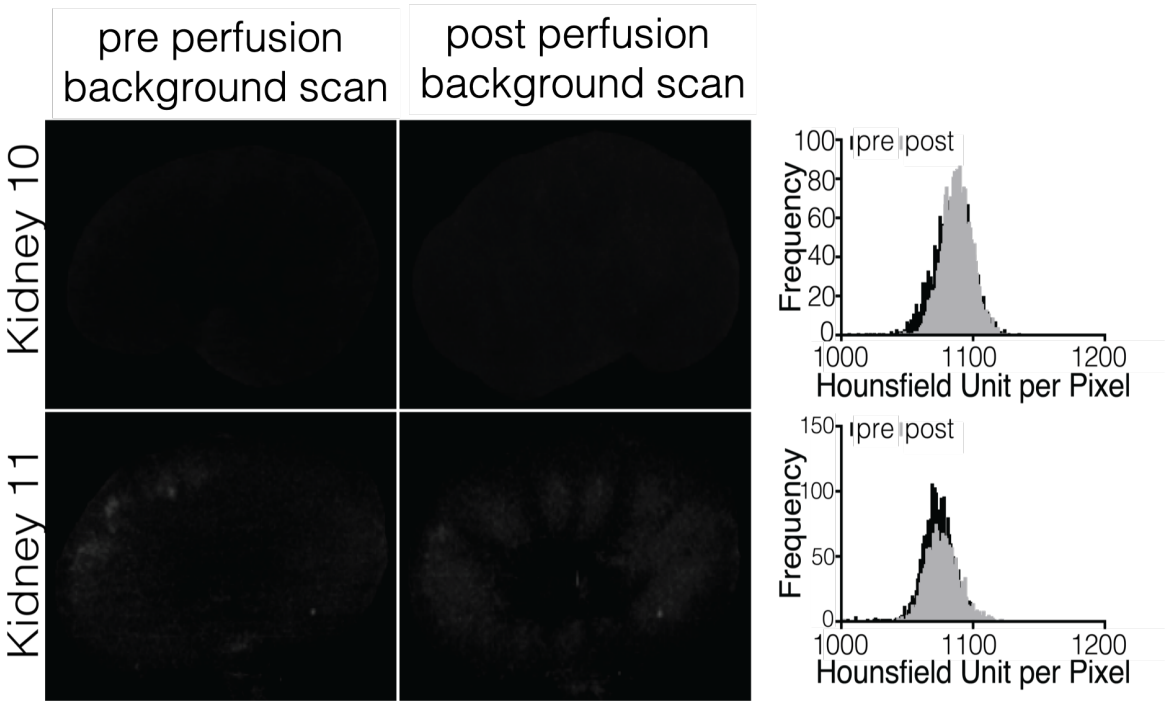

Fig. 4.5 **Complete flush of contrast under cold-storage imaging conditions.** Background scans and corresponding histograms from Kidney 10 and Kidney 11 are presented.

Prior to initiation of NMP, both human kidneys in this series (Kidney 10, Kidney 11) were each imaged with the standard cold-storage imaging protocol described above. Both organs achieved high levels of contrast filling comparable to that achieved by Kidney 1 in the preceding series (Figure 4.6A and B versus Figure 4.1A and B). Microvascular assessment, as in Figure 4.3, similarly showed high levels of contrast accessibility with generally good regional coverage; some relatively small pockets of hypoperfusion were observed similar to Kidney 1 (Figure 4.6C and D). Collectively, these metrics suggest these organs were in a relatively good state prior to NMP.

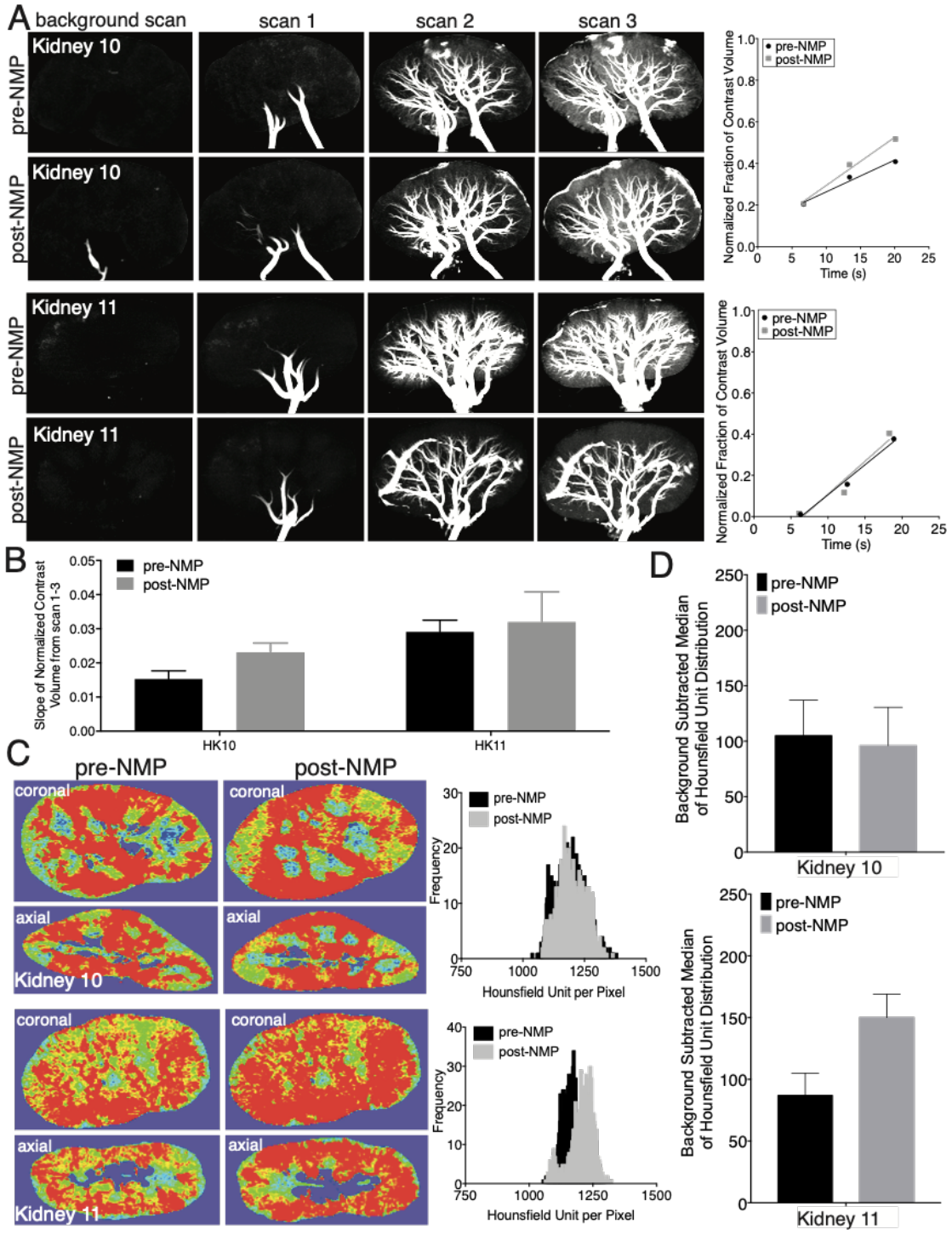

Fig. 4.6 **Contrast-enhanced CT before and after NMP.** (A) Maximum intensity projections are presented for Kidney 10 and Kidney 11 pre and post-NMP. The normalized fraction of contrast volume is displayed for each scan (right). (B) Slopes of the contrast volume calculated in (A) are presented pre and post-NMP for Kidney 10 and Kidney 11. Error is SD. (C) Heat maps for single slices from the midpoint of the organ are displayed along with their corresponding histograms. (D) Median values from the distribution of intensities within the cortex throughout the entire organ are displayed for Kidney 10 (top) and Kidney 11 (bottom).

Following the initial cold-storage imaging, the organs underwent 1 hr of NMP following the standard clinical protocol previously developed by Hosgood and Nicholson[26]. Both organs produced urine with Kidney 10 making 50 mL and Kidney 11 making 63 mL during the 1 hr perfusion period. In spite of making more urine, Kidney 11 had significantly impaired renal blood flow (RBF) relative to Kidney 10 (Figure 4.7). This combination of higher urine output with reduced RBF suggests a possible breakdown of glomerular barrier function.

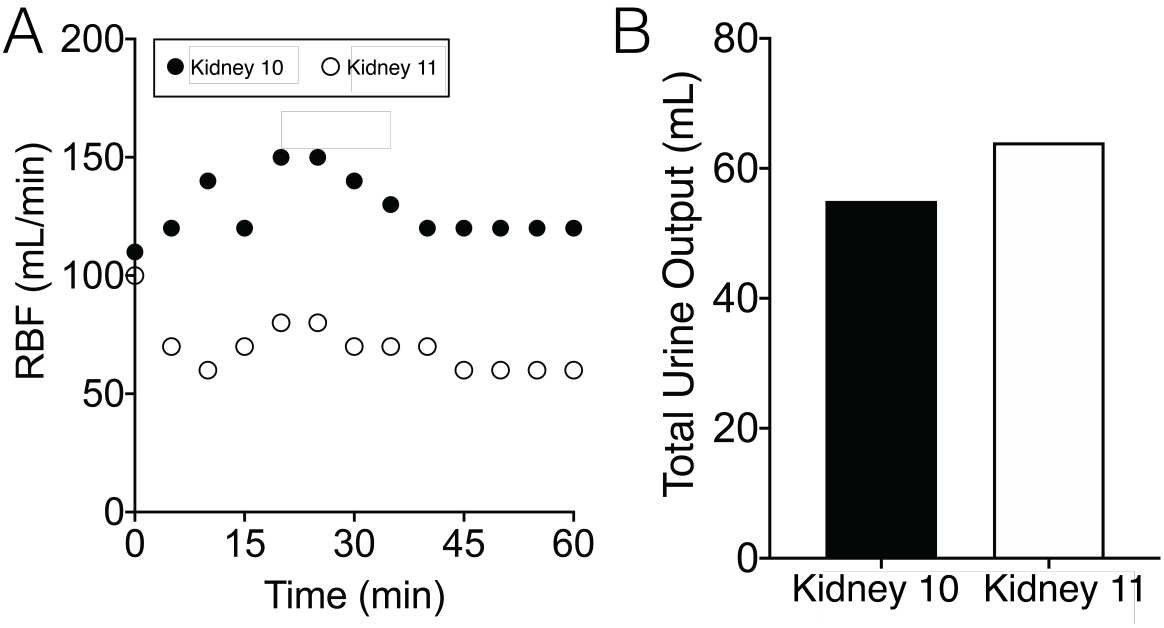

Fig. 4.7 **Organ perfusion parameters for Kidney 10 and Kidney 11.** (A) Renal blood flow (RBF) and urine output (B) are presented for Kidney 10 and Kidney 11.

Following NMP, both organs were again flushed with cold LR and cooled to 4°C under static-cold storage for repeat imaging under identical conditions as prior to NMP. In the repeat imaging series Kidney 10 had a slightly faster rate of contrast volume filling (2.4% $\pm$ 0.3% compared to 1.5% $\pm$ 0.2%), whereas Kidney 11 demonstrated no change. Notably, the median Hounsfield unit of the organ parenchyma was significantly higher in Kidney 11 after NMP as compared to NMP (Figure 4.6C and D). Additionally, vasoconstriction of the arterial vessels was also identified in Kidney 11 after NMP; vasoconstriction did not appear in Kidney 10. The combination of higher median Hounsfield unit and vasoconstriction following NMP was similar to that observed in a pig kidney perfused with whole blood (a model of ischemia reperfusion injury; Figure 4.1D).

Discussion

Ex vivo organ perfusion (including both hypothermic and normothermic variations) shows great promise as a platform to enable improved viability assessment of higher-risk organs [138–140]. As compared to a single biopsy collected from an organ under cold-storage, organs on *ex vivo* perfusion can be repeatedly assessed for physiologic function over time. At current, physiologic parameters like renal blood flow, vascular resistance, and urine production (under normothermic conditions) are routinely measured in clinical utilization of *ex vivo* perfusion [49, 26, 25, 128]. However, the utility of these basic parameters to guide good clinical decision making has yet to be established. In fact, evidence to date suggests that these parameters alone may not be reliable indicators of organ viability [119, 145]. Based on this, as well as my clinically focused research experience, I propose that these parameters may be necessary, but not sufficient, for effective organ evaluation. The underlying reason an organ produces a high level of urine, for example, could be because the organ is functioning well or because there has been a breakdown of glomerular barrier. Thus, there is a clear need for complementary diagnostics that can contextualize these functional parameters.

Previous groups, evaluating *ex vivo* imaging modalities, have primarily been limited to fluorescent imaging of animal organs [146, 147]. Here, I have evaluated the potential of *ex vivo* tomography imaging for use as one of these complementary diagnostic assessments. More specifically, contrast-enhanced CT was tested for two key criteria: (1) Capacity for regional assessment of circulation within the whole-organ; and (2) Capacity for non-invasive, longitudinal assessment in combination with NMP. The data demonstrate that contrast-enhanced CT can be used for quantitative assessment of regional circulation across the whole-organ (Criteria 1). I have further developed simple metrics to enable organ-to-organ comparisons using this modality. With respect to Criteria 2, I have shown that contrast-enhanced CT can potentially be used for longitudinal assessments in combination with NMP. However, there are also some restrictions necessary to limit the invasiveness of this procedure when using iohexol as the contrast reagent. Iohexol appeared to be retained in kidneys when repeatedly administered under normothermic perfusion conditions; the potential for nephrotoxicity of iohexol thus limits its use in this setting [148, 149]. However, I demonstrated that it is possible to circumvent the issue of iohexol retention by administration of iohexol under cold-storage conditions followed by extensive organ flushing.

It is beyond the scope of the current study to assess the safety and efficacy of *ex vivo* CT for clinical assessment of marginal organs. Nevertheless, this study suggests that such a future effort may be well worth considering. The example of Kidney 1, an otherwise completely transplantable organ that went unused due to a suspected air embolus, showcases

the potential. The 'cold-storage-imaging' approach developed here could possibly have been used to visually identify if the embolus had entered the organ vasculature and, if so, to further assess if extensive flushing could remove this. Additionally, the quantitative metrics could provide critical context to the current standard measures of physiology described above to enable clinicians to more effectively triage higher-risk organs. From a practical standpoint, it will be essential to develop the ability to maintain optimal organ temperature and sterility throughout the imaging procedure for this to become a clinically viable tool for assessment.

Contrast-enhanced CT imaging need not become a routine part of clinical care to still be a valuable research tool. The research potential of this approach is demonstrated by the vasoconstriction observed in both the pig kidney subjected to ischemia-reperfusion-injury and Kidney 11. First, this type of observation can guide the generation of hypotheses for future mechanistic studies to understand how organs respond to NMP. Moreover, if this severe vasoconstriction following NMP were to be definitively identified as a marker of organ injury, it could then be used to evaluate the efficacy of different therapeutic interventions administered during NMP. It should also be noted that there is no restriction to the sole use of iohexol as a contrast reagent or to CT as a sole imaging modality. There is a wide array of different contrast agents that could be explored in future studies, including agents that would remain within the vasculature to avoid the retention issue of iohexol. Additionally, nuclear imaging (e.g. PET for assessment of metabolic function or SPECT for multi-isotope molecular imaging of inflammatory markers) holds a great deal of promise in combination with CT imaging; the scanner used for this study features both modalities.

Chapter 5

Summary

5.1 Revisiting Aims

In this section, I explore how the initial aims I set out to achieve throughout this body of work were met.

1. Effectively deliver targeted nanoparticles during *ex vivo* NMP

In Chapter 1, I had demonstrated that it was possible to target nanoparticles to the vascular endothelium during NMP. In well perfused organs, there was a significant targeting benefit. In poorly perfused organs, NPs accumulated nonspecifically in red cell plugs. After developing a regimen to re-establish microvascular perfusion, endothelial targeted NPs showed a significant targeting benefit even in long-cold stored organs. However, even in treated cases, targeted NPs do not cover all of the microvasculature. This suggests that in future work, we may need to consider changing the administered dose and/or modifying the targeting capacity of the NPs.

2. Re-establish microvascular circulation in poorly perfused organs

Using a treatment regimen of tPA and plasminogen, I was able to effectively lyse microvascular obstructions in human kidneys during NMP and re-establish microvascular circulation. Not only did this enable better targeted drug delivery, it also lowered markers of tissue injury, increased urine output, and stabilized kidney resistances.

3. Understand mechanisms by which microvascular obstructions arise

In this body of work I discovered that microvascular obstructions are rich in fibrinogen. Upon the restoration of normothermia, sequestered fibrinogen in the tubular epithelia (that is cold

storage dependent) is released into the vasculature and correlates with the appearance of microvascular obstructions. While there may be other factors that contribute to the rise of these microvascular obstructions, the translocation of fibrinogen into the vasculature appears to be key mediator in poor organ perfusion seen in long-cold stored organs.

4. Investigate potential pre-transplantation therapeutic strategies to prevent IRI

Throughout the course of this thesis, I was able to investigate the role of an NLRP3 inflammasome inhibitor (MCC050) in IRI. I found that when delivered to human kidneys during NMP, MCC950 had a protective effect up to 8 hours after the treatment was initially administered. While there are many other therapeutic strategies available to investigate, MCC950 shows significant promise.

5. Develop non-invasive imaging methods to visualize perfusion quality of whole organs

In most organ-based research, whole organ assessments are made based either on macroscopic appearance or biopsy results. Here, I was able to successfully develop a high resolution (600 μm), *ex vivo* imaging protocol utilizing CT to visualize vasculature integrity during cold storage and NMP. Ultimately, this methodology can be adapted to utilize other contrast agents or imaging platforms (e.g. positron emission tomography). As this approach is highly customizable, I believe this advancement can be a valuable tool for organ research.

5.2 Future Directions

Having defined the conditions for effective NP targeting in an *ex vivo* setting and showing that MCC950 is protective against IRI in the short term, the next logical step is to begin formulating NPs with the small hydrophobic drug. To do so, it will be necessary to determine the conditions (e.g organic:aqueous ratio, drug loading percentage, nanoprecipitation flow rate) for optimal sustained release profiles of the NPs. Additionally, it will be necessary to characterize the size, polydispersity index, and drug encapsulation efficiency of these particles before tests can begin during renal NMP. It will be possible to utilize the *ex vivo* imaging modalities developed throughout this thesis to ensure quality of perfusion and desired protection from IRI in whole blood perfusion models.

The discovery that the accumulation of fibrinogen within the renal tubular epithelium increases with cold storage time has led to more questions about “why organs fail” during cold storage. Previously stored samples from our fibrinogen time course studies are currently

being processed using multi-omic approaches (i.e. RNA sequencing and proteomics) to help answer these questions. Through developing a more comprehensive understanding of how organs respond to periods of cold stress, it should be possible to design better pre-transplant therapeutics as I did with the tPA and plasminogen treatment regimen.

More immediately, I am working to establish a pilot trial of tPA and plasminogen treatment in marginal kidneys with extended periods of cold preservation. In collaboration with Prof. Nicholson, Dr. Hosgood, Dr. Tietjen, New England Donor Services, and the Yale Department of Surgery, we plan to use this pilot trial in a series of 20 patients to determine the safety and preliminary efficacy of transplanting tPA and plasminogen treated kidneys. Based on the findings from my doctoral work, we believe that the successful implementation of this treatment regimen will ultimately increase the rates of long-cold stored organ utilization in renal transplantation and may further improve long-term viability of these organs. This clinical trial will be the focus of my first year as a postdoctoral researcher at Yale, prior to my enrollment in medical school as I pursue a career as an academic transplant surgeon.

References

[1] WHO-ONT. Global observatory on donation and transplantation. 2017.

[2] UNOS. United network for organ sharing, 2020.

[3] C. Ponticelli. Ischaemia-reperfusion injury: a major protagonist in kidney transplantation. *Nephrol Dial Transplant*, 29(6):1134–40, 2014.

[4] D. E. Stewart, V. C. Garcia, J. D. Rosendale, D. K. Klassen, and B. J. Carrico. Diagnosing the decades-long rise in the deceased donor kidney discard rate in the united states. *Transplantation*, 101(3):575–587, 2017.

[5] H. Zhao, A. Alam, A. P. Soo, A. J. T. George, and D. Ma. Ischemia-reperfusion injury reduces long term renal graft survival: Mechanism and beyond. *EBioMedicine*, 28:31–42, 2018.

[6] M. Kosieradzki and W. Rowinski. Ischemia/reperfusion injury in kidney transplantation: mechanisms and prevention. *Transplant Proc*, 40(10):3279–88, 2008.

[7] J. Cui, L. Qin, J. Zhang, P. Abrahimi, H. Li, G. Li, G. T. Tietjen, G. Tellides, J. S. Pober, and W. Mark Saltzman. Ex vivo pretreatment of human vessels with sirna nanoparticles provides protein silencing in endothelial cells. *Nat Commun*, 8(1):191, 2017.

[8] F. K. Port, R. M. Merion, E. C. Roys, and R. A. Wolfe. Trends in organ donation and transplantation in the united states, 1997-2006. *Am J Transplant*, 8(4 Pt 2):911–21, 2008.

[9] M. Hassanain, E. Simoneau, S. A. Doi, M. Aljiffry, A. Aloraini, A. Madkhali, and P. Metrakos. Trends in brain-dead organ donor characteristics: a 13-year analysis. *Can J Surg*, 59(3):154–60, 2016.

[10] H. Le Dinh, J. Monard, M. H. Delbouille, M. F. Hans, L. Weekers, C. Bonvoisin, J. Joris, S. Lauwick, A. Kaba, D. Ledoux, A. de Roover, P. Honore, J. P. Squifflet, M. Meurisse, and O. Detry. A more than 20transplantation activity after the use of donation after circulatory death. *Transplant Proc*, 46(1):9–13, 2014.

[11] M. Malek and M. Nematbakhsh. Renal ischemia/reperfusion injury; from pathophysiology to treatment. *J Renal Inj Prev*, 4(2):20–7, 2015.

[12] N. Le Clef, A. Verhulst, P. C. D'Haese, and B. A. Vervaet. Unilateral renal ischemia-reperfusion as a robust model for acute to chronic kidney injury in mice. *Plos One*, 11(3), 2016.

[13] D. P. Basile, M. D. Anderson, and T. A. Sutton. Pathophysiology of acute kidney injury. *Compr Physiol*, 2(2):1303–53, 2012.

[14] T. Kalogeris, C. P. Baines, M. Krenz, and R. J. Korthuis. Cell biology of ischemia/reperfusion injury. *Int Rev Cell Mol Biol*, 298:229–317, 2012.

[15] A. Kezic, N. Stajic, and F. Thaiss. Innate immune response in kidney ischemia/reperfusion injury: Potential target for therapy. *J Immunol Res*, 2017:6305439, 2017.

[16] Z. Guo, S. Yu, X. Chen, R. Ye, W. Zhu, and X. Liu. Nlrp3 is involved in ischemia/reperfusion injury. *CNS Neurol Disord Drug Targets*, 15(6):699–712, 2016.

[17] A. Vilaysane, J. Chun, M. E. Seamone, W. Wang, R. Chin, S. Hirota, Y. Li, S. A. Clark, J. Tschopp, K. Trpkov, B. R. Hemmelgarn, P. L. Beck, and D. A. Muruve. The nlrp3 inflammasome promotes renal inflammation and contributes to ckd. *J Am Soc Nephrol*, 21(10):1732–44, 2010.

[18] J. C. Leemans, S. L. Cassel, and F. S. Sutterwala. Sensing damage by the nlrp3 inflammasome. *Immunol Rev*, 243(1):152–62, 2011.

[19] P. Hong, F. X. Li, R. N. Gu, Y. Y. Fang, L. Y. Lai, Y. W. Wang, T. Tao, S. Y. Xu, Z. J. You, and H. F. Zhang. Inhibition of nlrp3 inflammasome ameliorates cerebral ischemia-reperfusion injury in diabetic mice. *Neural Plast*, 2018:9163521, 2018.

[20] K. Y. Xu, C. Y. Wu, S. Tong, P. Xiong, and S. H. Wang. The selective nlrp3 inflammasome inhibitor mcc950 attenuates lung ischemia-reperfusion injury. *Biochem Biophys Res Commun*, 503(4):3031–3037, 2018.

[21] D. A. Hume. The mononuclear phagocyte system. *Curr Opin Immunol*, 18(1):49–53, 2006.

[22] 3rd Bidwell, G. L., F. Mahdi, Q. Shao, O. C. Logue, J. P. Waller, C. Reese, and A. R. Chade. A kidney-selective biopolymer for targeted drug delivery. *Am J Physiol Renal Physiol*, 312(1):F54–F64, 2017.

[23] L. E. Deelman, A. E. Decleves, J. J. Rychak, and K. Sharma. Targeted renal therapies through microbubbles and ultrasound. *Advanced Drug Delivery Reviews*, 62(14):1369–1377, 2010.

[24] S. A. Hosgood, M. Patel, and M. L. Nicholson. The conditioning effect of ex vivo normothermic perfusion in an experimental kidney model. *J Surg Res*, 182(1):153–60, 2013.

[25] S. A. Hosgood, E. van Heurn, and M. L. Nicholson. Normothermic machine perfusion of the kidney: better conditioning and repair? *Transpl Int*, 28(6):657–64, 2015.

[26] S. A. Hosgood, K. Saeb-Parsy, C. Wilson, C. Callaghan, D. Collett, and M. L. Nicholson. Protocol of a randomised controlled, open-label trial of ex vivo normothermic perfusion versus static cold storage in donation after circulatory death renal transplantation. *BMJ Open*, 7(1):e012237, 2017.

[27] J. M. Kaths, M. Hamar, J. Echeverri, I. Linares, P. Urbanellis, J. Y. Cen, S. Ganesh, L. S. Dingwell, P. Yip, R. John, D. Bagli, I. Mucsi, A. Ghanekar, D. Grant, L. A. Robinson, and M. Selzner. Normothermic ex vivo kidney perfusion for graft quality assessment prior to transplantation. *Am J Transplant*, 2017.

[28] L. Brasile, R. Buelow, B. M. Stubenitsky, and G. Kootstra. Induction of heme oxygenase-1 in kidneys during ex vivo warm perfusion. *Transplantation*, 76(8):1145–9, 2003.

[29] G. T. Tietjen, L. G. Bracaglia, W. M. Saltzman, and J. S. Pober. Focus on fundamentals: Achieving effective nanoparticle targeting. *Trends Mol Med*, 24(7):598–606, 2018.

[30] A. Bagul, S. A. Hosgood, M. Kaushik, and M. L. Nicholson. Carbon monoxide protects against ischemia-reperfusion injury in an experimental model of controlled nonheartbeating donor kidney. *Transplantation*, 85(4):576–81, 2008.

[31] S. A. Hosgood, A. Bagul, M. Kaushik, J. Rimoldi, R. S. Gadepalli, and M. L. Nicholson. Application of nitric oxide and carbon monoxide in a model of renal preservation. *Br J Surg*, 95(8):1060–7, 2008.

[32] J. C. Yeung, D. Wagnetz, M. Cypel, M. Rubacha, T. Koike, Y. M. Chun, J. Hu, T. K. Waddell, D. M. Hwang, M. Liu, and S. Keshavjee. Ex vivo adenoviral vector gene delivery results in decreased vector-associated inflammation pre- and post-lung transplantation in the pig. *Mol Ther*, 20(6):1204–11, 2012.

[33] M. M. Aburawi, F. M. Fontan, N. Karimian, C. Eymard, S. Cronin, C. Pendexter, S. Nagpal, P. Banik, S. Ozer, P. Mahboub, F. L. Delmonico, H. Yeh, K. Uygun, and J. F. Markmann. Synthetic hemoglobin-based oxygen carriers are an acceptable alternative for packed red blood cells in normothermic kidney perfusion. *Am J Transplant*, 19(10):2814–2824, 2019.

[34] T. D. Adams, S. A. Hosgood, and M. L. Nicholson. Physiological effects of altering oxygenation during kidney normothermic machine perfusion. *Am J Physiol Renal Physiol*, 316(5):F823–F829, 2019.

[35] J. P. Hunter, S. A. Hosgood, M. Patel, R. Rose, K. Read, and M. L. Nicholson. Effects of hydrogen sulphide in an experimental model of renal ischaemia-reperfusion injury. *Br J Surg*, 99(12):1665–71, 2012.

[36] J. M. Sierra-Parraga, M. Eijken, J. Hunter, C. Moers, H. Leuvenink, B. Moller, R. J. Ploeg, C. C. Baan, B. Jespersen, and M. J. Hoogduijn. Mesenchymal stromal cells as anti-inflammatory and regenerative mediators for donor kidneys during normothermic machine perfusion. *Stem Cells and Development*, 26(16):1162–1170, 2017.

[37] L. Brasile, N. Henry, G. Orlando, and B. Stubenitsky. Potentiating renal regeneration using mesenchymal stem cells. *Transplantation*, 103(2):307–313, 2019.

[38] L. Brasile, B. M. Stubenitsky, M. H. Booster, D. Arenada, C. Haisch, and G. Kootstra. Transfection and transgene expression in a human kidney during ex vivo warm perfusion. *Transplant Proc*, 34(7):2624, 2002.

[39] C. J. Cheng, G. T. Tietjen, J. K. Saucier-Sawyer, and W. M. Saltzman. A holistic approach to targeting disease with polymeric nanoparticles. *Nat Rev Drug Discov*, 14(4):239–47, 2015.

[40] J. A. Hubbell and R. Langer. Translating materials design to the clinic. *Nat Mater*, 12(11):963–6, 2013.

[41] J. E. Zuckerman, I. Gritli, A. Tolcher, J. D. Heidel, D. Lim, R. Morgan, B. Chmielowski, A. Ribas, M. E. Davis, and Y. Yen. Correlating animal and human phase ia/ib clinical data with calaa-01, a targeted, polymer-based nanoparticle containing sirna. *Proc Natl Acad Sci U S A*, 111(31):11449–54, 2014.

[42] A. Z. Wang, R. Langer, and O. C. Farokhzad. Nanoparticle delivery of cancer drugs. *Annu Rev Med*, 63:185–98, 2012.

[43] F. Alexis, E. Pridgen, L. K. Molnar, and O. C. Farokhzad. Factors affecting the clearance and biodistribution of polymeric nanoparticles. *Mol Pharm*, 5(4):505–15, 2008.

[44] R. Gaspar. Nanoparticles: Pushed off target with proteins. *Nat Nanotechnol*, 8(2):79–80, 2013.

[45] Z. Amoozgar and Y. Yeo. Recent advances in stealth coating of nanoparticle drug delivery systems. *Wiley Interdiscip Rev Nanomed Nanobiotechnol*, 4(2):219–33, 2012.

[46] D. Xu, C. J. Tsai, and R. Nussinov. Hydrogen bonds and salt bridges across protein-protein interfaces. *Protein Eng*, 10(9):999–1012, 1997.

[47] D. D. Von Hoff, M. M. Mita, R. K. Ramanathan, G. J. Weiss, A. C. Mita, P. M. LoRusso, 3rd Burris, H. A., L. L. Hart, S. C. Low, D. M. Parsons, S. E. Zale, J. M. Summa, H. Youssoufian, and J. C. Sachdev. Phase i study of psma-targeted docetaxel-containing nanoparticle bind-014 in patients with advanced solid tumors. *Clin Cancer Res*, 22(13):3157–63, 2016.

[48] Vladimir R. Muzykantov. Targeted drug delivery to endothelial adhesion molecules. *ISRN Vascular Medicine*, 2013:1–27, 2013.

[49] S. A. Hosgood and M. L. Nicholson. An assessment of urinary biomarkers in a series of declined human kidneys measured during ex vivo normothermic kidney perfusion. *Transplantation*, 101(9):2120–2125, 2017.

[50] B. Sis, G. S. Jhangri, S. Bunnag, K. Allanach, B. Kaplan, and P. F. Halloran. Endothelial gene expression in kidney transplants with alloantibody indicates antibody-mediated damage despite lack of c4d staining. *Am J Transplant*, 9(10):2312–23, 2009.

[51] H. Bian and E. F. Reed. Alloantibody-mediated class i signal transduction in endothelial cells and smooth muscle cells: enhancement by ifn-gamma and tnf-alpha. *J Immunol*, 163(2):1010–8, 1999.

[52] D. Brandle, J. Joergensen, G. Zenke, K. Burki, and R. P. Hof. Contribution of donor-specific antibodies to acute allograft rejection: evidence from b cell-deficient mice. *Transplantation*, 65(11):1489–93, 1998.

[53] A. S. Chong and M. L. Alegre. The impact of infection and tissue damage in solid-organ transplantation. *Nat Rev Immunol*, 12(6):459–71, 2012.

[54] G. Castellano, R. Melchiorre, A. Loverre, P. Ditonno, V. Montinaro, M. Rossini, C. Divella, M. Battaglia, G. Lucarelli, G. Annunziata, S. Palazzo, F. P. Selvaggi, F. Staffieri, A. Crovace, M. R. Daha, M. Mannesse, S. van Wetering, F. Paolo Schena, and G. Grandaliano. Therapeutic targeting of classical and lectin pathways of complement protects from ischemia-reperfusion-induced renal damage. *Am J Pathol*, 176(4):1648–59, 2010.

[55] A. Barbari, S. Abbas, and M. Jaafar. Approach to kidney transplant in sensitized potential transplant recipients. *Exp Clin Transplant*, 10(5):419–27, 2012.

[56] J. Devalliere, W. G. Chang, J. W. Andrejecsk, P. Abrahimi, C. J. Cheng, D. Jane-wit, W. M. Saltzman, and J. S. Pober. Sustained delivery of proangiogenic microrna-132 by nanoparticle transfection improves endothelial cell transplantation. *FASEB J*, 28(2):908–22, 2014.

[57] Z. Cheng, A. Al Zaki, J. Z. Hui, V. R. Muzykantov, and A. Tsourkas. Multifunctional nanoparticles: cost versus benefit of adding targeting and imaging capabilities. *Science*, 338(6109):903–10, 2012.

[58] C. H. Choi, C. A. Alabi, P. Webster, and M. E. Davis. Mechanism of active targeting in solid tumors with transferrin-containing gold nanoparticles. *Proc Natl Acad Sci U S A*, 107(3):1235–40, 2010.

[59] E. Blanco, H. Shen, and M. Ferrari. Principles of nanoparticle design for overcoming biological barriers to drug delivery. *Nat Biotechnol*, 33(9):941–51, 2015.

[60] S. Tenzer, D. Docter, J. Kuharev, A. Musyanovych, V. Fetz, R. Hecht, F. Schlenk, D. Fischer, K. Kiouptsi, C. Reinhardt, K. Landfester, H. Schild, M. Maskos, S. K. Knauer, and R. H. Stauber. Rapid formation of plasma protein corona critically affects nanoparticle pathophysiology. *Nat Nanotechnol*, 8(10):772–81, 2013.

[61] M. Lundqvist, J. Stigler, G. Elia, I. Lynch, T. Cedervall, and K. A. Dawson. Nanoparticle size and surface properties determine the protein corona with possible implications for biological impacts. *Proc Natl Acad Sci U S A*, 105(38):14265–70, 2008.

[62] M. P. Monopoli, C. Aberg, A. Salvati, and K. A. Dawson. Biomolecular coronas provide the biological identity of nanosized materials. *Nat Nanotechnol*, 7(12):779–86, 2012.

[63] M. P. Pusztaszeri, W. Seelentag, and F. T. Bosman. Immunohistochemical expression of endothelial markers cd31, cd34, von willebrand factor, and fli-1 in normal human tissues. *J Histochem Cytochem*, 54(4):385–95, 2006.

[64] C. Garnacho, S. M. Albelda, V. R. Muzykantov, and S. Muro. Differential intra-endothelial delivery of polymer nanocarriers targeted to distinct pecam-1 epitopes. *J Control Release*, 130(3):226–33, 2008.

[65] J. Han, V. V. Shuvaev, P. F. Davies, D. M. Eckmann, S. Muro, and V. R. Muzykantov. Flow shear stress differentially regulates endothelial uptake of nanocarriers targeted to distinct epitopes of pecam-1. *J Control Release*, 210:39–47, 2015.

[66] J. Han, B. J. Zern, V. V. Shuvaev, P. F. Davies, S. Muro, and V. Muzykantov. Acute and chronic shear stress differently regulate endothelial internalization of nanocarriers targeted to platelet-endothelial cell adhesion molecule-1. *ACS Nano*, 6(10):8824–36, 2012.

[67] J. Hrkach, D. Von Hoff, M. Mukkaram Ali, E. Andrianova, J. Auer, T. Campbell, D. De Witt, M. Figa, M. Figueiredo, A. Horhota, S. Low, K. McDonnell, E. Peeke, B. Retnarajan, A. Sabnis, E. Schnipper, J. J. Song, Y. H. Song, J. Summa, D. Tompsett, G. Troiano, T. Van Geen Hoven, J. Wright, P. LoRusso, P. W. Kantoff, N. H. Bander, C. Sweeney, O. C. Farokhzad, R. Langer, and S. Zale. Preclinical development and clinical translation of a psma-targeted docetaxel nanoparticle with a differentiated pharmacological profile. *Sci Transl Med*, 4(128):128ra39, 2012.

[68] G. T. Hermanson. *Bioconjugate Techniques*. Academic Press, 3 edition, 2013.

[69] C. Tassa, J. L. Duffner, T. A. Lewis, R. Weissleder, S. L. Schreiber, A. N. Koehler, and S. Y. Shaw. Binding affinity and kinetic analysis of targeted small molecule-modified nanoparticles. *Bioconjug Chem*, 21(1):14–9, 2010.

[70] T. D. Dziubla, V. V. Shuvaev, N. K. Hong, B. J. Hawkins, M. Madesh, H. Takano, E. Simone, M. T. Nakada, A. Fisher, S. M. Albelda, and V. R. Muzykantov. Endothelial targeting of semi-permeable polymer nanocarriers for enzyme therapies. *Biomaterials*, 29(2):215–27, 2008.

[71] N. Bertrand, J. Wu, X. Xu, N. Kamaly, and O. C. Farokhzad. Cancer nanotechnology: the impact of passive and active targeting in the era of modern cancer biology. *Adv Drug Deliv Rev*, 66:2–25, 2014.

[72] M. Zhao and M. Liu. New avenues for nanoparticle-related therapies. *Nanoscale Res Lett*, 13(1):136, 2018.

[73] D. Nakajima, M. Cypel, R. Bonato, T. N. Machuca, I. Iskender, K. Hashimoto, V. Linacre, M. Chen, R. Coutinho, S. Azad, T. Martinu, T. K. Waddell, D. M. Hwang, S. Husain, M. Liu, and S. Keshavjee. Ex vivo perfusion treatment of infection in human donor lungs. *Am J Transplant*, 16(4):1229–37, 2016.

[74] G. T. Tietjen, S. A. Hosgood, J. DiRito, J. Cui, D. Deep, E. Song, J. R. Kraehling, A. S. Piotrowski-Daspit, N. C. Kirkiles-Smith, R. Al-Lamki, S. Thiru, J. A. Bradley, K. Saeb-Parsy, J. R. Bradley, M. L. Nicholson, W. M. Saltzman, and J. S. Pober. Nanoparticle targeting to the endothelium during normothermic machine perfusion of human kidneys. *Sci Transl Med*, 9(418), 2017.

[75] A. M. Chacko, J. Han, C. F. Greineder, B. J. Zern, J. L. Mikitsh, M. Nayak, D. Menon, I. H. Johnston, M. Poncz, D. M. Eckmann, P. F. Davies, and V. R. Muzykantov. Collaborative enhancement of endothelial targeting of nanocarriers by modulating platelet-endothelial cell adhesion molecule-1/cd31 epitope engagement. *ACS Nano*, 9(7):6785–93, 2015.

[76] D. Lominadze. Involvement of fibrinogen specific binding in erythrocyte aggregation. *FEBS Lett*, 517(41):1–3, 2002.

[77] M. Brust, O. Aouane, M. Thiebaud, D. Flormann, C. Verdier, L. Kaestner, M. W. Laschke, H. Selmi, A. Benyoussef, T. Podgorski, G. Coupier, C. Misbah, and C. Wagner. The plasma protein fibrinogen stabilizes clusters of red blood cells in microcapillary flows. *Sci Rep*, 4:4348, 2014.

[78] José V. Castell, Maria J. Gómez-Lechón, Martina David, Tilo Andus, Thomas Geiger, Ramón Trullenque, Ricardo Fabra, and Peter C. Heinrich. Interleukin-6 is the major regulator of acute phase protein synthesis in adult human hepatocytes. *FEBS Letters*, 242(2):237–239, 1989.

[79] P. J. Hamilton, A. L. Stalker, and A. S. Douglas. Disseminated intravascular coagulation: a review. *J Clin Pathol*, 31(7):609–19, 1978.

[80] A. C. Lendrum, D. S. Fraser, W. Slidders, and R. Henderson. Studies on the character and staining of fibrin. *J Clin Pathol*, 15:401–13, 1962.

[81] Jr. Wells, R. E., T. H. Gawronski, P. J. Cox, and R. D. Perera. Influence of fibrinogen on flow properties of erythrocyte suspensions. *Am J Physiol*, 207:1035–40, 1964.

[82] E. H. Stoops and M. J. Caplan. Trafficking to the apical and basolateral membranes in polarized epithelial cells. *J Am Soc Nephrol*, 25(7):1375–86, 2014.

[83] H. Kalra, G. P. Drummen, and S. Mathivanan. Focus on extracellular vesicles: Introducing the next small big thing. *Int J Mol Sci*, 17(2):170, 2016.

[84] I. Sorensen-Zender, S. Rong, N. Susnik, J. Lange, F. Gueler, J. L. Degen, A. Melk, H. Haller, and R. Schmitt. Role of fibrinogen in acute ischemic kidney injury. *Am J Physiol Renal Physiol*, 305(5):F777–85, 2013.

[85] I. Sorensen, N. Susnik, T. Inhester, J. L. Degen, A. Melk, H. Haller, and R. Schmitt. Fibrinogen, acting as a mitogen for tubulointerstitial fibroblasts, promotes renal fibrosis. *Kidney Int*, 80(10):1035–44, 2011.

[86] A. K. Ajay, J. Saikumar, V. Bijol, and V. S. Vaidya. Heterozygosity for fibrinogen results in efficient resolution of kidney ischemia reperfusion injury. *PLoS One*, 7(9):e45628, 2012.

[87] D. Hoffmann, V. Bijol, A. Krishnamoorthy, V. R. Gonzalez, G. Frendl, Q. Zhang, P. L. Goering, R. P. Brown, S. S. Waikar, and V. S. Vaidya. Fibrinogen excretion in the urine and immunoreactivity in the kidney serves as a translational biomarker for acute kidney injury. *Am J Pathol*, 181(3):818–28, 2012.

[88] L. Vandelli, M. Marietta, M. Gambini, M. Cavazzuti, T. Trenti, M. A. Cenci, F. Casoni, G. Bigliardi, R. Pentore, P. Nichelli, and A. Zini. Fibrinogen decrease after intravenous thrombolysis in ischemic stroke patients is a risk factor for intracerebral hemorrhage. *J Stroke Cerebrovasc Dis*, 24(2):394–400, 2015.

[89] Sadahiro Nomura, Shiro Kashiwagi, Haruhide Ito, Yusuke Mimura, and Kazuyuki Nakamura. Degradation of fibrinogen and fibrin by plasmin and nonplasmin proteases in the chronic subdural hematoma: Evaluation by sodium dodecyl sulfate-polyacrylamide gel electrophoresis and immunoblot. *Electrophoresis*, 14(1):1318–1321, 1993.

[90] M. A. Gok, B. K. Shenton, R. Peaston, C. Cornell, H. Robertson, M. Mathers, J. D. Aitchison, J. H. Dark, D. Mantle, and D. Talbot. Improving the quality of kidneys from non-heart-beating donors, using streptokinase: an animal model. *Transplantation*, 73(12):1869–74, 2002.

[91] J. B. Seal, H. Bohorquez, T. Reichman, A. Kressel, A. Ghanekar, A. Cohen, I. D. McGilvray, M. S. Cattral, D. Bruce, P. Greig, I. Carmody, D. Grant, M. Selzner, and G. Loss. Thrombolytic protocol minimizes ischemic-type biliary complications in liver transplantation from donation after circulatory death donors. *Liver Transpl*, 21(3):321–8, 2015.

[92] K. J. Woodside, D. A. Goldfarb, J. C. Rabets, E. Q. Sanchez, D. J. Lebovitz, J. A. Schulak, J. J. Fung, and B. Eghtesad. Enhancing kidney function with thrombolytic therapy following donation after cardiac death: a multicenter quasi-blinded prospective randomized trial. *Clin Transplant*, 29(12):1173–80, 2015.

[93] J. J. Roelofs, K. M. Rouschop, G. J. Teske, G. T. Wagenaar, N. Claessen, J. J. Weening, T. van der Poll, and S. Florquin. Endogenous tissue-type plasminogen activator is protective during ascending urinary tract infection. *Nephrol Dial Transplant*, 24(3):801–8, 2009.

[94] E. Greenwald and K. Yuki. A translational consideration of intercellular adhesion molecule-1 biology in the perioperative setting. *Transl Perioper Pain Med*, 1(2):17–23, 2016.

[95] V. L. Chen, A. K. Le, O. Podlaha, J. Estevez, B. Li, P. Vutien, E. T. Chang, Y. Rosenberg-Hasson, S. Pflanz, Z. Jiang, D. Ge, A. Gaggar, and M. H. Nguyen. Soluble intercellular adhesion molecule-1 is associated with hepatocellular carcinoma risk: multiplex analysis of serum markers. *Sci Rep*, 7(1):11169, 2017.

[96] Yukihiro Shimizu, Masami Minemura, Takashi Tsukishiro, Yoshirou Kashii, Megumi Miyamoto, Hiroshi Nishimori, Kiyohiro Higuchi, and Akiharu Watanabe. Serum concentration of intercellular adhesion molecule–1 in patients with hepatocellular carcinoma is a marker of the disease progression and prognosis. *Hepatology*, 22(2):525–531, 1995.

[97] W. J. Lee, L. K. Chen, C. K. Liang, L. N. Peng, S. T. Chiou, and P. Chou. Soluble icam-1, independent of il-6, is associated with prevalent frailty in community-dwelling elderly taiwanese people. *PLoS One*, 11(6):e0157877, 2016.

[98] D. K. de Vries, J. H. Lindeman, D. Tsikas, E. de Heer, A. Roos, J. W. de Fijter, A. G. Baranski, J. van Pelt, and A. F. Schaapherder. Early renal ischemia-reperfusion injury in humans is dominated by il-6 release from the allograft. *Am J Transplant*, 9(7):1574–84, 2009.

[99] T. Tanaka, M. Narazaki, and T. Kishimoto. Il-6 in inflammation, immunity, and disease. *Cold Spring Harb Perspect Biol*, 6(10):a016295, 2014.

[100] C. Steichen, S. Giraud, D. Bon, B. Barrou, L. Badet, E. Salame, T. Kerforne, G. Allain, J. Roumy, C. Jayle, P. Hannaert, T. Hauet, and R. Thuillier. Barriers and advances in kidney preservation. *Biomed Res Int*, 2018:9206257, 2018.

[101] M. I. Bellini, J. Yiu, M. Nozdrin, and V. Papalois. The effect of preservation temperature on liver, kidney, and pancreas tissue atp in animal and preclinical human models. *J Clin Med*, 8(9), 2019.

[102] D. M. Summers, R. J. Johnson, A. Hudson, D. Collett, C. J. Watson, and J. A. Bradley. Effect of donor age and cold storage time on outcome in recipients of kidneys donated after circulatory death in the uk: a cohort study. *Lancet*, 381(9868):727–34, 2013.

[103] F. O. Belzer and J. H. Southard. Principles of solid-organ preservation by cold storage. *Transplantation*, 45(4):673–6, 1988.

[104] G. M. Collins, Maria Bravo-Shugarman, and P. I. Terasaki. Kidney preservation for transportation. *The Lancet*, 294(7632):1219–1222, 1969.

[105] F. O. Belzer, B. S. Ashby, P. F. Gulyassy, and M. Powell. Successful seventeen-hour preservation and transplantation of human-cadaver kidney. *N Engl J Med*, 278(11):608–10, 1968.

[106] J. P. Nicolay, V. Thorn, C. Daniel, K. Amann, B. Siraskar, F. Lang, C. Hillgruber, T. Goerge, S. Hoffmann, C. Gorzelanny, V. Huck, C. Mess, T. Obser, R. Schneppenheim, I. Fleming, M. F. Schneider, and S. W. Schneider. Cellular stress induces erythrocyte assembly on intravascular von willebrand factor strings and promotes microangiopathy. *Sci Rep*, 8(1):10945, 2018.

[107] M. W. J. Smeets, M. J. Mourik, H. W. M. Niessen, and P. L. Hordijk. Stasis promotes erythrocyte adhesion to von willebrand factor. *Arterioscler Thromb Vasc Biol*, 37(9):1618–1627, 2017.

[108] K. Hashimoto, B. Eghtesad, G. Gunasekaran, M. Fujiki, T. D. Uso, C. Quintini, F. N. Aucejo, D. M. Kelly, C. G. Winans, D. P. Vogt, B. M. Parker, S. A. Irefin, C. M. Miller, and J. J. Fung. Use of tissue plasminogen activator in liver transplantation from donation after cardiac death donors. *Am J Transplant*, 10(12):2665–72, 2010.

[109] A. D. Shapiro, C. Nakar, J. M. Parker, G. R. Albert, J. E. Moran, K. Thibaudeau, N. Thukral, B. M. Hardesty, P. Laurin, and P. M. Sandset. Plasminogen replacement therapy for the treatment of children and adults with congenital plasminogen deficiency. *Blood*, 131(12):1301–1310, 2018.

[110] K. Tefs, M. Gueorguieva, J. Klammt, C. M. Allen, D. Aktas, F. Y. Anlar, S. D. Aydogdu, D. Brown, E. Ciftci, P. Contarini, C. E. Dempfle, M. Dostalek, S. Eisert, A. Gokbuget, O. Gunhan, A. A. Hidayat, B. Hugle, M. Isikoglu, M. Irkec, S. K. Joss, S. Klebe, C. Kneppo, I. Kurtulus, R. P. Mehta, K. Ornek, R. Schneppenheim, S. Seregard, E. Sweeney, S. Turtschi, G. Veres, P. Zeitler, M. Ziegler, and V. Schuster. Molecular and clinical spectrum of type i plasminogen deficiency: A series of 50 patients. *Blood*, 108(9):3021–6, 2006.

[111] D. Collen, E. B. Ong, and A. J. Johnson. Human plasminogen: in vitro and in vivo evidence for the biological integrity of nh2-terminal glutamic acid plasminogen. *Thromb Res*, 7(4):515–29, 1975.

[112] F. J. Castellino and V. A. Ploplis. Structure and function of the plasminogen/plasmin system. *Thromb Haemost*, 93(4):647–54, 2005.

[113] Plasminogen deficiency clinical trials, 2020.

[114] E. Song, A. Gaudin, A. R. King, Y. E. Seo, H. W. Suh, Y. Deng, J. Cui, G. T. Tietjen, A. Huttner, and W. M. Saltzman. Surface chemistry governs cellular tropism of nanoparticles in the brain. *Nat Commun*, 8:15322, 2017.

[115] A. S. Ricciardi, R. Bahal, J. S. Farrelly, E. Quijano, A. H. Bianchi, V. L. Luks, R. Putman, F. Lopez-Giraldez, S. Coskun, E. Song, Y. Liu, W. C. Hsieh, D. H. Ly, D. H. Stitelman, P. M. Glazer, and W. M. Saltzman. In utero nanoparticle delivery for site-specific genome editing. *Nat Commun*, 9(1):2481, 2018.

[116] N. Sharma, A. Mahajan, and Y. A. Qazi. Marginal kidney transplantation: the road less traveled. *Curr Opin Organ Transplant*, 24(1):92–96, 2019.

[117] Y. Yang, H. Wang, M. Kouadir, H. Song, and F. Shi. Recent advances in the mechanisms of nlrp3 inflammasome activation and its inhibitors. *Cell Death Dis*, 10(2):128, 2019.

[118] E. F. Carney. Inflammation: Activated protein c inhibits inflammasome activation in iri. *Nat Rev Nephrol*, 13(11):662, 2017.

[119] J. R. DiRito, S. A. Hosgood, G. T. Tietjen, and M. L. Nicholson. The future of marginal kidney repair in the context of normothermic machine perfusion. *Am J Transplant*, 18(10):2400–2408, 2018.

[120] S. A. Hosgood and M. L. Nicholson. First in man renal transplantation after ex vivo normothermic perfusion. *Transplantation*, 92(7):735–8, 2011.

[121] R. C. Coll, J. R. Hill, C. J. Day, A. Zamoshnikova, D. Boucher, N. L. Massey, J. L. Chitty, J. A. Fraser, M. P. Jennings, A. A. B. Robertson, and K. Schroder. Mcc950 directly targets the nlrp3 atp-hydrolysis motif for inflammasome inhibition. *Nat Chem Biol*, 15(6):556–559, 2019.

[122] E. E. Hesketh, A. Czopek, M. Clay, G. Borthwick, D. Ferenbach, D. Kluth, and J. Hughes. Renal ischaemia reperfusion injury: a mouse model of injury and regeneration. *J Vis Exp*, (88), 2014.

[123] C. L. Edelstein. Biomarkers of acute kidney injury. *Adv Chronic Kidney Dis*, 15(3):222–34, 2008.

[124] A. A. Shigeoka, J. L. Mueller, A. Kambo, J. C. Mathison, A. J. King, W. F. Hall, S. Correia Jda, R. J. Ulevitch, H. M. Hoffman, and D. B. McKay. An inflammasome-independent role for epithelial-expressed nlrp3 in renal ischemia-reperfusion injury. *J Immunol*, 185(10):6277–85, 2010.

[125] Y. Fan, L. Du, Q. Fu, Z. Zhou, J. Zhang, G. Li, and J. Wu. Inhibiting the nlrp3 inflammasome with mcc950 ameliorates isoflurane-induced pyroptosis and cognitive impairment in aged mice. *Front Cell Neurosci*, 12:426, 2018.

[126] R. C. Coll, A. A. Robertson, J. J. Chae, S. C. Higgins, R. Munoz-Planillo, M. C. Inserra, I. Vetter, L. S. Dungan, B. G. Monks, A. Stutz, D. E. Croker, M. S. Butler, M. Haneklaus, C. E. Sutton, G. Nunez, E. Latz, D. L. Kastner, K. H. Mills, S. L. Masters, K. Schroder, M. A. Cooper, and L. A. O'Neill. A small-molecule inhibitor of the nlrp3 inflammasome for the treatment of inflammatory diseases. *Nat Med*, 21(3):248–55, 2015.

[127] R. S. Al-Lamki, J. R. Bradley, and J. S. Pober. Human organ culture: Updating the approach to bridge the gap from in vitro to in vivo in inflammation, cancer, and stem cell biology. *Front Med (Lausanne)*, 4:148, 2017.

[128] C. Yong, S. A. Hosgood, and M. L. Nicholson. Ex-vivo normothermic perfusion in renal transplantation: past, present and future. *Curr Opin Organ Transplant*, 21(3):301–7, 2016.

[129] M. Salvadori, G. Rosso, and E. Bertoni. Update on ischemia-reperfusion injury in kidney transplantation: Pathogenesis and treatment. *World J Transplant*, 5(2):52–67, 2015.

[130] A. P. Perera, R. Fernando, T. Shinde, R. Gundamaraju, B. Southam, S. S. Sohal, A. A. B. Robertson, K. Schroder, D. Kunde, and R. Eri. Mcc950, a specific small molecule inhibitor of nlrp3 inflammasome attenuates colonic inflammation in spontaneous colitis mice. *Sci Rep*, 8(1):8618, 2018.

[131] S. Ismael, L. Zhao, S. Nasoohi, and T. Ishrat. Inhibition of the nlrp3-inflammasome as a potential approach for neuroprotection after stroke. *Sci Rep*, 8(1):5971, 2018.

[132] E. Theofani, M. Semitekolou, I. Morianos, K. Samitas, and G. Xanthou. Targeting nlrp3 inflammasome activation in severe asthma. *J Clin Med*, 8(10), 2019.

[133] R. Gordon, E. A. Albornoz, D. C. Christie, M. R. Langley, V. Kumar, S. Mantovani, A. A. B. Robertson, M. S. Butler, D. B. Rowe, L. A. O'Neill, A. G. Kanthasamy, K. Schroder, M. A. Cooper, and T. M. Woodruff. Inflammasome inhibition prevents alpha-synuclein pathology and dopaminergic neurodegeneration in mice. *Sci Transl Med*, 10(465), 2018.

[134] Y. Yu, Y. Cheng, Q. Pan, Y. J. Zhang, D. G. Jia, and Y. F. Liu. Effect of the selective nlrp3 inflammasome inhibitor mcc950 on transplantation outcome in a pig liver transplantation model with organs from donors after circulatory death preserved by hypothermic machine perfusion. *Transplantation*, 103(2):353–362, 2019.

[135] H. et al. Lodish. *Section 15.1 Diffusion of Small Molecules across Phospholipid Bilayers*. W. H. Freeman, New York, 2000.

[136] J. Fan, K. Xie, L. Wang, N. Zheng, and X. Yu. Roles of inflammasomes in inflammatory kidney diseases. *Mediators Inflamm*, 2019:2923072, 2019.

[137] N. Kamaly, B. Yameen, J. Wu, and O. C. Farokhzad. Degradable controlled-release polymers and polymeric nanoparticles: Mechanisms of controlling drug release. *Chem Rev*, 116(4):2602–63, 2016.

[138] M. L. Nicholson and S. A. Hosgood. Renal transplantation after ex vivo normothermic perfusion: The first clinical study. *American Journal of Transplantation*, 13(5):1246–1252, 2013.

[139] A. M. Hameed, H. C. Pleass, G. Wong, and W. J. Hawthorne. Maximizing kidneys for transplantation using machine perfusion: from the past to the future: A comprehensive systematic review and meta-analysis. *Medicine (Baltimore)*, 95(40):e5083, 2016.

[140] S. J. Tingle, R. S. Figueiredo, J. A. Moir, M. Goodfellow, D. Talbot, and C. H. Wilson. Machine perfusion preservation versus static cold storage for deceased donor kidney transplantation. *Cochrane Database Syst Rev*, 3:CD011671, 2019.

[141] A. Weissenbacher, G. Vrakas, D. Nasralla, and C. D. L. Ceresa. The future of organ perfusion and re-conditioning. *Transpl Int*, 32(6):586–597, 2019.

[142] C. D. L. Ceresa, D. Nasralla, C. C. Coussios, and P. J. Friend. The case for normothermic machine perfusion in liver transplantation. *Liver Transpl*, 24(2):269–275, 2018.

[143] D. Nasralla, C. C. Coussios, H. Mergental, M. Z. Akhtar, A. J. Butler, C. D. L. Ceresa, V. Chiocchia, S. J. Dutton, J. C. Garcia-Valdecasas, N. Heaton, C. Imber, W. Jassem, I. Jochmans, J. Karani, S. R. Knight, P. Kocabayoglu, M. Malago, D. Mirza, P. J. Morris, A. Pallan, A. Paul, M. Pavel, Mtpr Perera, J. Pirenne, R. Ravikumar, L. Russell, S. Upponi, C. J. E. Watson, A. Weissenbacher, R. J. Ploeg, P. J. Friend, and Europe Consortium for Organ Preservation in. A randomized trial of normothermic preservation in liver transplantation. *Nature*, 557(7703):50–56, 2018.

[144] T. D. Adams, M. Patel, S. A. Hosgood, and M. L. Nicholson. Lowering perfusate temperature from 37 degrees c to 32 degrees c diminishes function in a porcine model of ex vivo kidney perfusion. *Transplant Direct*, 3(3):e140, 2017.

[145] J. M. Kaths, J. Y. Cen, Y. M. Chun, J. Echeverri, I. Linares, S. Ganesh, P. Yip, R. John, D. Bagli, I. Mucsi, A. Ghanekar, D. R. Grant, L. A. Robinson, and M. Selzner. Continuous normothermic ex vivo kidney perfusion is superior to brief normothermic perfusion following static cold storage in donation after circulatory death pig kidney transplantation. *Am J Transplant*, 17(4):957–969, 2017.

[146] J. W. McGowan and 3rd Bidwell, G. L. The use of ex vivo whole-organ imaging and quantitative tissue histology to determine the bio-distribution of fluorescently labeled molecules. *J Vis Exp*, (118), 2016.

[147] M. J. Lee, O. Veiseh, N. Bhattarai, C. Sun, S. J. Hansen, S. Ditzler, S. Knoblaugh, D. Lee, R. Ellenbogen, M. Zhang, and J. M. Olson. Rapid pharmacokinetic and biodistribution studies using cholorotoxin-conjugated iron oxide nanoparticles: a novel non-radioactive method. *PLoS One*, 5(3):e9536, 2010.

[148] W. Cheng, F. Zhao, C. Y. Tang, X. W. Li, M. Luo, and S. B. Duan. Comparison of iohexol and iodixanol induced nephrotoxicity, mitochondrial damage and mitophagy in a new contrast-induced acute kidney injury rat model. *Arch Toxicol*, 92(7):2245–2257, 2018.

[149] D. R. Campbell, B. K. Flemming, W. F. Mason, S. A. Jackson, D. J. Hirsch, and K. J. MacDonald. A comparative study of the nephrotoxicity of iohexol, iopamidol and ioxaglate in peripheral angiography. *Can Assoc Radiol J*, 41(3):133–7, 1990.

[150] U. Bilati, E. Allemann, and E. Doelker. Development of a nanoprecipitation method intended for the entrapment of hydrophilic drugs into nanoparticles. *Eur J Pharm Sci*, 24(1):67–75, 2005.

[151] abcam. Elisa sample preparation guide. 2018.

Appendix A

Materials and Methods

A.1 Chapter 1: Delivering targeted nanoparticles during NMP

A.1.1 Ethical approvals

In vitro experimentation with HUVECs from de-identified sources has been classified as nonhuman subject research by the Yale's Institutional Review Board. Ethical approval for experiments with human kidney was granted by the National Research Ethics Commission in the United Kingdom. Consent for the use of the organs for research was obtained from the donor family by the specialist nurses in organ donation before organ retrieval. Kidneys were retrieved by one of the U.K. National Organ Retrieval Services teams. After *in situ* flushing of the abdominal organs with cold preservation solution, kidneys were retrieved and then stored by static cold storage. Eight kidneys that were deemed unsuitable for transplantation were recruited into the study.

A.1.2 Materials

PLA-PEG copolymer (molecular weight, 16 to 5 kDa) was purchased from PolySciTech and used as received without further purification. Anhydrous dimethyl sulfoxide (DMSO), DiI and DiO stains, and Fisherbrand Superfrost Microscope Slides were purchased from Life Technologies.Ulex vascular stain was purchased fromVector Laboratories either preconjugated with fluorescein isothiocyanate or unconjugated for later conjugation to AlexaFluor 633-N-hydroxysuccinimide following the vendor's supplied protocol.

A.1.3 NP formulation

NPs were prepared by a nanoprecipitation procedure [150]. PLA-PEG was dissolved at a concentration of 100 mg/mL in DMSO and then diluted to the desired concentration for NP formulation (typically about 55 mg/mL for about 165-nm NPs used in this study), along with addition of either DiI or DiO dye also dissolved inDMSO. NPs were loaded with DiI or DiO dye at a final dye/polymer ratio of 0.5% (w/w). The dye/polymer solution in DMSO was added dropwise to vigorously stirringsterile deionized H_2O (diH_2O) in batches of 300 mL of polymer/dye solution added to 1.2mL of diH2O, with identical repetitions performed to generate a full NP batch. NPs were subsequently filtered through a 1.2-mm cellulose acetate membrane (GE Healthcare Life Sciences) filter to remove any free-dye or polymer aggregates and then pooled. The NP solutions were then transferred in batches to dialysis cassettes (12-mL volume; molecular weight cutoff, 10,000; Slide-A-Lyzer, Thermo Fisher Scientific) and dialyzed against two exchanges of about 2.2 liters of diH2O at room temperature to remove excess DMSO. After dialysis, NPs were aliquoted and snap-frozen in liquid N_2. One aliquot from each NP batch was lyophilized in a preweighed tube to determine the NP concentration. Standard NP concentration was typically about 5 mg/mL before Ab conjugation.

A.1.4 Ab surface conjugation

Ab-conjugated PLA-PEG NPs were generated via 1-ethyl-3-(3-dimethylaminopropyl)carbodiimide hydrochloride-mediated COOH-NH_2 coupling. Commercial Ab were purchased from BD Biosciences (CD31, clone WM59; Isotype, clone MOPC-21) and subsequently dialyzed overnight in dialysis cassettes (0.5 mL; molecular weight cutoff, 10,000; Slide-A-Lyzer, Thermo Fisher Scientific) to remove sodium azide, which can inhibit the coupling reaction. After dialysis, the protein concentration was adjusted (if necessary) to 0.55 mg/mL by addition of sterile Dulbecco's phosphate-buffered saline (Thermo Fisher Scientific).

A.1.5 Cell culture

HUVECs pooled from three separate donors were obtained from the Yale Vascular Biology and Transplantation tissue culture core laboratory, where they were isolated from fresh umbilical veins by treatment with collagenase and subsequently cultured in gelatin-coated tissue culture plastic plates using M199 medium supplemented with 20% v/v fetal bovine serum, 2% L-glutamine, 1% penicillin and streptomycin, and 1% (v/v) EC growth supplement (fibroblast growth factor-1). All cell culture experiments were performed using cells passaged

four or fewer times. For static NP incubation, cells were cultured for at least 4 to 5 days after reaching full confluence to ensure the formation of mature cell-cell junctions to best mimic *in vivo* conditions. The medium was exchanged every 2 to 3 days during these culture periods to ensure that the cells remained viable. Cells were visually inspected before all experiments to ensure cell viability.

A.1.6 Normothermic machine perfusion

After arrival, the kidneys were prepared, and the renal artery, vein, and ureter were cannulated. The kidneys were weighed before undergoing *ex vivo* NMP [120, 138]. Briefly, the *ex vivo* kidney perfusion circuit was designed using pediatric cardiopulmonary bypass technology (Medtronic) and consisted of a centrifugal blood pump (Bio-Pump 560), a heat exchanger (Chalice Medical), a venous reservoir (Medtronic), 1/4-inch polyvinyl chloride tubing, and a Pixie membrane oxygenator (Medtronic). The hardware included a speed controller, a TX50P flow transducer, and a temperature probe (Cole-Parmer). Two Alaris infusion pumps (CareFusion) were also incorporated into the system. The circuit was primed with a perfusate solution (Ringer's solution, Baxter Healthcare) and one unit of ABO-compatible packed red cells from the blood bank. Twenty-five milliliters of 10% mannitol (Baxter Healthcare), 8 mg of dexamethasone (Organon Laboratories), and 2 mL of heparin (1000 IU/mL; CP Pharmaceuticals) were added to the perfusate. Sodium bicarbonate (8.4%; Fresenius Kabi) was added to normalize the pH. A nutrient solution (NuTRIflex, B. Braun)with 25 mL of 8.4% sodium bicarbonate, 100 IU of insulin (Novo Nordisk), and multivitamins (Cernevit, Baxter Healthcare) was infused into the circuit at a rate of 20 mL/hour. Prostacyclin (0.5 mg; Flolan, GlaxoWellcome) was infused into the arterial arm of the circuit at a rate of 4mL/hour, and 5%glucose (Baxter Healthcare) was infused at 7 mL/hour. Ringer's solution was used to replace urine output milliliter-for-milliliter.

Kidneys were perfused at a set mean arterial pressure (70 to 75 mmHg). The plasma-free RBC-based perfusate was circulated from the venous reservoir through the centrifugal pump into the membrane oxygenator, where it was oxygenated and also warmed to 36^oC. It then flowed through the arterial limb of the circuit to the renal artery. Venous return from the renal vein was fed back into the reservoir [23]. Renal blood flow (RBF) was monitored continuously during NMP, and the total urine output was recorded. Pre-perfusion wedge biopsies and wedge biopsies were collected at various time points, as noted in Results. The tissue was either fixed in 10% formal saline or snap-frozen in liquid nitrogen and then stored at -80^oC. Samples of perfusate and urine were also collected at the same time points and stored at -80^oC.

The quality of each kidney was assessed on the basis of the macroscopic appearance, the mean RBF, and the total amount of urine produced. For macroscopic assessment, each kidney was categorized into one of three groups and scored according to its macroscopic appearance as follows: (i) grade I, excellent perfusion (global pink appearance); (ii) grade II, moderate perfusion (patchy pink and purple appearance, which either remained or improved during NMP); (iii) grade III, poor perfusion (global mottling and purple and black appearance, which remained throughout NMP). Kidneys with a mean RBF below the threshold (< 50 ml/min per 100 g) were given an additional score of 1. Kidneys producing less than the threshold volume of urine (< 43 ml/hour) were also given an additional score of 1. Therefore, overall NMP assessment scores can range from 1 (indicating the least injury) to 5 (the most severe). Six of the eight kidneys enrolled in this study had an NMP assessment score of 2 (kidneys 1 to 5 and 8), whereas kidneys 6 and 7 had a score of 1.

A.1.7 Quantitative microscopy on tissue biopsy sample

Snap-frozen wedge biopsies were cryosectioned on a microtome to a thickness of either 10 or 20 μm. Sections were imaged without fixation to avoid any alteration in dye-loaded NP signal. Ulex staining was performed rapidly with about 15 min of Ulex (Vector Laboratories) conjugated with Alexa Fluor 633 (Life Technologies) after standard conjugation procedures. After staining, sections were washed three times for 5 min each with DPBS and then mounted with Hardmount medium (Vector Laboratories) and coverslipped. Independent images were collected by raster scanning across cryosections, with typically three sections per condition and typically at least seven or more images of regions containing glomeruli or solely interstitial microvessels per section (corresponding to at least 15 images per section typically). Images were sorted, filtered, and processed using custom MATLAB code to distinguish glomerular vessels from surrounding microvasculature. Finally, the background-subtracted NP fluorescent signal was quantified for each image; backgrounds were determined by imaging sections from biopsies sampled before introduction of NP. For single-color experiments, these intensity values were then normalized to the vascular area of each corresponding image, as determined by Ulex staining. For two color experiments, the total background subtracted signal from DiI (red) CD31-NPs was normalized to the DiO (green) isotype-NPs and expressed as a specificity ratio with 1 corresponding to nonspecific accumulations and values > 1 corresponding to CD31-specific accumulation. Images were collected using a Semrock GFP-1828A bandpass filter set (excitation, 470 to 495 nm; emission, 505 to 535 nm) and a Chroma TRITC/DiI/Cy3 filter set (excitation, 525 to 550 nm; emission, 580 to 630 nm) with an air immersion apochromatic 20× objective (NA, 0.95; Olympus) or 40× objective (NA, 0.90; Olympus) on an Olympus Z71 inverted microscope illuminated by a light-emitting

diode (LED) light source (Olympus L300) with each LED at full illumination intensity. These filter sets and illumination setup ensured no spectral bleed with these NPs, which is a prerequisite for proper implementation of this technique. Quantitative equivalence of the two color NPs was confirmed by adding concentrated NPs to the sample mounting medium with minimal dilution. NPs were imaged in an identical plane as the positive Ulex stain to ensure that any signal absorption would be identical to the standard imaging conditions. All images were captured by an Olympus Retiga R6 CCD camera. Images of two-color NP accumulation are presented as thresholded images so that regions of low and high levels of accumulation can be equally appreciated. Data analysis, fitting, and statistical analysis were performed in GraphPad Prism.

A.2 Chapter 2: Identifying and treating microvascular obstructions

A.2.1 Ethical Approvals

U.K. transplant declined kidneys

Consent for the use of transplant-declined kidneys for research was obtained from the donor family by the specialist nurses in organ donation before organ retrieval. Consent for research was obtained by The North East Newcastle & North Tyneside 2 research ethics committee (15/NE/0408). Kidneys were retrieved by one of the U.K. National Organ Retrieval Services teams. After *in situ* flushing of the abdominal organs with cold University of Wisconsin preservation solution, kidneys were retrieved and then stored by static cold storage, packed in ice. 23 kidneys that were deemed unsuitable for transplantation were recruited into the study. Discard organ characteristics used in the experimental tPA series can be seen in Table 2.2

U.S. transplant declined kidneys

Prior to receiving any transplant-declined human kidneys donors and/or donor families consented for their kidneys to be used for research through the New England Donor Services (NEDS). In the U.S., since the donor is deceased, this research is not considered human subject research as defined in the HHS Policy for Protection of Human Research Subjects 45 CFR 46.102. HIPAA is still invoked with these specimens and all kidneys used have been de-identified from their deceased organ donors.

Multi-center randomized control trial

Human renal cortex biopsies from 15 different donors of the multi-center randomized control trial comparing cold storage to NMP (ISRCTN15821205) were taken from the control arm (cold storage) before and 30 minutes after transplantation. These samples have been fixed in 10% formalin. As the study is still ongoing, I currently do not have access to outcome data. Donor characteristics can be see in Table 2.1. The study protocol and trial documents including the consent form and participant information sheet have been approved by the NHS Health Research Authority East of England, Cambridge Central Research Committee (15/EE/0356). Approval has also been granted by the NHS Research & Development (R&D) department and will be sought at each participating center [26].

A.2.2 Normothermic machine perfusion

After arrival, the kidneys were benched, and the renal artery, vein, and ureter were cannulated with 14 Fr., 24 Fr., and 10 Fr cannula respectively. The kidneys were weighed before undergoing ex vivo NMP in order to normalize perfusion parameters. Briefly, the *ex vivo* kidney perfusion circuit was designed using pediatric cardiopulmonary bypass technology (Medtronic) and consisted of a centrifugal blood pump (Bio-Pump 560), a heat exchanger (Chalice Medical), a venous reservoir (Medtronic), 1/4-inch polyvinyl chloride tubing, and a Pixie membrane oxygenator (Medtronic). The hardware included a speed controller, a TX50P flow transducer, and a temperature probe (Cole-Parmer). Two Alaris infusion pumps (CareFusion) were also incorporated into the system. The circuit was primed with a perfusate solution (Ringer's solution, Baxter Healthcare) and one unit of ABO-compatible packed red cells from the blood bank. Fifteen milliliters of 10% mannitol (Baxter Healthcare), 6.67 mg of dexamethasone (Organon Laboratories), and 3 mL of heparin (1000 IU/mL; CP Pharmaceuticals) were added to the perfusate. Sodium bicarbonate (8.4%; Fresenius Kabi) was added to normalize the pH as necessary. Prostacyclin (0.5 mg; Flolan, Glaxo Wellcome) was infused into the arterial arm of the circuit at a rate of 5 mL/hour, and 5% glucose (Baxter Healthcare) was infused at 7 mL/hour. Ringer's solution was used to replace urine output milliliter-for-milliliter.

Kidneys were perfused at a set mean arterial pressure (75 to 85 mmHg). The plasma-free RBC-based perfusate was circulated from the venous reservoir through the centrifugal pump into the membrane oxygenator, where it was oxygenated and also warmed to 37^{o}C. It then flowed through the arterial limb of the circuit to the renal artery. Venous return from the renal vein was fed back into the reservoir. Renal blood flow (RBF) was monitored every five minutes during NMP, and the total urine output was recorded every thirty minutes. Cold

storage wedge biopsies and perfusion wedge biopsies were collected at various time points, as noted in tPA + plasminogen treatment. The tissue was either fixed in 10% formalin, snap-frozen in liquid nitrogen and then stored at -80^{o}C, or fixed in 2% glutaraldehyde, 2% formaldehyde in a 0.1M sodium cacodylate buffer and stored at 4^{o}C for TEM analysis. Samples of perfusate and urine were also collected as noted , centrifuged at 1,300g and their supernatants were snap frozen and stored at -80^{o}C.

A.2.3 TEM imaging

The human kidney cortex biopsy taken after 30 min of NMP was immersion-fixed in 2.5% glutaraldehyde and 2% paraformaldehyde in 0.1M cacodylate buffer (pH 7.4), then post-fixed in 1% OsO 4 in the same buffer at room temperature for 1 hour. After en bloc staining with 2% aqueous uranyl acetate for 30 min, tissue was dehydrated in a graded series of ethanol to 100%, followed by propylene oxide and finally embedded in EMBed 812 resin. Tissue blocks were polymerized in 60^{o}C oven overnight. Thin sections (60 nm) were cut by a Leica ultramicrotome (UC7) and post-stained with 2% uranyl acetate and lead citrate. Sample grids were examined in a FEI Tecnai transmission electron microscope at 80 kV of accelerating voltage, digital images were recorded with an Olympus Morada CCD camera and iTEM imaging software.

A.2.4 Fibrin(ogen) immunofluorescent staining

Frozen samples were cryosectioned to 4 μm and placed on Superfrost Plus glass slides (Fisher). Samples were stored at -80^{o}C until staining. Before staining, samples were air dried for 10 min and a square was drawn around each sample with a hydrophobic pen. Samples were treated with 1% paraformaldehyde for 10 min at room temperature, washed with PBS, and then blocked with 10% fetal bovine serum for 30 min on ice. Samples were washed and stained with 100 μg/mL of monoclonal mouse anti-human fibrin antibody (MyBioSource) for 24 hours on ice. Samples were washed and stained with 8 μg/mL of 2° Ab (Alexa Fluor 546 goat anti-mouse IgM, Fischer) and 50 μg/mL of DyLight 649 Ulex for 1 hr. Samples were then washed and air dried for 10 min. 10 μL of Vectashield Hard Set mounting media were added to each sample preceding a coverslip. Mouse IgM (BioLegend) was used as an isotype control. 2% bovine serum albumin was used to dilute all staining reagents.

A.2.5 Fibrinogen protein levels

Snap-frozen kidney biopsies were thawed on ice and homogenized with an electric homogenizer in protein extraction and enhancement buffer (abcam). Levels of fibrinogen were measured using a Human ELISA Kit (abcam) and normalized to protein levels measured using a Pierce BCA protein assay kit (Thermofisher).

Fibrinogen protein presence and increase with CIT was also confirmed using Western blotting techniques (Supplemental Figure 10). Kidney protein lysate diluted to 1500 μg/mL was denatured at 100^{o}C for 5 min with 25% beta-mercaptoethanol by volume. 20 μL of the denatured protein and dye were added into the wells of the gel. 2 μL of pre-stained protein ladder (abcam) was loaded into the gel. The 4-20% Mini-Protean TGX stain-free precast SDS gel (Bio-Rad Laboratories, Hercules, CA, USA) was run at 150 V for 1 hour in SDS-PAGE buffer. Once the protein had migrated, it was transferred to a nitrocellulose membrane using the mini Trans-Blot cell (Bio-Rad Laboratories, Hercules, CA, USA) in transfer buffer (10% methanol, 190 M glycine, 25 mM Tris, pH 8.3) for 90 min at 90 V. Nitrocellulose membranes were stained with Ponceau S solution to confirm protein transfer. The nitrocellulose membranes were rinsed with1 X TBS-T (TBS; 50 mM Tris, 150 mM NaCl, pH to 7.5. TBS-T; + 0.1% Tween-20) and blocked for 1 hour at RT in TBST + 5% BSA. The membranes were stained overnight on a rocker at 4^{o}C in TBS-T in 5% BSA with anti-fibrinogen antibody (ab58207), mouse IgG1 (ab170190) for isotype control, or alpha-tubulin as a house keeping gene to confirm equal loading levels of protein. Membranes were washed 3x in TBST for 5 min/wash at RT. The next day, membranes were washed 4 times with TBS-T for 5 minutes before the addition of HRP-conjugated secondary antibody (ab205719) in 5% milk in TBS-T and gently rocked at RT for 1 hour. After secondary Ab incubation, wash steps were then repeated before membranes were incubated with 5 mL ECL substrate per membrane for 1 minute (ab65623). The presence of chemiluminescent bands (target protein) was visualized using the ChemiDoc MP imaging system (Bio-Rad Laboratories, Hercules, CA, USA).

A.2.6 Microvascular obstruction quantification

In the series of 12 kidneys, 5 total biopsies were collected per organ: one prior to NMP, one 30 min after the start of NMP and before tPA treatment, and three at 90 min after the start of NMP treatment. All biopsies were fixed in 10% formalin for 72 hours, embedded in paraffin, and cut to 4 μm thicknesses. Sections were stained with a martius scarlet blue (MSB) kit (tcs biosciences) to highlight erythrocytes (yellow), fibrin(ogen) (red), and collagen (blue) within the samples. 20 images per section and 3 sections per sample were imaged with light

microscopy for a robust quantification in experimental tPA work. Images were output in 2448 x 1920 pixels. Slides were imaged in a randomized, blinded fashion as to not bias imaging fields. Images were collected in a snake-like pattern making sure not to overlap fields of view.

To quantitatively and objectively assess the extent of vascular obstruction in each procured sample, bright field images were analyzed with code that isolated the microvascular obstructions based on color. The extent of microvascular obstruction was quantified by the total area of fibrin(ogen) (red with MSB stain) normalized to the total captured area (n = 20 regions per section). In order to ensure consistent color thresholding of the fibrin(ogen) stain color across samples, a MATLAB (v. R2017b) script was developed that sorts individual pixels by their RGB profile. In this program, the user provides initial input by identifying fibrin(ogen)-positive and fibrin(ogen)-negative features in a set of representative sample images. This input is used to generate a list of RGB profiles that are unique to pixels in positive regions (positive color map), which is then applied to filter pixels in all other images in the dataset. Each pixel is assigned a true or false score for fibrin(ogen) staining, generating a fibrin(ogen)-positive binary mask of each image. Within individual organ donors, staining was consistent (Figure 2.9). However, staining between organs tended to vary, even between samples processed at the same time (Figure 2.10). To control for this, positive regions of interest were identified for individual donors and used to create a color map for each donor.

A.2.7 tPA + plasminogen treatment

In order to test whether tPA in the presence of plasminogen was a viable agent to clear microvascular obstructions in pre-transplant kidneys, tPA and plasminogen was administered in a series of three single and three pairs of discarded human kidneys. tPA (altepase) was obtained from Addenbrooke's pharmacy in Cambridge. Plasminogen was purchased in 10-unit batches from Sigma Aldrich for use in a single perfusion circuit. NMP was performed as described above with a few minor modifications. (1) 10 μg/mL of plasminogen was added to the perfusate and allowed to circulate with the organ on circuit for 30 min prior to the administration of tPA. (2) tPA was administered 30 min post start of perfusion via a controlled infusion with 10% of the total dose delivered as a bolus into the arterial port and 90% of the dose delivered IV throughout the course of the hour-long treatment. tPA was delivered at a dose of 100 μg/kg of graft. Single wedge biopsies were collected after a period of cold storage, immediately prior to NMP, 30 min after the start of NMP while plasminogen was circulating, and three wedge biopsies were taken 90 min after the start of NMP, 60 min

after the initial dose of tPA was delivered. Wedge biopsies were minimized during NMP as to not disrupt flow measurements.

A.2.8 Biochemical measurements

Biochemical assays were implemented to confirm the resolution of microvascular obstructions. The experiments performed also give possible insight into the mechanisms behind the formation of microvascular obstructions. A plasmin activity assay (abcam) performed on perfusate samples was used to assess tPA-mediated conversion of plasminogen to plasmin. Fibrin degradation products were measured in the perfusate using a nonspecific Human D-Dimer ELISA (abcam) to quantify the extent of fibrinopeptide degradation. All outcomes were measured on a SpectraMax iD5 microplate reader. Perfusate samples, used for the aforementioned assays, were centrifuged at 1,600g for 10 min in heparinized tubes to isolate plasma immediately following collection, snap frozen in liquid nitrogen, and stored at -80^{o}C until testing. Wedge biopsies were snap frozen immediately after procurement, and were homogenized following a pre-established protocol from abcam [151].

A.2.9 Nanoparticle administration

To determine how tPA and plasminogen treatment impacted targeted delivery, ICAM2 targeted-NPs were formulated and conjugated as previously described [74]. Targeted-NPs (red) with control-NPs (green) were simultaneously injected into the arterial arms of the NMP circuit upstream in three separate pairs of kidneys. One kidney in each pair received tPA and plasminogen treatment while the other kidney underwent NMP without treatment. Biopsies were collected at the end of CS, 30 min after NMP started (before tPA treatment), after an hour of tPA treatment (before NP treatment), and after 4 hours of NP treatment. In each case, NPs were injected for a final circulating concentration of 50 μg/mL of targeted-NPs and 50 μg/mL of control-NPs.

A.2.10 Quantitative fluorescent microscopy on tissue biopsy sample

Snap-frozen wedge biopsies were cryosectioned on a microtome to a thickness 16 μm. Sections were imaged without fixation to avoid any alteration in dye-loaded NP signal. Vascular staining was performed rapidly with 30 min of DyLight 649 labeled Ulex Europaeus Agglutinin I (Vector Laboratories). After staining, sections were washed three times for 5 min each with DPBS and then mounted with Hardmount medium (Vector Laboratories) and coverslipped.

20 images of glomeruli or microvessels were collected for each of the three biopsies/kidney, resulting in 60 total images for both glomeruli and microvessels in each kidney. The background-subtracted NP fluorescent signal was quantified for each image; backgrounds were determined by imaging sections from biopsies sampled before introduction of NP. The total background subtracted signal from DiI (red) ICAM2-NPs was normalized to the DiO (green) isotype-NPs and expressed as a specificity ratio with 1 corresponding to nonspecific accumulations and values >1 corresponding to ICAM2 specific accumulation. Imaging conditions were validated as previously described [74]. All fluorescent microscopy was conducted with the Invitrogen EVOS FL Auto 2 Cell Imaging System.

A.2.11 Statistics

Distributions of kidney tissue images using quantitative microscopy did not follow normal distributions, so statistical analyses were performed using Wilcoxon signed-rank test. Significant differences in biochemical measurements were assessed with multiple non-parametric-tests. Differences in perfusion parameters were made with non-parametric paired t-tests, as the experimental comparisons were made in matched kidneys. All statistical analyses were conducted in Prism. 20 images per paraffin section were taken. Three paraffin sections per sample were cut and imaged in all experimental series.

A.3 Chapter 3: NLRP3 inflammasome inhibition during NMP

A.3.1 Murine renal ischemia reperfusion model

Animal husbandry

Female C57BL/6 (Charles River Laboratories, UK) and Nlrp3- derived from JAX stock 021302 (The Jackson Laboratory, USA) were maintained in pathogen free facilities with ad libitum food and water in Central Biomedical Services at Addenbrooke's Hospital site. All procedures were conducted under Project License number P7720A3D6.

Pre-operative care

Pre-operative care was performed by surgical technicians working for University Biomedical Services. Mice were anesthetized in an induction chamber using 5% isoflurane (Abbott Laboratories, USA) with 2.0 L/min oxygen. Following induction, mice were transferred to

a heating pad at 37^{o}C and anesthesia was maintained with 1.5% isoflurane with 2.0 L/min oxygen delivered via nose cone. The abdomen of the mouse was subsequently shaved using electrical clipper and sterilized using ethanol and chlorhexidine (Molnlycke, Sweden). 0.1 mg/kg buprenorphine was administered for pain relief following surgery for non-terminal procedures.

Surgery

Anesthetized mice were transferred from the pre-operative suite to the operating theater where they were placed on a heating pad attached to a homeothermic monitoring system (Harvard Apparatus, UK). Core temperature of the mice was monitored using rectal temperature probe. Mice were maintained at 37.0 $\pm$ 0.5^{o}C throughout the procedure. A midline laparotomy was performed and the bilateral renal pedicles were dissected to expose the renal artery and veins. All mice received 100 μL of either saline (n = 16) or 600 μg/mL of MCC950 (n = 4) injected into the inferior vena cava using a 30 gauge needle. For mice that were set to receive renal ischemic injury, 15mm microserrofine clamps (Fine Science Tools, Germany) were placed over the renal hila of each kidney for 24 minutes to occlude renal blood flow. Successful occlusion was confirmed through the development of a dark purple color in both kidneys. During this period of ischemia, the midline laparotomy was closed using 5-0 absorbable suture to maintain temperature. Following the period of ischemia, the clamps were removed and return to normal color was confirmed, indicating successful reperfusion. For sham operations (n = 8), the same procedure was mimicked but did not include the use of clamps. All procedures were performed under sterile conditions.

Post-operative care

Mice were recovered in a heated cabinet for 24 hours and monitored hourly for the first six hours to ensure proper wound healing at the site of incision. After 24 hours, mice were anesthetized and prepared for terminal surgeries for bilateral kidney and blood collection.

Procedure randomization

Once consistent, and reproducible renal injury was established in a cohort of wild type mice (n = 4), the four other conditions (1) wild type sham (n = 4), (2) NLRP3$^{-/-}$ sham (n = 4), (3) wild type MCC950 + IRI (n = 4), and (4) NLRP3$^{-/-}$ IRI (n = 4) were conducted in a random order using a random number generator.

Sample collection and storage

Mice were allowed to recover for 24 hours prior to tissue and blood collection. These samples were retrieved from the mice under terminal anesthesia. Approximately 500 μL of whole blood was collected from the inferior vena cava using a 27 gauge needle attached to a 1-mL syringe. Blood was transferred into 250 μL capillary action tubes and were temporarily stored on ice prior to centrifugation. Blood was then spun on a 4^{o}C table-top centrifuge for 10 minutes at 3000g. Serum was collected, snap frozen, and stored at -80^{o}C until further processing. Kidneys were excised from the mouse following blood collection. One randomly assigned kidney in the pair was snap frozen in liquid nitrogen. Frozen tissue was stored in cryovials at -80^{o}C until further processing. The other kidney was placed in 10% neutral buffered formalin and sent for paraffin embedding and H&E staining through Addenbrooke's histopathology services.

Sample processing

Mouse serum urea and creatinine levels were analyzed using enzymatic assays on the Siemens Healthineers Dimension EXL clinical chemistry system using reagents supplied by Siemens Healthineers (Newark, USA) at Addenbrooke's Core Biochemical Assay Laboratory.

A.3.2 Transplant declined human kidney experiments

Consent for the use of transplant-declined kidneys for research was obtained from the donor family by the specialist nurses in organ donation before organ retrieval. Consent for research was obtained by The North East Newcastle & North Tyneside 2 research ethics committee (15/NE/0408). Kidneys were retrieved by one of the U.K. National Organ Retrieval Services teams. After in situ flushing of the abdominal organs with cold University of Wisconsin preservation solution, kidneys were retrieved and then stored by static cold storage, packed in ice. 12 kidneys that were deemed unsuitable for transplantation were recruited into the study. Discard organ characteristics can be seen in Supplemental Table I. All organs in this study were retrieved from donors following brain death.

Cold storage human organ culture for MCC950 dose titration

Human organ culture Upon organ receipt, biopsies were taken and dissected into 1 mm^3 cubes in 37^{o}C M199 media supplemented with 10% fetal bovine serum and 1% penicillin streptomycin. Three 1 mm^3 tissue sections were placed in a well in a 96-well plate and incubated at 37^{o}C and atmospheric O_2 concentrations for 4 hours. with varying

concentrations of MCC950 in 200 μL of supplemented M199 media. Samples were processed in triplicate. Tissue was then transferred to a 96-well plate with 200 μL of gelatin veronal buffer (Sigma-Aldrich) supplemented with 10% high panel reactive antibody serum (Tissue Typing Lab, Addenbrooke's). The plate was then placed in a hypoxic chamber with 5% O_2 and incubated at 37^{o}C for 2 hours. Following this period of hypoxia, tissue was transferred back into another 96-well plate with complete M199 media and allowed to "reperfuse" under normoxic conditions for 2 hours at 37^{o}C.

Sample collection Following the period of reperfusion media and tissue samples were collected and snap frozen. Samples were stored at -80^{o}C until further processing.

Sample processing Using a 2X dilution IL-1β and IL-18 levels were measured in the media using a human IL-1β ELISA (abcam, ab214025) and IL-18 ELISA (Generon, UK) respectively.

MCC950 delivery during normothermic machine perfusion

Perfusion protocol Upon arrival, the kidneys were benched, and the renal artery, vein, and ureter were cannulated with 14 Fr., 24 Fr., and 10 Fr cannula respectively. The kidneys were weighed before undergoing ex vivo NMP in order to normalize perfusion parameters. The ex vivo kidney perfusion circuit used was designed as previously noted. The circuit was primed with a perfusate solution (Ringer's solution, Baxter Healthcare) and one unit of ABO-compatible packed red cells from the blood bank. Fifteen milliliters of 10% mannitol (Baxter Healthcare), 6.67 mg of dexamethasone (Organon Laboratories), and 3 mL of heparin (1000 IU/mL; CP Pharmaceuticals) were added to the perfusate. Sodium bicarbonate (8.4%; Fresenius Kabi) was added to normalize the pH as necessary. Prostacyclin (0.5mg; Flolan, Glaxo Wellcome) was infused into the arterial arm of the circuit at a rate of 5 mL/hour, and 5% glucose (Baxter Healthcare) was infused at 7 mL/hour. Ringer's solution was used to replace urine output milliliter-for-milliliter. Kidneys were perfused at a set mean arterial pressure (75to 85mmHg). The plasma-free RBC-based perfusate was circulated from the venous reservoir through the centrifugal pump into the membrane oxygenator, where it was oxygenated and also warmed to 37^{o}C. It then flowed through the arterial limb of the circuit to the renal artery. Venous return from the renal vein was fed back into the reservoir.

Renal blood flow (RBF) was monitored every five minutes for the first 90 minutes of NMP to monitor the stabilization of the organ and then every 30 minutes for the remaining 4 hours of perfusion. The total urine output was recorded every thirty minutes.

MCC950 injection After 90 minutes of perfusion, allowing the organ to stabilize a 10 mL bolus of 20 mg of MCC950 was injected into the arterial arm of the perfusion circuit upstream of the kidney in the treated condition. This lead to a final concentration of 100 μM of MCC950 in the circulating perfusate. In the untreated condition, 10 mL of saline was injected into the arterial arm as a control.

Sample collection and storage Wedge biopsies were collected prior to perfusion, at 90 minutes of perfusion (prior to treatment), and at the end of the 5.5 hour long perfusion. Biopsies were divided and the tissue was either fixed in 10% formalin or snap-frozen in liquid nitrogen and then stored at -80^{o}C. Samples of perfusate were collected prior to the organ being connected to the circuit, at 90 minutes of perfusion (prior to treatment), and at the end of the 5.5 hour long perfusion. Urine samples were collected at 90 minutes and 5.5 hours of perfusion. Perfusate and urine samples were centrifuged at 1,300g for 10 minutes at 4^{o}C. Supernatants were aliquoted, snap frozen, and stored at -80^{o}C until further analysis.

Sample processing The perfusate cytokine levels were analyzed by an electrochemiluminescence assay using the MesoScale Discovery (MSD) human Proinflammatory Panel 1 (MSD, Rockville, MD, USA) at Addenbrooke's Core Biochemical Assay Laboratory. This assay is a 10-plex sandwich immunoassay with an electrochemical detection system which is read of the MSD S600 reader.

Post-perfusion human organ culture Following the 5.5 hour period of perfusion, biopsies were dissected into 1 mm^3 cubes in 37^{o}C supplemented M199 media. Tissue was then immediately transferred to the hypoxic conditions followed by the reperfusion conditions as previously described.

A.3.3 Statistics

All statistical analyses were conducted in Prism.

A.4 Chapter 4: Whole organ viability assessments

A.4.1 Porcine organ recovery, preservation, and perfusion

30 porcine kidneys were used to develop CT imaging methods under conditions of cold storage and normothermic machine perfusion. Methods were initially established in a series of porcine kidneys obtained from a local slaughterhouse post-mortem. Once imaging

protocols were finalized, imaging was conducted in a series of porcine kidneys under our experimental control. Protocols for the care of all experimental animals in this study were approved by Yale IACUC and were designed to comply with The Guide for the Care and Use of Laboratory Animals, by the National Research Council (US) Institute for Laboratory Animal Research. Kidneys were procured using a DCD model of procurement. Animals were sedated, intubated, and maintained under general anesthesia until they were euthanized. Dissections were based on clinical DCD procurement procedures. The infrarenal aorta and inferior vena cava (IVC) were exposed, then the pigs were euthanized with phenobarbital. After a period of either minimal (0-5 min) or long (30 min) warm ischemia, the aorta was cannulated and flushed with 4-6 L of Custodiol HTK. The infrarenal cava was released in the abdomen, suprahepatic cava released in the chest, and descending thoracic aorta clamped. Flushing proceeded until effluent from the IVC cleared. Kidneys were subsequently procured *en block* and benched on the back table. The renal artery (RA) and ureters were cannulated (Cole-Parmer 1/8" – 1/4" leur lock adapter for the RA, and 14 Fr silicone catheter for the ureter) and flushed with an additional 0.5 L of Custodiol HTK and the kidney stored in preservation solution on ice comparable to clinical standard cold storage (SCS) until imaging or perfusion. Immediately prior to imaging, the kidneys were flushed with 500 mL of cold lactated ringer's (LR) to remove the preservation solution. To simulate reperfusion injury, porcine kidneys were perfused with autologous blood for 1 hour following well established experimental protocols [144].

A.4.2 Human organ recovery and preservation

11 transplant-declined human kidneys were obtained for imaging. 6 were used for cold storage imaging only, 3 for a pilot imaging series during NMP, and 2 for the pre/post NMP series. Transplant-declined human kidneys were obtained under a protocol approved by New England Donor Services (NEDS). Consent for the use of the organs for research was obtained from donor families by organ donation nurse specialists. Kidneys were retrieved by clinical organ recovery teams. After in situ flushing of the abdominal organs with cold preservation solution, kidneys were retrieved and stored by clinical protocols by either static cold storage, or hypothermic machine perfusion (LifePort Kidney Transporter from Organ Recovery Systems®, Itasca, IL). No specific selection criteria were applied to organ offers from NEDS and kidneys from both brain death and cardiac death donors were utilized. Donor demographic and organ characteristics for kidneys used in the experimental series are reported in Table 1. On arrival to the lab, kidneys were stored in ice in a 4^oC refrigerator in the preservation solution they were delivered. The kidneys were dissected to remove extrarenal fat. The renal artery (RA) and ureters were cannulated with a size appropriate

cannula (Cole-Parmer 1/8”-1/4” leur lock adapter, or cannula from hypothermic perfusion for the RA and 14Fr silicone catheter for the ureter). Kidneys were then stored under static cold conditions until imaging.

A.4.3 Computed tomography imaging protocols

All CT imaging was performed on a 64-slice GE clinical CT scanner at the Yale Translational Research Imaging Center. All imaging series utilized whole organ, helical scans and were obtained at 250mA and 80kEv. Contrast infusions were performed using a clinical contrast injector (MEDRAD Stellant Injection System). Custom MATLAB code was developed for image analysis to supplement analysis performed in HOROS, a freeware software package for analysis of dicom images.

A.4.4 Cold storage imaging

Cold storage imaging was performed on a setup where the contrast and crystalloid were infused using the clinical contrast infuser connected to a 3-way stopcock on the renal artery cannula. The other port on the 3-way stop cock was connected to a bag of cold LR, used to flush the preservation solution from the organ prior to imaging. The organ was positioned on a urocatch bag (Universal Medical) secured over a plastic container with renal vein extending away from the hilum to allow for contrast to passively drain away from the organ. Immediately prior to imaging, the kidneys were flushed with 500 mL of cold LR to remove the preservation solution. 5% iohexol contrast was infused at 1 mL/second for 50 seconds. When contrast infusion began, three sequential scans were obtained to capture major renal vascular filling. After a 5-minute delay, a fourth helical scan was obtained to capture microvascular deficits.

A.4.5 Normothermic machine perfusion imaging

Methods for perfusion imaging were developed with human kidneys 7-9. During the cold storage imaging prior to NMP, total contrast infused was reduced to 15 mL from 50 mL in an attempt to avoid oversaturating the organ. The kidneys were perfused for 30 minutes using an NMP protocol adapted from a well-established protocol [26]. During NMP imaging, contrast was delivered at 3 mL/second for 15 seconds. Repeat whole organ helical scans were obtained with before NMP (during cold-storage) and after ~5, ~10, ~20 min of NMP for HK07 and HK08; HK09 was measured at ~5, 10, 15 and 20 min after initiation of NMP.

A.4.6 Pre and post NMP imaging

The cold storage imaging protocol was used before and after NMP to identify the impact of the procedure on organ circulation. The pre-NMP imaging was performed as described in the cold storage section above. Following imaging, the kidney was flushed with 1L of cold LR to remove contrast. It was then perfused using NMP on a custom adapted pediatric cardiac bypass circuit in our lab as descried elsewhere for 1 hour while recording pressure, flow, and urine output. The kidney was then flushed with LR until effluent cleared, and was stored for 1 hour using SCS. Prior to repeat imaging, the kidney was flushed with 500 mL of cold LR and again imaged with the cold storage imaging protocol.

A.4.7 Statistics

All statistical analyses were conducted in Prism.

Appendix B

Supplementary Code

B.1 MATLAB code for two-color fluorescent microscopy quantification

```
function [ vasc ] = vasc_filter_2c_roi()
%Program to isolate glomerular versus microvasculature for kidney quantitation
%This version is for two color analysis

    warning('off', 'Images:initSize:adjustingMag');
    close all;

%Get file and read in ulex channel
    [FileName,PathName,FilterIndex] = uigetfile('.tif');
    cd(PathName);

    cd ..;

    d = dir;

for j = 3:length(d)

    cd(d(j).name);


    vasc.FileName = strcat(d(j).name,'_MMStack_Pos0.ome.tif');
```

```
    vasc.ulex.ui16 = imread(vasc.FileName,4);
    vasc.ulex_threshold = graythresh(vasc.ulex.ui16)*2^16;
    vasc.h = size(vasc.ulex.ui16,1);
    vasc.w = size(vasc.ulex.ui16,2);

%Generate black and white image


    vasc.ulex.bw = imbinarize(vasc.ulex.ui16,vasc.ulex_threshold/2^16);
    colormap('gray');
    vasc.ulex.adj = imadjust(vasc.ulex.ui16.*uint16(vasc.ulex.bw),[300 4000]/2^16);
    vasc.ulex.bw_r = uint16(cat(3,vasc.ulex.bw,zeros(2200,2688),
    zeros(2200,2688))*2^16);
    vasc.ulex.adj_w = cat(3,vasc.ulex.adj, vasc.ulex.adj, vasc.ulex.adj);
    imshow(vasc.ulex.bw_r+vasc.ulex.adj_w);



    glom_roi = input('Are there glomeruli? (1==yes, enter for no): ');

        if glom_roi == 1
             regofint = roipoly();
             vasc.ulex.glom.regofint = regofint;
             vasc.ulex.microv.regofint = abs(1-regofint);

             vasc.ulex.glom.bw = vasc.ulex.bw.*vasc.ulex.glom.regofint;
             vasc.ulex.glom.ui16 = vasc.ulex.ui16.*uint16(vasc.ulex.glom.bw);
             vasc.ulex.microv.bw = vasc.ulex.bw.*vasc.ulex.microv.regofint;
             vasc.ulex.microv.ui16 = vasc.ulex.ui16.*uint16(vasc.ulex.microv.bw);

             imshow(vasc.ulex.glom.bw);
             title(sprintf('Thresh = %d', round(vasc.ulex_threshold)));
             pause;
             close all;
```

```
        else
            regofint = zeros(2200,2688);
            vasc.ulex.glom.regofint = regofint;
            vasc.ulex.microv.regofint = abs(1-regofint);

            vasc.ulex.glom.bw = zeros(2200,2688);
            vasc.ulex.glom.ui16 = zeros(2200,2688);
            vasc.ulex.microv.bw = vasc.ulex.bw;
            vasc.ulex.microv.ui16 = vasc.ulex.ui16;
            close all;

        end


%Save vasc variable to vasc.mat
    save vasc.mat vasc;

    cd ..;


end

end



function [ np, data] = np_quantify_2cv2( np_background, np_thresh, scale )
%Program for quantification of NP signal in two color HK3-5
%experiments
%Input np_background and np_threshold as [dii dio]
%scale input is in terms of micron per pixel


%Navigate to parent folder of images then sequential move to image folder
%and load image and vasc filter mat file
```

```
    warning('off', 'Images:initSize:adjustingMag');

    np.dii.np_background = np_background(1);
    np.dio.np_background = np_background(2);

    [FileName,PathName,FilterIndex] = uigetfile('.tif');
    cd(PathName);

    cd ..;

    d = dir;

    np.data = zeros(length(d)-2,3);%Image number; area; mean

for j = 3:length(d)


    cd(d(j).name);


    np.FileName = strcat(d(j).name,'_MMStack_Pos0.ome.tif');


    np.dii.ui16 = imread(np.FileName,3);
    np.dio.ui16 = imread(np.FileName,2);

    load vasc.mat;

    np.dii.thresh = np_thresh(1);
    np.dio.thresh = np_thresh(2);

    np.dii.ui16_bw = imbinarize(np.dii.ui16, np.dii.thresh/2^16);
    np.dio.ui16_bw = imbinarize(np.dio.ui16, np.dio.thresh/2^16);

%Parse NP image for glom v microv
    np.dii.glom.ui16 = uint16(vasc.ulex.glom.regofint).*np.dii.ui16;
```

```
    np.dii.glom.bw = vasc.ulex.glom.regofint.
    *imbinarize(np.dii.ui16,np.dii.thresh/2^16);
    np.dii.glom.ui16_thresh = uint16(np.dii.glom.bw).*np.dii.glom.ui16;

    np.dii.microv.ui16 = uint16(vasc.ulex.microv.regofint).*np.dii.ui16;
    np.dii.microv.bw = vasc.ulex.microv.regofint.
    *imbinarize(np.dii.ui16,np.dii.thresh/2^16);
    np.dii.microv.ui16_thresh = uint16(np.dii.microv.bw).*np.dii.microv.ui16;

    np.dio.glom.ui16 = uint16(vasc.ulex.glom.regofint).*np.dio.ui16;
    np.dio.glom.bw = vasc.ulex.glom.regofint.
    *imbinarize(np.dio.ui16,np.dio.thresh/2^16);
    np.dio.glom.ui16_thresh = uint16(np.dio.glom.bw).*np.dio.glom.ui16;

    np.dio.microv.ui16 = uint16(vasc.ulex.microv.regofint).*np.dio.ui16;
    np.dio.microv.bw = vasc.ulex.microv.regofint.
    *imbinarize(np.dio.ui16,np.dio.thresh/2^16);
    np.dio.microv.ui16_thresh = uint16(np.dio.microv.bw).*np.dio.microv.ui16;

    np.np_overlay.glom.bw = uint16(cat
    (3,np.dii.glom.bw, np.dio.glom.bw, zeros(2200,2688)))*2^16;
    np.np_overlay.microv.bw = uint16(cat(
    3,np.dii.microv.bw, np.dio.microv.bw, zeros(2200,2688)))*2^16;

%Calculate background subtracted mean pixel intensity
    np.dii.glom.dist = np.dii.glom.ui16_thresh
    (np.dii.glom.ui16_thresh~=0)-np.dii.np_background;
    np.dii.microv.dist  = np.dii.microv.ui16_thresh
    (np.dii.microv.ui16_thresh~=0)-np.dii.np_background;
    np.dio.glom.dist = np.dio.glom.ui16_thresh
    (np.dio.glom.ui16_thresh~=0)-np.dio.np_background;
    np.dio.microv.dist  = np.dio.microv.ui16_thresh
    (np.dio.microv.ui16_thresh~=0)-np.dio.np_background;

    np.dii.glom.mean = mean(np.dii.glom.dist);
    np.dii.microv.mean = mean(np.dii.microv.dist);
```

```
np.dio.glom.mean = mean(np.dio.glom.dist);
np.dio.microv.mean = mean(np.dio.microv.dist);

np.dii.glom.area = numel(np.dii.glom.dist)*scale^2;
np.dii.microv.area = numel(np.dii.microv.dist)*scale^2;
np.dio.glom.area = numel(np.dio.glom.dist)*scale^2;
np.dio.microv.area = numel(np.dio.microv.dist)*scale^2;

np.dii.glom.total = np.dii.glom.mean*np.dii.glom.area;
np.dii.microv.total = np.dii.microv.mean*np.dii.microv.area;
np.dio.glom.total = np.dio.glom.mean*np.dio.glom.area;
np.dio.microv.total = np.dio.microv.mean*np.dio.microv.area;


save np.mat np;

data.glom(j-2,1) = j-2;
data.glom(j-2,2) = np.dii.glom.area;
data.glom(j-2,3) = np.dio.glom.area;
data.glom(j-2,4) = data.glom(j-2,2)/data.glom(j-2,3);
data.glom(j-2,5) = np.dii.glom.mean;
data.glom(j-2,6) = np.dio.glom.mean;
data.glom(j-2,7) = data.glom(j-2,5)/data.glom(j-2,6);
data.glom(j-2,8) = np.dii.glom.total;
data.glom(j-2,9) = np.dio.glom.total;
data.glom(j-2,10) = np.dii.glom.total/np.dio.glom.total;
data.glom(j-2,11) = nnz(vasc.ulex.glom.bw)*scale^2;
data.glom(j-2,12) = np.dii.glom.total/data.glom(j-2,11);
data.glom(j-2,13) = np.dio.glom.total/data.glom(j-2,11);

data.microv(j-2,1) = j-1;
data.microv(j-2,2) = np.dii.microv.area;
data.microv(j-2,3) = np.dio.microv.area;
data.microv(j-2,4) = data.microv(j-2,2)/data.microv(j-2,3);
data.microv(j-2,5) = np.dii.microv.mean;
data.microv(j-2,6) = np.dio.microv.mean;
```

```
    data.microv(j-2,7) = data.microv(j-2,5)/data.microv(j-2,6);
    data.microv(j-2,8) = np.dii.microv.total;
    data.microv(j-2,9) = np.dio.microv.total;
    data.microv(j-2,10) = np.dii.microv.total/np.dio.microv.total;
    data.microv(j-2,11) = nnz(vasc.ulex.microv.bw)*scale^2;
    data.microv(j-2,12) = np.dii.microv.total/data.microv(j-2,11);
    data.microv(j-2,13) = np.dio.microv.total/data.microv(j-2,11);

    cd ..

end

    save data.mat data;
    save np.mat np;

end
```

B.2 MATLAB code to 'create color map' on brightfield images

```
%load images and select pos/neg regions

close all
clear all

images = [dir('*02.tif'); dir('*03.tif')];
%loads images but does not read them yet

for ii = 1:length(images)
    img_name   = images(ii).name;
    info       = imfinfo(img_name);

    img.ui8   = imread(img_name);
    img.height = size(img.ui8,1);
    img.width  = size(img.ui8,2);
```

```
temp.ui8_r = uint8(img.ui8(:,:,1));
temp.ui8_g = uint8(img.ui8(:,:,2));
temp.ui8_b = uint8(img.ui8(:,:,3));

f1 = figure(1);
f1.Units = 'normalized';
f1.OuterPosition = [0 0.2 0.9 0.8];
imshow(img.ui8)

% select first positive region
h = msgbox('Select positive region 1');
uiwait(h);
findposreg1 = roipoly();
img.findposreg1 = findposreg1;

% select second positive region
h = msgbox('Select positive region 2');
uiwait(h);
%display('Select positive region 2')
findposreg2 = roipoly();
img.findposreg2 = findposreg2;

% make array where 1 is in selected positive regions and 0 is not
img.index_pos = img.findposreg1 + img.findposreg2;

% make index of the linear index of selected positive pixels
idx_pos = sort(unique(cat(1,find(img.findposreg1),find(img.findposreg2))));

% select first negative region
h = msgbox('Select negative region 1');
uiwait(h);
findnegreg1 = roipoly();
img.findnegreg1 = findnegreg1;

% select second negative region
```

```
h = msgbox('Select negative region 2');
uiwait(h);
findnegreg2 = roipoly();
img.findnegreg2 = findnegreg2;

% make array where 1 is in selected negative regions and 0 is not
img.index_neg = img.findnegreg1 + img.findnegreg2;

% make index of the linear index of selected negative pixels
idx_neg = sort(unique(cat(1,find(img.findnegreg1),find(img.findnegreg2))));

% convert to an indexed image with a colormap, display image

if ii == 1
    display('generating color map')
    [X,map] = rgb2ind(img.ui8,65536);
    %second input in this function is the number of colors
    %will run faster with fewer colors but you will get more false negative pix
else
    display('using previous color map')
    X = dither(img.ui8,map,8,7);
end

storeX = X;
% find all colors from colormap in both positive and negative selected
% regions
poscolors = sort(unique(X(idx_pos)));
negcolors = sort(unique(X(idx_neg)));

% make a list of all colors that
nooverlap = poscolors(find(-1*(ismember(poscolors,negcolors) - 1)));

for ll = 1:(size(X,1)*size(X,2))
    if ismember(X(ll),nooverlap) == 0
        X(ll) = 0;
    else
```

```
            continue
        end
    end

    storedPosColors(1:length(nooverlap),ii) = nooverlap;

end

PosColorList = unique(nonzeros(reshape(storedPosColors,[],1)));
save('PosColors.mat','PosColorList');
save('RefColorMap.mat','map');


f2 = figure(2);
f2.Units = 'normalized';
f2.OuterPosition = [0 0.2 0.9 0.8];
imagesc(X)
colormap(map)
axis image
colorbar
```

B.3 MATLAB code to quantify positive area in brightfield images

```
close all
clear all

images = dir('*.tif'); %loads images but does not read them yet

%select what you want to do, 1=true, 0=false
save_images = 0;

load('PosColors.mat');
load('RefColorMap.mat');
```

```
for ii = 1:length(images)
    imageNumber_outOf = [ii length(images)];
    imageNumber_outOf
    img_name = images(ii).name;
    info = imfinfo(img_name);

    img.ui8 = imread(img_name);
    img.height = size(img.ui8,1);
    img.width = size(img.ui8,2);
    img_area = img.height*img.width;

   indimage = dither(img.ui8,map,8,7);
    for ll = 1:(size(indimage,1)*size(indimage,2))
        if ismember(indimage(ll),PosColorList) == 0
            indimage(ll) = 0;
        else
            continue
        end
    end

    % convert indexed image to mask (zeros and ones)
    mask_idx = find(indimage);
    maskzeros = zeros(img.height,img.width);
    maskzeros(mask_idx) = 1;

    % dilate, erode ,fill holes in mask
    SE = strel('disk',5,4);
    dilated = imdilate(maskzeros,SE);
    eroded = imerode(dilated,SE);
    filledBWmask = imfill(eroded,'holes');

    conncomp = bwconncomp(filledBWmask);
    numPixels = cellfun(@numel,conncomp.PixelIdxList);
    img.stain = zeros(img.height, img.width);
      for kk = 1:conncomp.NumObjects
          if numPixels(kk) > 50
```

```
            img.stain(conncomp.PixelIdxList{kk}) = 1;
        end
    end

    % calculate the positive pixel number
    pos_area = nnz(img.stain);

    % make mask green
    filledgreenmask = uint8(cat(3,zeros
    (img.height,img.width),img.stain,zeros(img.height,img.width))*2^8);

    fig = figure(3);
    fig.Units = 'normalized';
    fig.OuterPosition = [0 0.2 0.8 0.8];

    subplot(4,2,[1,4]), imshow(filledgreenmask+img.ui8);
    subplot(4,2,[5,8]), imshowpair(filledgreenmask,img.ui8,'montage');

    % save images
    if save_images == 1
    picturename = sprintf([img_name(1:end-4) '_detected_stain']);
    saveas(gcf, picturename,'tif');
    end

    % store image name, positive pixels, total pixels in Results table
    Results(ii,1) = {img_name};
    Results(ii,2) = {pos_area};
    Results(ii,3) = {img_area};
    Results(ii,4) = {pos_area/img_area};

end

save('Results.mat','Results');
```

B.4 MATLAB code to quantify vascular area in a DICOM images

```
%clear all
close all

CT_images = dir('*.dcm');

info = dicominfo(CT_images(1).name);
pixelSize = info.PixelSpacing(1);
voxel_size = 0.625*pixelSize^2; % in mm

BG_img_file_name = CT_images(157).name; % change accordingly
BG_img           = dicomread(BG_img_file_name);

start_frame = 1;  % change accordingly
end_frame   = 157; % change accordingly
radius      = 100

plot_figures = 1;
find_center  = 1;
select_one_region = 0;
select_two_regions = 0;
cut_out_region     = 0;

%find organ center
if find_center == 1
    s = round((end_frame-start_frame+1)/2);
    img_name  = CT_images(s).name;
    img       = dicomread(img_name);
    figure(1), imshow(imadjust(img,[0.5 0.53],[]))

    h = msgbox('Select image region which should be cut out');
    display('Select image region which should be cut out')
    region = roipoly();
    neg_region = abs(1-region);
```

```
    img_BGsub = img-BG_img;
    img_BGsub(img_BGsub < 0) = 0;

    thresh_organ = graythresh(img_BGsub);
    img_BGsub_organ_bw = imbinarize(img_BGsub,thresh_organ);

    CC = bwconncomp(img_BGsub_organ_bw);
    numPixels = cellfun(@numel, CC.PixelIdxList);
    [biggest, idx] = max(numPixels);
    img_BGsub_organ_bw = zeros(512,512);
    img_BGsub_organ_bw(CC.PixelIdxList{idx}) = 1;

    img_BGsub_organ = img_BGsub_organ_bw.*double(img);
    img_BGsub_organ = img_BGsub_organ.*double(neg_region);

    figure(3), imshow(img_BGsub_organ_bw)
    img_BGsub_organ_cr = bwconncomp(img_BGsub_organ);
    c = regionprops(img_BGsub_organ_cr,'centroid');
    xCenter = c.Centroid(1);
    yCenter = c.Centroid(2);

    figure(2), imshow(img_BGsub_organ)
    hold on
    plot(xCenter,yCenter,'r+');
end

%real program starts

for i = start_frame:end_frame;%1:length(CT_images)

    img_name  = CT_images(i).name;
    img       = dicomread(img_name);

    if plot_figures == 1
    figure(1), imshow(imadjust(img,[0.5 0.53],[]))
```

```
 end

 img_BGsub = img-BG_img;
 img_BGsub(img_BGsub < 0) = 0;

 thresh_organ = graythresh(img_BGsub);
 img_BGsub_organ_bw = imbinarize(img_BGsub,thresh_organ);

 CC = bwconncomp(img_BGsub_organ_bw);
 numPixels = cellfun(@numel, CC.PixelIdxList);
 ecc = regionprops(CC, 'Eccentricity');
 ecc = struct2cell(ecc);
 [biggest, idx] = max(numPixels);
 if select_one_region == 0;
 for j = 1:length(CC.PixelIdxList)
     if numPixels(j) > 1000
        img_BGsub_organ_bw(CC.PixelIdxList{j}) = 1;
     else img_BGsub_organ_bw(CC.PixelIdxList{j}) = 0;
     end
 end
 end

if select_one_region == 1
   region = roipoly();
   img_BGsub_organ_bw = region.*img_BGsub_organ_bw;
end

if select_two_regions == 1
   region1 = roipoly();
   region2 = roipoly();
   region = region1+region2;
   img_BGsub_organ_bw = region.*img_BGsub_organ_bw;
end

if cut_out_region == 1
   region3 = roipoly();
```

```
   neg_region3 = abs(1-region3);
   img_BGsub_organ_bw = neg_region3.*img_BGsub_organ_bw;
end


img_BGsub_organ = img_BGsub_organ_bw.*double(img);
img_BGsub_organ = img_BGsub_organ.*double(neg_region);
organ_volume(i) = nnz(img_BGsub_organ)*voxel_size;

 if plot_figures == 1
 figure(2), imshow(img_BGsub_organ)
 end

 img_BGsub_vasc = img_BGsub_organ - 1100;
 img_BGsub_vasc(img_BGsub_vasc < 0) = 0;
 img_BGsub_vasc_bw = img_BGsub_vasc;
 img_BGsub_vasc_bw(img_BGsub_vasc_bw > 0) = 1;

 if plot_figures == 1
 figure(3), imshow(img_BGsub_vasc)
 end
 vasc_volume(i) = nnz(img_BGsub_vasc)*voxel_size;


 for k = 1:10;
     theta = (pi/5*(k-1)):0.1:(pi/5*k);
     x = radius*cos(theta)+xCenter;
     y = radius*sin(theta)+yCenter;
     x = [xCenter,x,xCenter];
     y = [yCenter, y, yCenter];
     mask = poly2mask(x,y,512,512);
     img_BGsub_vasc_segment  = img_BGsub_vasc.*double(mask);
     img_BGsub_organ_segment = img_BGsub_organ.*double(mask);
     if max(max(img_BGsub_organ_segment)) == 0;
        segment_present{i}(k) = 0;
        vasc_volume_segment{i}(k) = NaN;
```

```
        mean_intensity_segment{i}(k) = NaN;
    else segment_present{i}(k) = 1;
         vasc_volume_segment{i}(k) = nnz(img_BGsub_vasc_segment)*voxel_size;
        mean_intensity_segment{i}(k) =
        mean(mean(img_BGsub_vasc_segment(img_BGsub_vasc_segment~=0)));
        tf = isnan(mean_intensity_segment{i}(k));
        if tf == 1
           mean_intensity_segment{i}(k) = 0;
        end
    end
end

max_segment{i} = max(mean_intensity_segment{i});
min_segment{i} = min(mean_intensity_segment{i});


if min_segment{i} ~= 0
   overall_heterogeneity(i) = max_segment{i}/min_segment{i};
elseif max_segment{i} == 0;
    overall_heterogeneity(i) = 1;
else overall_heterogeneity(i) = max_segment{i};
end

    for l = 1:9
        if segment_present{i}(l) == 1 && segment_present{i}(l+1) == 1
            if mean_intensity_segment{i}(l)
            ~= 0 && mean_intensity_segment{i}(l+1) ~= 0
            f{i}(l) = mean_intensity_segment{i}
            (l)/mean_intensity_segment{i}(l+1);
            elseif mean_intensity_segment{i}(l)
            ~= 0 && mean_intensity_segment{i}(l+1) == 0
            f{i}(l) = mean_intensity_segment{i}(l);
            elseif mean_intensity_segment{i}(l)
            == 0 && mean_intensity_segment{i}(l+1) ~= 0
            f{i}(l) = mean_intensity_segment{i}(l+1);
            elseif mean_intensity_segment{i}(l)
```

```
            == 0 && mean_intensity_segment{i}(l+1) == 0
            f{i}(l) = 1;
            end

            if f{i}(l) < 1
               f{i}(l) = 1/f{i}(l);
            end
        else f{i}(l) = NaN;
        end
    end


    if segment_present{i}(10) == 1 && segment_present{i}(1) == 1
        if mean_intensity_segment{i}(10)
        ~=0 && mean_intensity_segment{i}(1) ~=0
            f{i}(10) = mean_intensity_segment{i}
            (10)/mean_intensity_segment{i}(1);
        elseif mean_intensity_segment{i}(10)
        ~=0 && mean_intensity_segment{i}(1) ==0
            f{i}(10) = mean_intensity_segment{i}(10);
        elseif mean_intensity_segment{i}(10)
        ==0 && mean_intensity_segment{i}(1) ~=0
            f{i}(10) = mean_intensity_segment{i}(1);
        elseif mean_intensity_segment{i}(10)
        ==0 && mean_intensity_segment{i}(1) ==0
            f{i}(10) = 1;
        end
        if f{i}(10) < 1
            f{i}(10) = 1/f{i}(10);
        end
    else f{i}(10) = NaN;
    end
    segment_heterogeneity(i) = nansum(f{i})/sum(~isnan(f{i}));

end
```

```
total_organ_volume = sum(organ_volume(start_frame:end_frame));
total_vasc_volume  = sum(vasc_volume(start_frame:end_frame));

total_mean_segment_heterogeneity
= nanmean(segment_heterogeneity(start_frame:end_frame));

total_overall_heterogeneity_mean
= nanmean(overall_heterogeneity(start_frame:end_frame));


for o = 1:10
    count(o) = 0;
    f2_sum(o) = 0;
    for n = start_frame:end_frame-1
        if segment_present{n}(o) == 1 && segment_present{n+1}(o) == 1
            if mean_intensity_segment{n}(o)
            ~= 0 && mean_intensity_segment{n+1}(o) ~= 0;
               f2{n}(o) = mean_intensity_segment{n}(o)/
               mean_intensity_segment{n+1}(o);
            elseif mean_intensity_segment{n}(o)
            ~= 0 && mean_intensity_segment{n+1}(o) == 0;
                f2{n}(o) = mean_intensity_segment{n}(o);
            elseif mean_intensity_segment{n}(o)
            == 0 && mean_intensity_segment{n+1}(o) ~= 0;
                f2{n}(o) = mean_intensity_segment{n+1}(o);
            elseif mean_intensity_segment{n}(o)
            == 0 && mean_intensity_segment{n+1}(o) == 0;
                f2{n}(o) = 1;
            end
            if f2{n}(o) < 1
               f2{n}(o) = 1/f2{n}(o);
            end
            count(o) = count(o) + 1;
            f2_sum(o) = f2_sum(o) + f2{n}(o);
        else f2{n}(o) = NaN;
```

```
        end
    end
    longitudinal_segment_heterogeneity(o) = f2_sum(o)/count(o);
end


total_longitudinal_heterogeneity
= sum(longitudinal_segment_heterogeneity)/10;

segment_heterogeneity = segment_heterogeneity';
overall_heterogeneity = overall_heterogeneity';
longitudinal_segment_heterogeneity = longitudinal_segment_heterogeneity';


Results_all_frames(1) = total_organ_volume;
Results_all_frames(2) = total_vasc_volume;
Results_all_frames(3) = total_vasc_volume/total_organ_volume;
Results_all_frames(4) = total_mean_segment_heterogeneity;
Results_all_frames(5) = total_overall_heterogeneity_mean;
Results_all_frames(6) = total_longitudinal_heterogeneity;

save(['Results.mat'], 'segment_heterogeneity', 'overall_heterogeneity',
'longitudinal_segment_heterogeneity','Results_all_frames');
```

B.5 MATLAB code to quantify vascular heterogeneity in DICOM images

B.5.1 Build output file

Contents

- Load files
- find the 99.5th percentile
- Load Large vasculature con dicom stack
- Load microvasculature con dicom stack
- Load delayed perfusion con dicom stack

- calculate normalized areas
- save results

Load files

```
thresh1 = 800; %emperically determinde threshold for subtracting background

user_path_noncon = uigetdir(...
    '/Users'...
    , 'Select DICOM Directory for Non-contrast images');

user_path_large = uigetdir(...
    '/Users/'...
    , 'Select Large Vasc DICOM directory');

user_path_micro = uigetdir(...
    '/Users/'...
    , 'Select Micro Vasc DICOM directory');

user_path_delayed = uigetdir(...
    '/Users/'...
    , 'Select delayed perfusion DICOM directory');
```

find the 99.5th percentile

```
statBar = waitbar(0,'Processing non-contrast images'); %initialize progress bar

cd(user_path_noncon)

ctNC = load('ct.mat');
ctNC = ctNC.ct;

%Create bw image
ctNC.im = uint16(ctNC.im);
%Convert to 16bit integer format - should be fixed in dicom_load.m
ctNC.bw = imbinarize(ctNC.im,thresh1/(2^16));
%Value previously determined empirically
```

```
for ii = 1:size(ctNC.bw,3)
    ctNC.bw_filt(:,:,ii) = bwareafilt(ctNC.bw(:,:,ii),1);
    %Select largest feature in each frame
    %note this breaks down at the Z dimension edges if there is free contrast
    ctNC.bw_filt(:,:,ii) = imfill(ctNC.bw_filt(:,:,ii),'holes');
end

x = ctNC.im;
z = reshape(x, 1,[]);
z(z < thresh1) = [];
figure;histogram(z)
upperThresh = double(prctile(z,99.5));
```

Load Large vasculature con dicom stack

```
waitbar(0.33, statBar ,'Processing Large Vasculature images');

cd(user_path_large)

ctL = load('ct.mat');
ctL = ctL.ct;

%Create bw image
ctL.im = uint16(ctL.im);
%Convert to 16bit integer format - should be fixed in dicom_load.m
ctL.bw = imbinarize(ctL.im,800/(2^16));
%Value previously determined empirically
ctL.bw_con = imbinarize(ctL.im,upperThresh/(2^16));

totalArea = 0;
totalAreaConLarge = 0;

for ii = 1:size(ctL.bw,3)
    ctL.bw_filt(:,:,ii) = bwareafilt(ctL.bw(:,:,ii),1);
    %Select largest feature in each frame
    %note this breaks down at the Z dimension edges if there is free contrast
```

```
    ctL.bw_filt(:,:,ii) = imfill(ctL.bw_filt(:,:,ii),'holes');

    totalArea = totalArea + sum(sum(ctL.bw_filt(:,:,ii)));
    totalAreaConLarge = totalAreaConLarge + sum(sum(ctL.bw_con(:,:,ii)));
end
```

Load microvasculature con dicom stack

```
waitbar(0.66, statBar ,'Processing micro-vasculature images');

cd(user_path_micro)

ctM = load('ct.mat');
ctM = ctM.ct;

%Create bw image
ctM.im = uint16(ctM.im);
%Convert to 16bit integer format - should be fixed in dicom_load.m
ctM.bw = imbinarize(ctM.im,800/(2^16));
%Value previously determined empirically
ctM.bw_con = imbinarize(ctM.im,upperThresh/(2^16));

totalArea2 = 0;
totalAreaConMicro = 0;

for ii = 1:size(ctM.bw,3)
    ctM.bw_filt(:,:,ii) = bwareafilt(ctM.bw(:,:,ii),1);
    %Select largest feature in each frame
    %note this breaks down at the Z dimension edges if there is free contrast
    ctM.bw_filt(:,:,ii) = imfill(ctM.bw_filt(:,:,ii),'holes');

    totalArea2 = totalArea2 + sum(sum(ctM.bw_filt(:,:,ii)));
    totalAreaConMicro = totalAreaConMicro + sum(sum(ctM.bw_con(:,:,ii)));
end
```

Load delayed perfusion con dicom stack

```
waitbar(0.85, statBar ,'Processing delayed perfusion images');

cd(user_path_delayed)

load('ct.mat')
ctD = load('ct.mat');
ctD = ctD.ct;

%Create bw image
ctD.im = uint16(ctD.im);
%Convert to 16bit integer format - should be fixed in dicom_load.m
ctD.bw = imbinarize(ctD.im,800/(2^16));
%Value previously determined empirically
ctD.bw_con = imbinarize(ctD.im,upperThresh/(2^16));

totalArea3 = 0;
totalAreaConDelayedPerfusion = 0;

for ii = 1:size(ctD.bw,3)
    ctD.bw_filt(:,:,ii) = bwareafilt(ctD.bw(:,:,ii),1);
    %Select largest feature in each frame
    %note this breaks down at the Z dimension edges if there is free contrast
    ctD.bw_filt(:,:,ii) = imfill(ctD.bw_filt(:,:,ii),'holes');

    totalArea3 = totalArea3 + sum(sum(ctD.bw_filt(:,:,ii)));
    totalAreaConDelayedPerfusion
    = totalAreaConDelayedPerfusion + sum(sum(ctD.bw_con(:,:,ii)));
end
```

calculate normalized areas

```
waitbar(1, statBar ,'Calculating normalized areas');

vol_kidney = (totalArea + totalArea2)/2;
vol_vasc = totalAreaConMicro;
```

```
vol_largeVasc = totalAreaConLarge;
vol_microVasc = totalAreaConMicro - totalAreaConLarge;
vol_delayedPerfusion = totalAreaConDelayedPerfusion - totalAreaConLarge;

vol_normalized_vasc = vol_vasc / vol_kidney;
vol_normalized_largeVasc = vol_largeVasc / vol_kidney;
vol_normalized_microVasc = vol_microVasc / vol_kidney;
vol_normalized_delayedPerfusion = vol_delayedPerfusion / vol_kidney;
```

save results

```
waitbar(1, statBar ,'saving results');

output(1).im_noncon = ctNC(1).im;
output(1).im_largeVasculature = ctL(1).im;
output(1).im_microVasculature = ctM(1).im;
output(1).im_delayedPerfusion = ctD(1).im;

output(1).bw_totalArea = ctM(1).bw_filt;
output(1).bw_largeVasculature = ctL(1).bw_con;
output(1).bw_microVasculature = ctM(1).bw_con;
output(1).bw_delayedPerfusion = ctD(1).bw_con;

output(1).thresh1 = thresh1;
output(1).thresh2 = upperThresh;

output(1).user_path_large = user_path_large;
output(1).user_path_micro = user_path_micro;
output(1).user_path_noncon = user_path_noncon;
output(1).user_path_delayed = user_path_delayed;

output(1).vol_normalized_vasc = vol_normalized_vasc;

waitbar(1, statBar ,'done');
pause(0.1); close(statBar);
```

B.5.2 Analyze cortex heterogeneity

Contents

- Create binary images
- Generate histograms

```
[file, user_path_output] = uigetfile
('*.mat', 'Please Select the output.mat file');
load(fullfile(user_path_output,file)); img = output(1).im_largeVasculature;

% inputs

start_frame = 1;
end_frame   = 160;
single_frame = idivide( (end_frame+start_frame) , int16(2));
%currently choosing the midpoint between start and end frames
distance      = 8;
thickness = 8;
show_fig = 1;

% outputs: whole_kidney_cortex_pixels, single_frame_kidney_cortex_pixels
```

Create binary images

```
BG_thresh = 800;
img_bw = imbinarize(img, BG_thresh/(2^16));
%Value previously determined empirically
img_bw_filt = false(size(img_bw));
img_bw_cortex = false(size(img_bw));

for ii = start_frame:end_frame %1:size(img_bw, 3)
    img_bw_filt(:,:,ii) = bwareafilt(img_bw(:,:,ii),1);
    %Select largest feature in each frame
    %note this breaks down at the Z dimension edges if there is free contrast
    img_bw_filt(:,:,ii) = imfill(img_bw_filt(:,:,ii),'holes');

    %figure; imshow(img_bw_filt(:,:,ii));
```

```
    se = strel('disk', distance, 4);
    img_bw_cortex_outer = imerode(img_bw_filt(:,:,ii), se);

    se = strel('disk', thickness, 4);
    img_bw_cortex_inner = imerode(img_bw_cortex_outer, se);


    if(show_fig)

        [B,~] = bwboundaries(img_bw_cortex_outer);
        [B2,~] = bwboundaries(img_bw_cortex_inner);
        figure(1), imshow(img(:,:,ii), []); title(strcat('slice #', num2str(ii)));
        hold on

        for k = 1:length(B)
           boundary = B{k};
           plot(boundary(:,2), boundary(:,1), 'r', 'LineWidth', 1)
        end

        for k = 1:length(B2)
           boundary = B2{k};
           plot(boundary(:,2), boundary(:,1), 'r', 'LineWidth', 1)
        end

        hold off
    end

    bw_cortex = img_bw_cortex_outer;
    bw_cortex(img_bw_cortex_inner) = false;
    img_bw_cortex(:,:,ii) = bw_cortex;
    %figure; imshow(img_bw_cortex);
end
```

Generate histograms

```
whole_kidney_cortex_pixels = img(img_bw_cortex);
```

```
figure; histogram(whole_kidney_cortex_pixels);
title('Cortex histogram')
grid on;


x = img(:,:,single_frame);
single_frame_kidney_cortex_pixels = x(img_bw_cortex(:,:,single_frame));
figure; histogram(single_frame_kidney_cortex_pixels);
title(strcat('Cortex histogram for slice #', num2str(single_frame)))
grid on;
```